Department of Physics and Astronomy
University of Heidelberg

MASTER-THESIS

in Physics

submitted by

Paul Faßl

born in Gießen (Germany)

2013

Identification and optimization of mixed light emitting layers in phosphorescent multilayer OLEDs

This Master thesis has been carried out by Paul Faßl

at the InnovationLab in Heidelberg

under the supervision of

Prof. Dr.-Ing. habil. Wolfgang Kowalsky

and Dr. Norman Mechau

Erkennung und Optimierung von gemischten Emitterschichten in phosphoreszierenden Multischicht-OLEDs

Phosphoreszierende OLEDs (PHOLEDs) sind aus kleinen Molekülen aufgebaut und bergen großes Potenzial für eine Vielzahl zukünftiger Anwendungen. Die Effizienz von PHOLEDs kann mit der von konventionellen Leuchtmitteln schon konkurrieren. Allerdings zeigen PHOLEDs typischerweise einen stetigen Abfall ihrer Effizienz bei hohen Stromdichten, ein Effekt der als Effizienz-RollOff bekannt ist. Einer der Gründe dafür ist die hohe Wahrscheinlichkeit für Triplet-Triplet-Annihilationsprozesse. Diese Prozesse sind einerseits der langen Lebensdauer der phosphoreszierenden Farbstoffe und andererseits einer sehr hohen Triplet-Dichte in der meist sehr engen Rekombinationszone in typischen OLED Heterostrukturen geschuldet. Ein Ansatz um diesen Roll-Off zu minimieren ist die Einführung einer gemischten Emitterschicht. Hierbei werden zwei Materialen gemischt, in denen eines bevorzugt Löcher und das andere bevorzugt Elektronen transportiert.

Im ersten Teil dieser Arbeit werden die Eigenschaften von PHOLEDs mit einer konventionellen Heterostruktur, einer einheitlich durchmischten Struktur und einer Struktur mit einem graduellen Übergang detailliert analysiert. PHOLEDs mit einer graduellen Struktur zeigten dabei im Vergleich zu denen mit einer konventienellen Heterostruktur eine erhöhte Quanteneffizienz, einen reduzierten Effizienz-RollOff und eine längere Lebensdauer. Diese Effekte werden einer verbreiterten Rekombinationszone und einem besseren Ladungsgleichgewicht in der Emitterschicht zugeschrieben.

Techniken um eine Durchmischung zweier Schichten zu detektieren sind sehr teuer und zeitaufwändig. Im zweiten Teil dieser Arbeit wurde geprüft, ob Impedanzspektroskopie sich als geeignetes und kostensparendes Verfahren zur Erkennung des Durschmischungsgrades zweier Schichten eignet. Es wurden Messungen einschichtiger Proben durchgeführt um die charakteristischen Parameter der Materialen zu bestimmen. Darauf aufbauend wurden zwei Fit-Funktionen formuliert und auf Messungen von Proben mit unterschiedlichem Durchmischungsgrad angewandt. Eine der Fit-Funktionen war in der Lage den Grad der Vermischung für alle untersuchten Strukturen sehr gut zu bestimmen.

Identification and optimization of mixed light emitting layers in phosphorescent multilayer OLEDs

Phosphorescent OLEDs (PHOLEDs) based on organic small molecules offer a great potential for a variety of future applications. In terms of efficiency PHOLEDs can already compete with conventional light sources. However, PHOLEDs typically suffer from a steady decrease in efficiency at high current densities, known as efficiency roll-off. One of the reasons for this is the high probability for triplet-triplet quenching processes. On the one hand these processes happen due to the long lifetime of the triplet phosphors and on the other hand due to the high triplet density in the rather narrow recombination zone in common OLED heterostructures. One approach to minimize this roll-off is to introduce a mixed host structure in the light emitting layer. This is done by mixing one mostly hole-transporting material and one mostly electron-transporting material with each other.

In the first part of this thesis, the characteristics of PHOLEDs with a conventional heterostructure, a uniformly mixed host structure and a graded mixed host structure were studied in detail. PHOLEDs with a graded mixed structure showed an increased quantum efficiency, a reduced efficiency roll-off and a longer lifetime compared to them with conventional heterostructure. These effects are attributed to the broadening of the recombination zone and a better charge balance inside the light emitting layer.

Existing techniques for the detection of intermixing are very expensive and time consuming. In the second part of this thesis, it was tested whether impedance spectroscopy can be used as a suitable and cheap tool to measure the degree of intermixing between two layers. Measurements of the single materials were made to extract their characteristic parameters. Two fit functions were formulated and applied to measurements of devices with different degrees of intermixing. One of the fit functions was able to identify intermixing for all tested devices very well.

Contents

1. Introduction

Due to their potential applications in electronic displays and solid state lighting, organic light emitting diodes (OLEDs) have received much attention from researchers as well as industry since the pioneering work of Tang and VanSlyke, who were the first introducing a double-layer structure for organic semiconductors in 1987 [1]. OLEDs feature efficient light generation with a wide viewing angle and the ability to be fabricated cost efficiently on large area devices and flexible substrates. OLED displays are presently used in many portable electronic devices and the first OLED flat-panel displays offering brilliant color rendering and low energy consumption have just entered the market. Other future application possibilites involve the use of OLEDs for the next generation of solid-state light sources, as sensors in biomedical applications and in organic laser diodes.

In 1998, Baldo et al. showed that the doping of organic small molecules with a phosphorescent heavy metal complex allows for the radiative emission of both, singlet and triplet excitons. This leads to a theoretical internal quantum efficiency of 100% [2]. Thus, in terms of efficiency OLEDs can compete with conventional light sources. However, they typically suffer from a steady decrease of efficiency at high current densities, known as efficiency roll-off. It is mainly ascribed to the long lifetime of the triplet phosphors, resulting in enhanced triplet quenching effects, but the underyling physics is not fully understood [3]. Future large area illumination will require OLED luminance levels of about $5000\frac{\mathrm{cd}}{\mathrm{m}^2}$ corresponding to current densities of $>100\frac{\mathrm{mA}}{\mathrm{cm}^2}$ [4], while for organic lasers peak current densities of even $>1\mathrm{kA}\frac{\mathrm{mA}}{\mathrm{cm}^2}$ are needed [5]. Providing a sufficient enough lifetime for OLEDs driven at such high current densities is another challenge [6].

Different methods have been proposed in the last decade to reduce the efficiency roll-off and increase the lifetime of OLEDs, including the broadening of the rather narrow recombination zone inside the light emitting layer. One approach to do that is by mixing one mostly electron-tranporting and one mostly hole-transporting material with each other. The resulting bipolar current shifts the recombination zone away from the interfaces and thereby leads to a lower roll-off and improved lifetime [7,8].

A further advantage of the OLED technology is its applicability in solution processing, which comes with a strong potential to decrease production costs [9, 10]. Although the resolution of today's printing techniques cannot compete with that of

inorganic semiconductors, it is sufficient enough for lighting applications and pho-
tovoltaics. However, with solution processing new difficulties arise: When printing
multiple layers of different materials on each other, the solvent of a freshly applied
layer may dissolve the underlying layer. One way to avoid such an intermixing be-
tween two layers is to use solvents which do not dissolve the neighbouring layer
(orthogonal solvents) [11,12]. Presently, especially for small molecules it can be dif-
ficult to find truly orthogonal solvents. The solubility in general can be changed by
adding or changing side chains of the molecules which however may lead to changes
in the characteristics of the small molecules. If the solvents are not truly orthogonal,
the solvent of one freshly applied layer may partially dissolve the underlying layer.
This leads to intermixing of the layers, which can alter the device's characteristics.

The most precise methods to identify the degree of intermixing between two
layers is energy resolved electron tomography. This is realized by cutting out a slice
of a sample and analyze it with an energy resolved transmission electron microscope
(TEM) under different tilting angles and varying electron energies so that a 3D
image of the samples material composition can be calculated. Another method is
X-ray photoelectron spetroscopy (XPS) in combination with sputtering. X-rays with
a well known energy are used to extract electrons from the surface of a sample in
order to measure the energy spectrum of the electrons. At the same time ions with
a high kinetic energy erode the surface (sputtering) so that layer by layer can be
measured and a depth profile of the sample can be calculated. However, both of
these methods are very expensive, time consuming and destructive so that finding a
viable alternative would be advantegous [13,14].

Recently, impedance spectroscopy was introduced as an alternative to detect
intermixing in evaporated double layers of Alq3 and NPD [15]. The basic idea of
impedance spectroscopy is that any thin, conductive layer can be described by an
equivalent circuit of a resistor and a capacitor in parallel. The parameters of these
circuit elements are thickness dependent and can be determined by measuring the
impedance spectrum of a device. Afterwards they can be correlated to the intrin-
sic parameters of the material, the conductivity and the permittivity. For the case
that intermixing occurs between two of such layers, it can be expected that the
impedance spectrum differs from that of an ideal double layer without intermixing.
If these changes can readily be identified, in general the detection of intermixing of
two layers should be possible.

In the first part of this thesis, the characteristics of OLEDs with different mixed

host structures are compared: A highly simplified OLED composed of two organic layers was used as a test device [16]. This OLED structure exhibits a conventional heterostructure, where the phoshphorescent dye $Ir(ppy)_3$ is doped into the electron transporting layer at the vicinity of the hole transporting layer. The hole- and electron transporting materials are TCTA and TPBI respectively. For efficient hole-injection from the ITO anode, MoO_3 is used and the cathode consists of Calcium and silver. The emitting layer was modified by in two different ways: One uniformly mixed host with a mixing ratio of 63:30:7 $TPBI:TCTA:Ir(ppy)_3$ and three graded mixed host structures with varying thicknesses between 30 nm and 70 nm were produced. All devices were fabricated by thermal vacuum evaporation. The different OLED-stacks are characterized and compared to each other in detail. The differences in their LIV-characteristics, efficiency roll-off, emission spectra and lifetime are discussed and conclusions are drawn.

In the second part of this thesis, devices with a graded mixed structure were analyzed with impedance spectroscopy in order to identify the intermixed region. Before this was done, each of the materials - TCTA, TPBI and MoO_3 - had been characterized using impedance spectroscopy and suitable equivalent circuits to extract their material parameters were introduced. Furthermore, external influences arising from the contacting layers as well as from space charges at the interfaces of the organic materials and the electrodes are analyzed in detail. Finally, two fit functions for the detection of intermixing in organic layers are introduced and their applicability is tested for devices with a graded mixed host structure.

This thesis is structured in the following way: In chapter 2 the theoretical principles are introduced. Firstly, the basic physics of organic semiconductors are described. Secondly, fundamental aspects concerning organic light emitting diodes are presented with special emphasis on factors determining their efficiency. Thirdly, the basic principles of impedance spectroscopy are explained and it is introduced as a tool for the identification of intermixed organic layers. Chapter 3 deals with the experimental setup of the evaporation system and the impedance measurement devices. In chapter 4 the materials and the device fabrication are presented and the structures of the OLED-stacks are introduced. In chapter 5 the OLED stacks are characterized and compared to each other in detail. Finally, in chapter 6 the results of the impedance measurements are summarized and relevant conclusions are drawn.

2. Theoretical principles

In this chapter, the theoretical principles of this thesis will be introduced. In section 2.1 the general characteristics of organic semiconductors will be illustrated. Subsequently, in section 2.2 important features concerning organic light emitting diodes (OLEDs) are presented, where special focus is given to factors determining the efficiency of phosphorescent OLEDs and to mixed host strucutres. Fundamental aspects of impedance spectroscopy needed for the understanding of the measurements performed in this thesis are explained in section 2.3.

2.1 Organic semiconductors

Anorganic semiconducting materials are in most cases of crystalline nature. Because of the existence of a long range order, the electrons experience a periodic lattice potential resulting in the formation of a band structure. In the ground state, the highest occupied energy level is called valence band and the lowest unoccupied energy level forms the conduction band. Free charge carriers inside these bands are strongly delocalized yielding a high conductivity of these materials.

In contrast, organic semiconducting materials mostly exhibit an amorphous or polycrystalline structure. The conductivity arises from the formation of π-orbitals, which allow for the delocalization of electrons within single molecules. However, the large distance between adjacent molecules states an energy barrier for charge carriers, strongly limiting the conductivity of these materials. Organic materials are divided into two subgroups, namely small molecules and polymers. This thesis deals with small molecules, but most of the concepts presented in this section are also applicable to polymers. The sources used for the roundup of the fundamental principles were: [17, 18]. Additonal sources are denoted in the text.

2.1.1 Hybridisation

The definition of materials as 'organic' arises from the fact that they mainly consist of carbon atoms. Their six electrons have the electronic configuration $1s^2 2s^2 2p_x^1 2p_y^1$. When a carbon atom is forming a chemical bond, it is energetically most favourable that the orbitals undergo a so called hybridisation. Here, one of the 2s-electrons is first excited into the remaining free 2p-orbital, yielding the electronic configuration
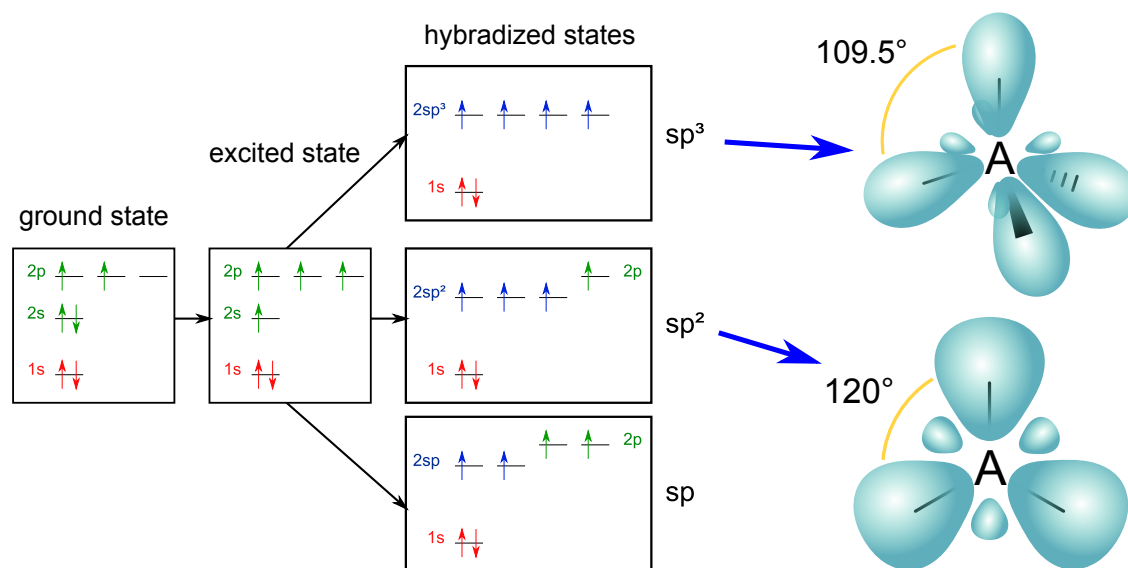
Figure 2.1: **Left**: Reprensation of the processes resulting in an hybridised state. The core electrons are shown in red, valence electrons in green and the hybrid orbitals in blue [19]. **Right**: Illustration of the sp3- and sp2-orbitals. Taken from [20, 21].

$1s^1 2s^2 2p_x^1 2p_y^1 2p_z^1$. Subsequently, the three p_z orbitals and the remaining 1s orbital can hybridise in three different ways, called sp3-, sp2- and sp-hybridisation. These processes are illustrated on the left side in figure 2.1.

For the sp3-hybridisation, four new hybrid orbitals are generated with their wavefunctions being a linear combination of the primary orbitals and orthogonal to each other. The orbitals are arranged in an angle of 109.5° to each other (right side of figure 2.1). One example for sp3-hybridisation is diamond, where the sp3-orbitals of neighbouring atom strongly overlap yielding a minimized energy and an energetically very strong bond.

The electronic properties of organic materials are mainly definied by sp2-hybridisation, which is exemplified in more detail in the next section. Here, 2 of the p-orbitals mix with the 1s-orbital into three hybrid orbitals which are lying on the molecular xy-plane and are arranged in an angle of 120° to each other (see also right side of figure 2.1). The remaining $2p_z$-orbital is arranged perpendicular to them.

The sp-hybridisation can explain the linear structure in molecules. It yields 2 hybrid oribtals with an angle of 180° to each other and the two remaining p-orbitals are arranged perpendicular to them. Examples for this hybridisation are ethyne and magnesium hydride.
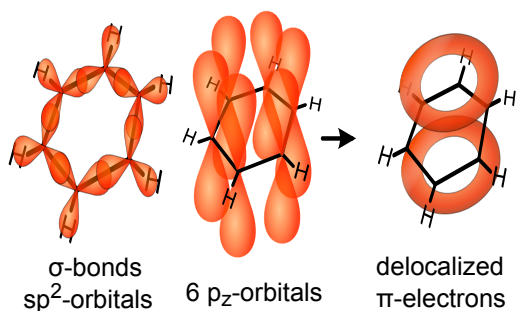
Figure 2.2: Electronic configuration of benzol. The σ-electrons are strongly localized between the carbon atoms. The p_z-orbitals of the atoms undergo weak π-bonds. These π-electrons are delocalized throughout the whole benzol ring. Taken from [22].
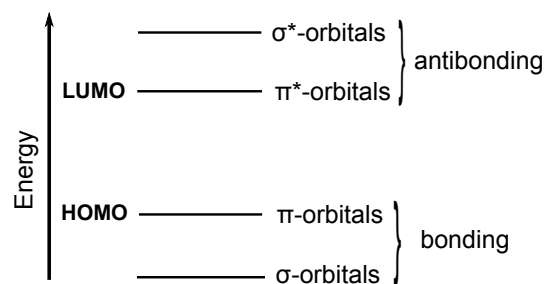
Figure 2.3: Illustration of the energy levels in an organic semicondctor. The HOMO defines the highest occupied and the LUMO the lowest unoccupied molecular orbitals. Adapted from [23].

HOMO-LUMO level

As already mentioned, the sp2-hybridisation is the basis for the electronic properties of organic small molecules and polymers. When carbon atoms form bonds, an overlap of the sp^2-orbitals results in the formation of strong σ-bonds, which split into two energy levels, one bonding σ-orbital and one antibonding σ*-orbital. They are the main contributors to the molecular bond and strongly localized between the carbon atoms. Additionally, the remaining p$_z$-orbitals yield weaker π-bonds, which are also divided into bonding π- and antibonding π*-bonds. These orbitals only weakly contribute to the molecular bond and their electrons are delocalized over all involved atoms, resulting in a so called π-electron system. This is exemplary depicted for benzol in figure 2.2, where the π-electrons are delocalzed over the whole benzol-ring. The smallest energetic excitaion inside such systems arises from the bonding π- into the antibonding π*-orbitals, which are defined as HOMO (Highest Ocuppied Molecular Orbital)- respectively LUMO (Lowest Unoccupied Molecular Orbital) levels and can be correlated to the valence- and conduction band of anorganic semicondcutors. Their energy levels are schematically depicted in figure 2.3.

The lack of a long range order in many organic materials and the according variation of the intermolecular distances and orientations result in a statistical distribution of the different molecular energy levels. Therefore, the HOMO- and LUMO level exhibit a gaussian like energetic distribution. Additionally, because of the limited overlap of the molecular orbitals, molecules only interact via weak Van-der-Waal
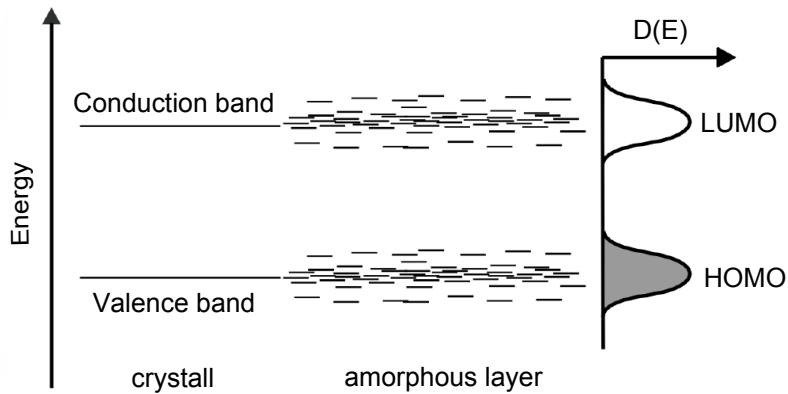
Figure 2.4: Schematic of the position of the energy levels of a crystalline and an amorphous semiconductor.

forces, which strongly localizes the electronic states on single molecules. A schematic diagram of the energetic levels of crystalline and amorphous structures is shown in figure 2.4. Typical values for the HOMO-LUMO-gap are in the range of 1,5-3,5 eV..

2.1.2   Charge transport

The charge transport in disordered organic solds is well described within the Bässler model for hopping transport [25]. The localization of the electrons and the gaussian distribution of the transport levels result in the presence of a distribution of different energetic barriers for electrons, strongly limiting the charge transport in organic semiconductors. These barriers can be overcome by a thermally activated process. The possibility for an electron to "hop" across the potential barrier (hopping rate) is proportional to the boltzmann factor $e^{-\frac{E_a}{k_B T}}$, where $k_B T$ is the thermal energy and E_a defines the energetic barrier. When no external field is applied, the averaged hopping rate is zero. An applied external electrical field reduces the energetic barriers in a preferred direction, which is illustrated in figure 2.5. The charge carriers are thus able to overcome the barriers in this direction, yielding a directed current. In general, the mobility of organic semiconductors is dependant on the temperature T and applied electric field E. Where A common empiric form, able to describe many experimental observations, is the so-called Poole-Frenkel form of the mobility:

$$\mu(T,E) = \mu_0 \cdot \exp^{-\frac{(\Delta_0 - \beta\sqrt{E})}{k_B T}} . \qquad (2.1)$$

Here, μ_0 is the zero-field mobility and Δ_0 and β are empiric constants. Many other models exist, taking into account a dependence of the mobility on charge carrier
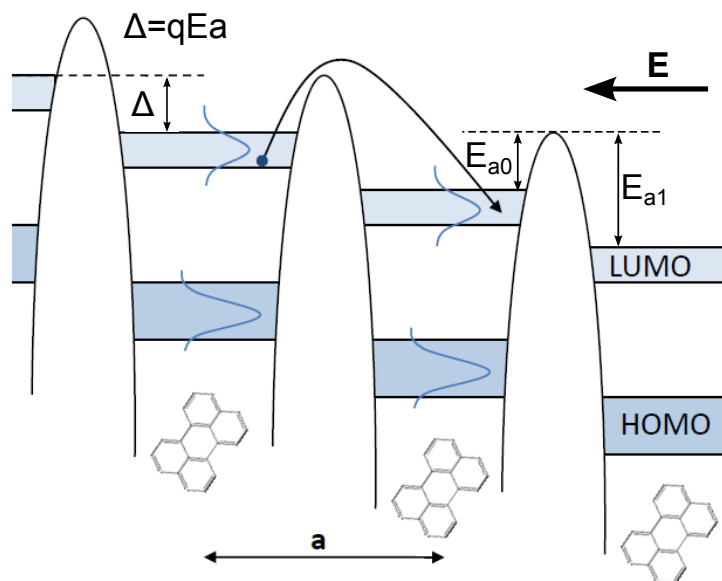
Figure 2.5: Illustration of the electron transport mechanism described by the hopping model. An external field reduces the energy barrier between two molecular transport states from E_{a1} to E_{a0} so that an electron can hop over the barrier. Adapted from [24].

density and holding an improved temperature dependence [26–30].

Charge carrier injection

The considerations in this section describe the case for idealized electrodes and assume the HOMO- and LUMO levels to be fixed. However, the principles can be used for the understanding of the main processes concerning charge injection in organic semiconductors [31]. Organic semiconductors are normally sandwiched between two types of electrodes. At the interface between the electrodes and the organic layer the electrons have to overcome an injection barrier, which is determined by the difference between the work function of the cathode (Φ_C) respectively anode (Φ_A) and the LUMO respectively HOMO level of the organic layer:

$$\Phi_e = \Phi_C - W_{\mathrm{LUMO}} \ \ \text{respectively} \ \ \Phi_h = W_{\mathrm{HOMO}} - \Phi_A \qquad (2.2)$$

In most cases, the two electrodes have different work functions ($\Phi_C \neq \Phi_A$). Before charges can be injected into the organic layer, an external field has to overcome this work function difference, which is defined as the built-in potential V_{bi} of an device:

$$V_{\mathrm{bi}} = \frac{\Phi_C - \Phi_A}{e} \qquad (2.3)$$

Applying a voltage V, the internal field in the organic layer (assuming it to be constant throughout the layer) will be:

$$E = \frac{V - V_{bi}}{d} \qquad (2.4)$$

For $E > 0$, charges can be either injected by a thermally activated process or by tunneling. The first case can be approximated by the Richardson equation (introduced for the thermal emission of electrons from a glow cathode in vacuum valves). Additionally, one must take into account that image charges (Schottky effect) lead to a reduction of the effective barrier height. In that case, the current density can be described by the Richardson-Schottky-equation [32]:

$$j_{RS} = A^* T^2 \exp\left(-\frac{\Phi_e - \beta\sqrt{E}}{k_B T}\right) \qquad (2.5)$$

Here, A^* is a constant proportional to the effective mass m^* of the charge carriers. The tunneling injection process is approximated for a triangular barrier Φ_B and was calculated by Fowler and Nordheim [33] to be

$$j_{FN} = \frac{A^*}{\Phi_B}\left(\frac{eE}{\alpha k_B}\right)^2 \exp\left(-\frac{2\alpha\Phi_B^{1.5}}{3eE}\right), \qquad (2.6)$$

where α is a constant. The two described injection processes are limiting cases and were first introduced for anorganic semiconductors. For organic semiconductors one has to take into account additional effects for a complete description of the charge carrier injection process, but this is beyond the scope of this thesis [31].

IV-characteristics

It is interesting to look at the IV-characteristics of organic semiconductors, as they also determine the general charge transport characteristics of organic light emitting diodes. The definitions described here only apply to single-carrier-devices (electrons or holes), but can be used as a starting point to model the bipolar current behaviour in OLEDs. Before charges are injected into an organic semiconductor, i.e. for a voltages below the built-in voltage, only intrinsic charge carriers can contribute to the current. Owing to the large band gap, the thermally activated intrinsic charge carrier density in organic semiconductors is much smaller than in their anorganic
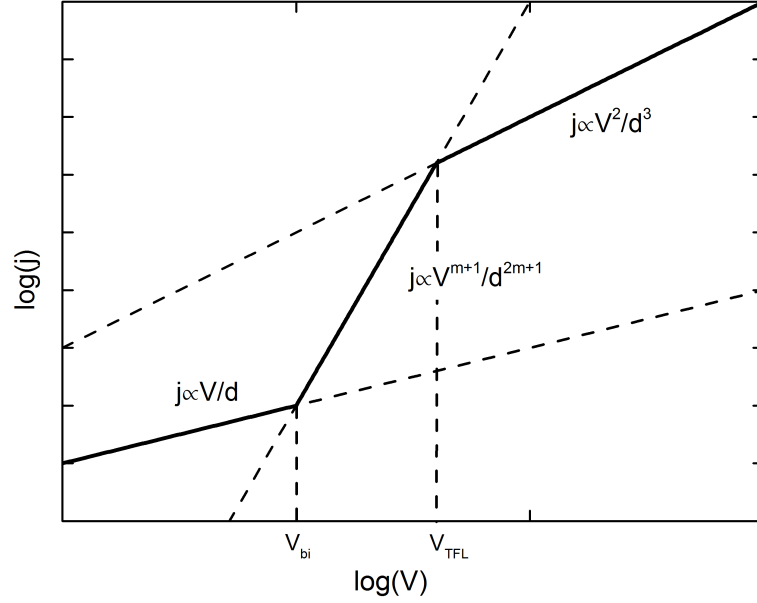
Figure 2.6: Schematic of the three different charge transport regimes (ohmic, TCLC, SCLC) described by equations 2.7, 2.8 and 2.9 assuming a field independant mobility. In real devices, there is a smooth transition between the TCLC and SCLC regime.

counterparts ($n_0 < 1 \cdot 10^{-12} \frac{1}{\mathrm{cm}^3}$ [18]) and ohmic conductivity is observed:

$$j = q\mu n_0 \frac{V}{d} \tag{2.7}$$

Here, q is the elementary charge, μ the mobility of the organic layer, n_0 the intrinsic charge carrier density, V the voltage over the device and d the layer thickness.

In disordered organic semiconductors, there are always trap states present, which can be assumed to exhibit a gaussian distribution. For voltages above the built-in potential, free charge carriers are injected into the device and the current increases abruptly. The trap states are filled and limit the charge transport, because trapped charges are immobile and cannot contribute to the current. Conduction in this voltage range is called Trap-Charge-Limited-Current (TCLC). The current density increases very steeply in this regime and can be calculed to be:

$$j_{\mathrm{TCLC}} = e\mu[E]n_0 \left(\frac{2m+1}{m+1} \right)^{m+1} \left(\frac{m}{m+1} \frac{\epsilon\epsilon_0}{eN_t} \right)^m \frac{V^{m+1}}{d^{2m+1}} \tag{2.8}$$

Here, N_t is the trap density, n_0 the intrinsic charge carrier density, ϵ_0 the vacuum permeability and ϵ the relative dielectric constant of the material. At a voltage of V_{TFL} most of the trapped states are filled and the current density characteristics

approach the so-called Space-Charge-Limited-Current (SCLC) regime. This regime is the ideal case for organic semiconductors without traps respectively only discrete trap states. The SCLC characteristics can be described by the so-called Mott-Gurney-Law [34]:

$$j_{\text{SCLC}} = \frac{9}{8} \epsilon \epsilon_0 \mu [E] \frac{V^2}{d^3} \tag{2.9}$$

The three regimes of ohmic conductivity, TCLC and SCLC are illustrated in figure 2.6, assuming a field independant mobility. In real devices there is no abrupt but a smooth transition between the TCLC and the SCLC regime. Furthermore, at higher voltages the field-dependance of the mobility (equation 2.1) becomes important so that the slope of the current density can differ from $j \propto V^2$.

For bipolar currents as they are present in OLEDs, the situation is more complicated. To be able to describe the IV-characteristics, one has to take into account the contribution of electrons and holes, their frequency dependant mobilities and recombination effects (Langevin recombination current) [31, 35, 36]. Furthermore, it has been shown that for certain combinations of materials and electrodes, at low injection voltages (in that case tunneling processes are dominant) equation 2.8 is not determined by the bulk properties of the device, but by trap states induced at the metal/organic interface [37]. The current in that case is then called injection limited, but still yields the TCLC behaviour.

2.1.3   Optical properties

In organic molecules excited states can either be generated by the absorption of light or the recombination of free charge carriers. The absorption of makes it possible to generate free charge carriers in organic solar cells, whereas the recombination of free charge carriers is the main factor for electro-luminescence in OLEDs. This section deals with the creation and transfer of these excited states.

Excitons

When an electron and hole pass each other they are attracted by the electrostatic coloumbic force and can "recombine" to form a bound electrically neutral state, which is called exciton. The strong localiziation of the charge carriers in organic semiconductors leads to relatively high exciton binding energies of about 0.1 eV-1 eV and the distance between the electron and the hole is of the order of 1nm. Such excitons are stated as Frenkel-Excitons. Spin multiplicity predicts that 25 % of the excitons are singlet-states with S=0 and 75 % are triplet states with S=1.

The Jablonski diagram in figure 2.7 presents possible transitions between the
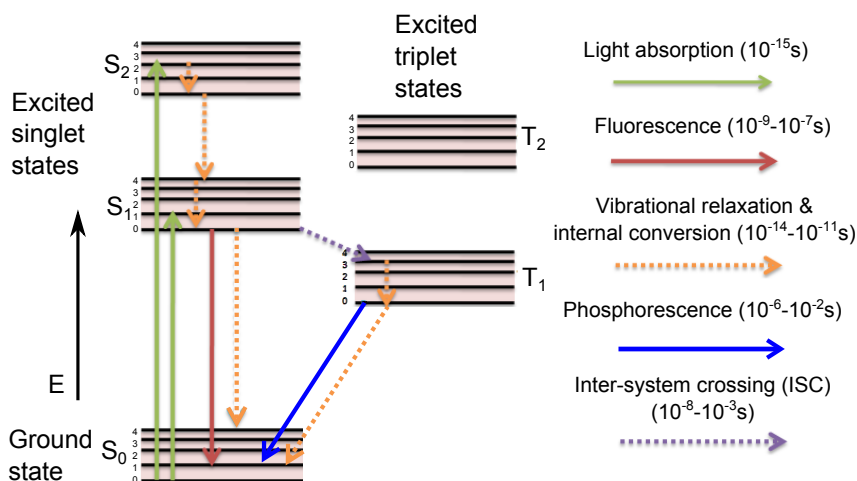
Figure 2.7: Jablonski Diagram, illustrating the electronic states of a molecule and the transitions between them. The energy is increasing in vertical direction, where the black lines denote the vibrational states. The time scale for the different types of transitions is specified. Adapted from [38] and processed.

electronic states of an isolated molecule and these are also valid for excitons. In vertical direction the states are positioned by their energy and in horizontal direction by their spin multiplicity. Solid lines present radiative and dotted lines non-radiative transitions. The green arrows represent the **absorption** of a photon which brings a molecule to its first or second excited singlet state. Subsequently the excited states transition into the lowest vibronic state by very fast **vibrational relaxations** and from higher excited to lower ones via **internal conversion** (orange arrows). The radiative decay (red arrow) of singlet states is taking place on a ns time-scale and is called **fluorescence**. In contrast, the radiative decay of triplet states with S=1 to the ground state with S=0, called **phosphorescence** (blue arrow), is quantum mechanically forbidden by transition rules ($\Delta S=0$). This inefficient transition explains the very long triplet lifetime of the order of μs to ms . Hence, the triplet states preferrably decay non-radiatively to the ground-state. The **intersystem crossing** (ISC) describes a transition from a singlet to a triplet state, which is also forbidden. Howevery, phoshporescence emission and ISC become possible when a strong spin-orbital-coupling is present, which softens the transition rules. This will be explained in the next section.

Förster resonance energy transfer

The Förster transfer describes the movement of singlet excitons from an excited "donor" molecule to an "acceptor" molecular and is based on electromagnetic dipole-

dipole interactions [39]. The efficiency of this transfer mechanism is mainly determined by the distance between the donor and the acceptor and the overlap of the emission spectrum of the donor with the absorption spectrum of the acceptor molecule. The Förster radius indiciates the distance for which the efficiency of the transfer is 50 % and is typically about 4 nm-10 nm for organic materials.

Dexter transfer

The Dexter transfer is the dominant mechanism for triplet exciton energy transfer and based on direct electron-electron interaction [40]. Hence, the molecular orbitals of donor and acceptor molecule have to overlap significantly which limits the range of this transfer mechanism to about 1nm.

Exciton diffusion

The diffusion length of excitons in organic semiconductors is determined by the lifetime of the singlet respectively triplet excitons and by the efficiency of the Förster and the Dexter transfer mechanisms [41–43]. The lifetime of triplet excitons spans from a few μs to ms and is in general much longer than that of singlet excitons. However, the dexter transfer is less efficient than the Förster transfer. For singlet excitons diffusion lengths in the nm range have been reported, whereas the ones of triplets can span from a few nm to a few μm. The knowledge that triplets can diffuse this far has to be incorporated in the process of developing highly efficient phosphorescent OLEDs.

2.2 Organic light emitting diodes

Already in 1964 Helfrich and Schneider demonstrated electroluminescence from a single semiconducting layer between two electrodes [44]. However, the required voltage was at about 100V and thus the efficiency was very low. In 1987 Tang and vanSlyke introduced an organic semiconducting double layer structure sandwiched between anode and cathode [1]. Since then, organic light emitting diodes have received much attention from researchers and industry, especially because of their potential application in flat panel displays and solid state lighting [45, 46].

2.2.1 Working principle

In figure 2.9 (a) the energy level alignments and electronic paramters of a simple single layer OLED under an applied DC voltage V are depicted. Before a current can flow, the build-in potential has to be overcome, which for an OLED in the most cases is equal to the difference of the electrode work functions $V_{bi} = \Phi_A - \Phi_C$. With increasing voltage, holes are injected from the anode into the HOMO and from the cathode into the LUMO of the organic layer, where the alignment of the HOMO/LUMO levels lead to a preferred hopping into the direction of the electrodes. The injection depends on the energies of the LUMO and the HOMO levels relative to the work functions of the electrodes as was described in 2.1.2. After the charge carriers are injected, holes and electrons in the organic layer are able to recombine forming excitons which can decay radiatively. This simple structure usually does not yield balanced charge injection and transport, resulting in charges flowing through the organic layer without recombining (dark current) [47] and thus a decreased efficiency. The introduction of additional layers can resolve the issue of overflow charges and is illustrated in figure 2.9 (b). In this strcture a hole-transporting-layer (HTL), an electron transporting-layer (ETL) and a light emitting layer (EML) are combined. The energy levels and properties of the materials are chosen for good charge injection and balanced charge transport. Additionally, the large energy barriers for holes and electrons at the EML/ETL respectively HTL/EML interfaces efficiently confines the charge carriers inside the EML. The result is a high recombination efficiency. For increased overall efficiencies, charge-inejecting, charge-blocking, exciton-confining, and p- and n- doped transport layers can additonally be implemented [48].
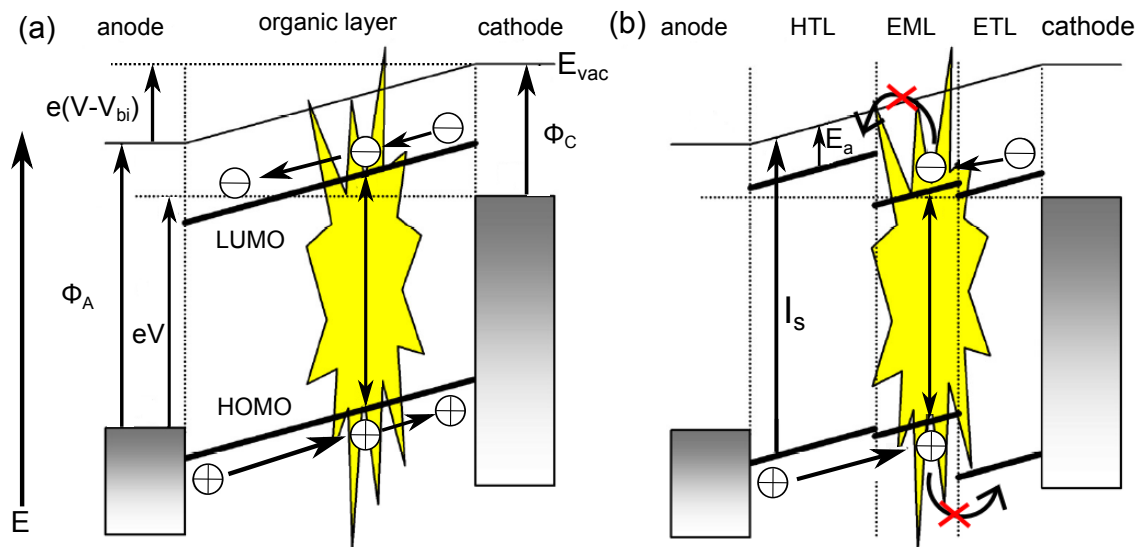
Figure 2.8: Simplified illustration of the working principle of an OLED under an applied voltage V. (a) OLED consisting of only one organic layer and (b) OLED consisting of three organic layers, namely a hole-transport-layer (HTL), an electron transport layer (ETL) and an emitting layer (EML). Details in the text. Taken from [49] and processed.

Fluorescent and phosphorescent recombination

Assuming that all of the injected charge carriers recombine and there is a balanced charge transport, the efficiency of an OLED is dependant on the number of generated excitons which result in the emission of light. For materials based on small molecules, simple spin statistics predict that 25% of the generated excitons occupy singlet states whereas 75% occupy triplet states [43, 50]. In fluorescent devices, the triplet states preferentially decay non-radiatively and the quantum quantum efficiency limited to 25% (see left side of figure ??). For certain polymers the singlet-to-triplet ratio was reported to vary so that higher fluorescent efficiencies are possible [51, 52].

In 1998, Baldo et al. showed that phosphorescent dyes (metal-organic complexes with heavy transition metals), which are doped into an organic host matrix, result in a strong enhancemant of OLED efficiency [2]. The central heavy metal atom leads to a strong spin-orbit-coupling (SOC) between the host and dopant. This gives rise to efficient dexter transfer of the triplets from the host to the dopant. Furthermore, excited singlet state on the dopant molecules can efficiently be transferred to their triplet state by intersystem crossing (ISC) [41]. The different energy transfer mechanisms in a host-dopant system are illustrated in figure ??. The triplets can now decay radiatively to the ground state resulting in phosphorescence. In principle the
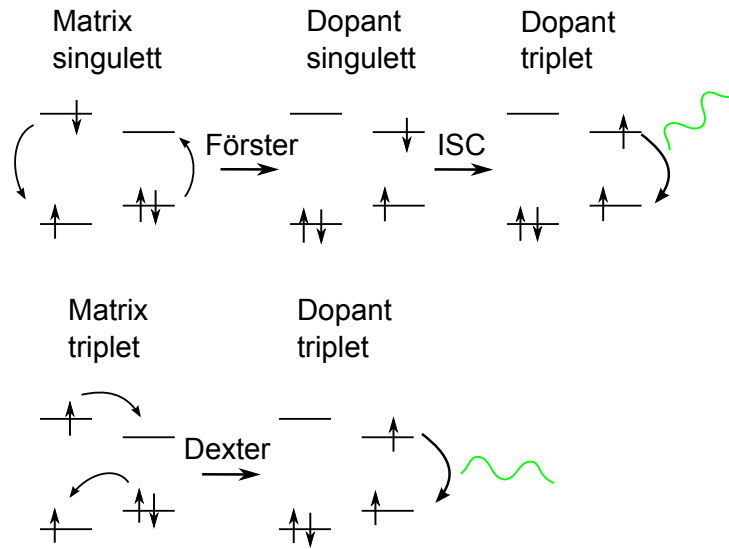
Figure 2.9: Detailed energy transfer mechanisms from an organic matrix to a phosphorescent dopant for singlet- and triplet excitons [50].

intrinsic quantum efficiency in such devices can reach up to 100% [53, 54].

Another possibility for the generation of excitons in a host-dopant system can be achieved by direct charge trapping. Here, the holes respectively electrons are transferred from the HOMO respectively LUMO level of the host to that of the dopant and excitons are directly generated on the dopant molecule. Charge trapping can significantly influence the electric characteristics and efficiency of OLED devices [55].

Radiometric and photometric quantities

For the characterization of electromagnetic radiation there are two different systems, namely radiometry and photometry. Every quantity in one system has an analogous in the other system, called photometric and radiometric quantities [56]. They are presented in table 2.1. The radiometric quantities are based on the absolute power emitted from a lightsource and described by the SI-unit Watt. For photometric quantities every wavelength is weigted according to the sensivity of the human eye

Table 2.1: Radiometric and the corresponding photometric units.

Radiometric quantity	SI-unit	Photometric quantiity	SI-unit
Radiant flux Φ_e	W	Luminous flux Φ_v	Lumen lm
Radiant intensity I_e	W/sr	Luminous intensity I_v	Candela cd=lm/sr
Radiance L_e	W/m^2/sr	Luminance L_v	cd/m^2

to it and described by the SI-unit lumen. The corresponding quantity to radiant flux
in the photometric system is the luminous flux and can be expressed as:

$$\Phi_v = K_m \int\limits_{380\text{nm}}^{780\text{nm}} \frac{\text{d}}{\text{d}\lambda} \Phi_e \left(\lambda\right) \cdot V \left(\lambda\right) \tag{2.10}$$

$V\left(\lambda\right)$ is the luminous function which describes the average spectral sensitivity of the
human eye with its maximum at a wavelength of $555\,\text{nm}$. K_m equals $683\ \text{lm}\,\text{W}^{-1}$
and is determined by the definition of the lumen to be unity at a radiant energy of
$1/168\,\text{W}$ at this wavelength. The luminous intensity is defined as the luminous flux
in a particular direction per unit solid angle and the luminance relates the luminous
intensity of a light source to its emitting area.

Quantum efficiency

After the injection of electrons and holes from the electrodes, the charge carriers
recombine in the EML to produce photons. The internal quantum efficiency η_{int} is
defined as the ratio of the total number of photons generated within the organic
emitter to the number of injected electrons. The external quantum efficiency η_{eqe} is
defined as the ratio of photons coming out of the device to the number of injected
electrons and can be related to the internal quantum efficiency with the relation [58]:

$$\eta_{\text{eqe}} = \frac{N_{\text{ext}}}{N_{\text{e}}} = \chi_{\text{out}} \cdot \eta_{\text{int}} = \chi_{\text{out}} \cdot \gamma \eta_{ex} \phi_p. \tag{2.11}$$

Here χ_{out} is the out-coupling efficiency of an OLED device, γ the electron-hole charge
balance factor, η_{ex} the number of the generated excitons which result in radiative
decay and ϕ_p the intrinsic quantum efficiency for radiative decay. For a normal
glass substrate without any outcoupling-enhancing techniques $\chi_{\text{out}} \approx 0,2$. Light
which is emitted at angles above a certain critical angle θ_{C} which accounts for about
80% of generated photons is lost in wave-guided modes due to the difference of the
refractive indexes of glass substrate, ITO and organic materials. It is either trapped
inside the glass substrate or emitted from the edges [57]. These loss mechanisms are
illustrated in figure 2.10. The intrinsic quantum efficiency for some phosphorescent
dye materials reaches values near 100%, which means that the non-radiative loss is
very small [48, 59].

Shukla et al. recently presented a simple method to estimate the external quan-
tum efficiency and the calculated values showed good agreement with measured val-
ues [60]. For this approach, only the spectral emission pattern and the LIV charac-
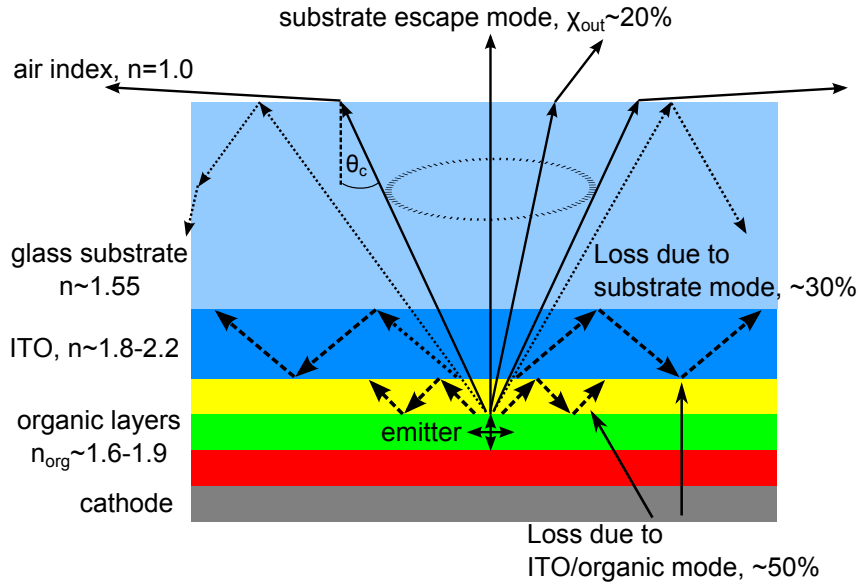
Figure 2.10: Schematic of the light propagation in various modes in a multilayer OLED-device due to the different refractive indexes of substrate, ITO and organic layers. Only light emitted at angles smaller than θ_C can escape from the surface. Adapted from [57].

teristics of the device have to be measured. With equation 2.10, one can determine the number of photons emitted at a wavelength λ with optical power of 1 lumen $(\Phi_v(\lambda) \overset{!}{=} 1\mathrm{lm})$:

$$N_{1\mathrm{lm}}(\lambda) = \frac{\lambda}{683 \cdot V(\lambda) \cdot \mathrm{hc}} \tag{2.12}$$

OLEDs are in first approximation lambertian radiators, for which the total luminous flux F_{tot} in the half sphere from an emitter with area A can be calculated from the peak luminance L_{tot} measured in forward direction:

$$F_{\mathrm{tot}} = \pi L_{\mathrm{tot}} A \tag{2.13}$$

At a certain wavelength λ the total luminous flux can be expressed as

$$F_{\mathrm{tot}}(\lambda) = \pi L(\lambda) A. \tag{2.14}$$

Furthermore, as the luminance is directly proportional to the emission intensity of an OLED, we can write

$$L(\lambda) = \alpha V(\lambda) I(\lambda) \tag{2.15}$$

, with α being a constant. Combining equation 2.12-2.15 and integrating over the

visible spectrum the total number of photons emitted externally by the device can
be calculated to be:

$$N_{ext} = \int\limits_{380nm}^{780nm} N_{1lm}(\lambda) \cdot F_{tot}(\lambda) \, d\lambda = \frac{\pi A}{683 \cdot hc} \cdot \alpha \int\limits_{380nm}^{780nm} I(\lambda) \lambda d\lambda. \tag{2.16}$$

The constant α can be obtained by taking measurements of the total luminance L_{tot}
in forward direction and the emission spectrum :

$$L_{tot} = \int\limits_{380nm}^{780nm} L(\lambda) \, d\lambda = \alpha \int\limits_{380nm}^{780nm} I(\lambda) \cdot V(\lambda) \, d\lambda. \tag{2.17}$$

Now substituting the value of α in 2.16 and calculating the number of injected
electrons by measuring the current through the device $N_e = \frac{I_D}{e}$ we can determine
the external quantum efficiency with equation 5.2:

$$\eta_{eqe} = \frac{\pi A \cdot I_D \cdot L_{tot}}{683 \cdot ehc} \cdot \frac{\int_{380nm}^{780nm} I(\lambda) \cdot \lambda d\lambda}{\int_{380nm}^{780nm} I(\lambda) \cdot V(\lambda) \, d\lambda} \tag{2.18}$$

The luminous or power efficacy η_P (unit lm/W) of an OLED is used as a measure
of how efficient it converts electrical power into visible light and can be calculated
using equation 2.13:

$$\eta_P = \frac{\pi \cdot L_{tot} \cdot A}{U_D \cdot I_D}. \tag{2.19}$$

In chapter 5, equations 2.18 and 2.19 are used to compare the efficiencies of the
analyzed OLEDs.

2.2.2   Quenching effects in phosphorescent OLEDs

The strong increase of the quantum efficiency for phosphorescent OLEDs (PHOLEDs)
was a major breakthorugh, but they often exhibit a steady decrease of efficiency at
higher current densites, known as efficiency roll-off. Due to the long lifetimes of
many phosphorescent dyes of the order of μs, there exist some quenching mecha-
nisms which result in non-radiative decay of excitons. These will be described in the
following [61]:

Exciton-exciton annihilation

The high exciton density and their diffusion processes in PHOLEDs leads to a high
probability of two excitons interacting before they decay radiatively [62]. Exciton-

exciton annihiliation occurs when this interaction results in a non-radiative decay. In PHOLEDs the excited singlet excitons are efficiently transferred to the triplet state of the dopant so that singlet-singlet-interactions can be neglected. The governing process is Triplet-Triplet-Annihilation (TTA) [63,64]:

$$^3D^* + {}^3A^* \Rightarrow {}^1D + {}^3A^* \tag{2.20}$$

The interaction between an excited triplet donor $^3D^*$ and an excited triplet acceptor $^3A^*$ results in a transition of the donor to the singlet groundstate ^1D. This process scales with the square of triplet exciton density and is often the limiting factor for the OLED quantum efficiency at high brightness.

Triplet-polaron annihiliation

Another quenching process is caused by the interaction between triplets and trapped charges and is called triplet-polaran annihilation (TPA). Depending on the type of charge involved, it can be expressed as [63]:

$$^3D^* + A^{*\overset{+}{-}} \Rightarrow {}^1D + A^{*\overset{+}{-}} \tag{2.21}$$

This process scales linearly with the triplet exciton density and should thus be less relevant in comparison to TTA for high current densities.

Diffusion limited exciton quenching

During diffusion through the device, excitons can be trapped by non-radiative defect states which are always present in organic thin films or develop under OLED operation due to chemical dissocation of the host matrix molecules [42,62]. Furthermore, in the vicinity of metal electrodes strong quenching effects have been observed. It is important to confine the excitons into the EML by implementing exciton blocking layers and to use stable host materials with few non-radiative defect states.

2.2.3 Degradation phenomena

For modern applications OLED devices should provide an adequate device stability and half-lifes of about 10000h at a luminance of $100\frac{cd}{m^2}$. Commonly, degradation in an OLED device results in a decrease in luminance over time and is divided into three different modes, which are shortly presented here [65,66]:

Dark spots

Dark spot degradation refers to the decrease in luminance of an OLED as a result of the formation of nonemissive defects within the emissive area of the device. It is an ambient-air-induced phenomenon and is mostly caused by the evolution of structural defects in the OLED layers, where local oxidation or delamination of the metal cathode play a major role. The density of such structural defects can be reduced by a proper pretreatment and cleaning of the ITO subtrates. Furthermore, the growth of existing dark-spots can effectively be minimized by encapsulation of the active area in inert conditions [47,67].

Catastrophic failure

This degradation phenomen refers to a sudden decrease or complete loss of luminance of a device caused by electrical shortcuts and the resulting large leakage currents. These so called hot spots result from morphological defects in the different layers which can lead to the decomposition of the organic layers during device operation. Materials with good film-forming- and layer properties as well as a good control over the fabrication process can reduce their occurence [48,65,68].

Intrinsic degradation

The intrinsic degradation refers to the decrease in luminance of an OLED during device operation, which can be directly attributed to an intrinsic decrease of the electroluminescence quantum efficiency of a device. As the name already suggests, it depends on the intrinsic properties of the used materials used and the employed OLED architecture. There are a number of models trying to identify the reasons for this type of degradation, but it is still not completely understood [47, 48, 69–71]. In multilayer PHOLEDs, the interplay between the host and the dye in the EML as well as between the host molecules and that of adjacent layers both have an inflluence on the strength of the degradation. In general it can be said that a good charge balance and a broad distribution and confinement of the excitons inside the EML can efficientely reduce intrinsic degradation. Thus, mixed host devices often show superior lifetimes compared to ones with a single-host as will be explained in the next section.

For many display applications, low luminance levels of about $100 - 1000 \frac{\text{cd}}{\text{m}^2}$ are most common and lifetimes of more than 100.000 hours are possible with certain OLED structures [72]. However, it is not practical to measure devices over such a long time so that the lifetimes are normally determined at higher brightness and then extrapolated to lower luminance levels. Fery et al. recently justified the use of

the so called stretched exponential decay (SED) [73] as a fit function to describe the lifetime of OLEDs and furthermore concluded that the annihilation of the emissive centers is the main contribution to the degradation of OLEDs [71]. The normalized decrease in luminance in this approach is described by:

$$L'(t) = \frac{L(t)}{L_0} = \exp\left[-\left(\frac{t}{\tau}\right)^{\beta}\right] \text{ with } \tau_{1/2} = \ln(2)^{\frac{1}{\beta}} \cdot \tau \qquad (2.22)$$

The SED incorporates an additional parameter β to be able to describe both, the rapid initial decay and the long-term degradation typically seen for OLED devices. Furthermore, for the same OLED structure β has been shown to stay constant for different initial luminances L_0, i.e. different current densities [71, 74].

By determining the lifetimes at different current densities with equation 2.22, an empirical lifetime acceleration function can be used to extrapolate the lifetimes to lower luminance values [70, 71, 74, 75]:

$$\tau_{1/2} = \frac{\text{const}}{(L_0)^{\text{n}}} \qquad (2.23)$$

L_0 is the initial luminance and n is the lifetime acceleration constant, which incorporates the fact that the enhanced lifetime reduction at higher luminance levels - which depends on the OLED structure and materials used - exhibits a nonlinear behaviour.

2.2.4 Mixed host structures

A conventional PHOLED-structure consists of a minimum of three organic layers, namely the HTL, the EML (consisting of a host matrix and a dopant) and the ETL. The electroluminescence takes place in the doped EML, where the host matrix is responsible for the charge transport and the dopant for the emission of light. In general, the host matrix of the EML has to fulfill a number of requirements with respect to the dopant to allow for efficient long-living devices, some of which are [49, 59]:

- The emission spectrum of the host matrix needs to overlap with the absorption spectrum of the dopant significantly to ensure efficient Förster transfer from the singlet states of the host to the dopant.

- A broad recombination zone is beneficial for the luminous efficacy and operating lifetime of OLEDs. In general, it requires a host matrix that is able to
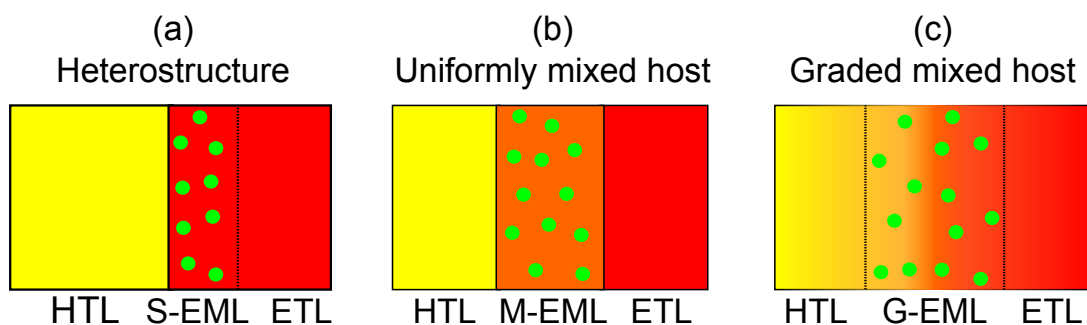
Figure 2.11: Schematic diagram of the hole-, electron and emissive layer of a device with (a) a conventional heterostructure, (b) a uniformly mixed host structure and (c) a graded mixed host structure. The green circles denote the phosphorescent dye. The concentration ratio between the HTL- and ETL molecules is illustrated by the mixing of the colors.

transport both, electrons and holes (bipolar charge transport) so that charge accumulations at one of the interfaces are effectively suppressed.

- The lowest triplet state of the host should lie energetically above that of the dopant so that all triplets can effectively be harvested by the dopant. Furthermore, the triplet energies of adjoining layers should lie reasonably high so that exctions are confined inside the EML.

There are different approaches for structuring the EML-layer in a PHOLED, including a heterostructure (HS), a uniformly mixed host structure (UMH) and a graded mixed host structure (GMH). An OLED with a heterostructure is illustrated in figure 2.11 and the single-EML (S-EML) is defined by doping the ETL material in the vicinity of the HTL/ETL interface (S-EML) with a phosphorescent dye (green circles). A uniformly mixed host structure is illustrated in figure 2.11 (b) and can be achieved by uniformly mixing of the HTL and ETL material in the doped region (M-EML). A third possibilty is to define a gradual transition so that the mixing ratio between HTL and ETL material is changing continuously from one side to the other in the doped region (G-EML) as illustrated in figure 2.11 (c). These approaches are described in the following:

Heterostructure

In a conventional HS, the energy gaps between the the mostly hole transporting HTL and the mostly electron transporting S-EML materials lead to a charge build-up and a high exciton density at the abrupt HTL/EML interface. The recombination zone is expected to be confined to a narrow region at the interface, which

can adversely affect the device lifetime. This is because only a few molecules are responsible for generating excited states so that recombination-related degradation processes are accelarated [71]. Furthermore, the high exciton density leads to enhanced triplet-triplet-annihilation quenching processes [63]. Additionally, the field dependent mobilites of the HTL and ETL materials can lead to a loss of charge balance with increasing current density, which results in the presence of excess charges at the interface. This increases the voltage drop across the interface so that higher driving voltages are needed. At very high electric fields some charge carriers may even overcome the energy barrier at the interface and be leaking out of the EML.

In general also an ambipolar material for the S-EML can be used to reach a good charge balance and broaden the recombination zone. However, it is difficult to find single host bipolar materials with high triplets energy especially for deep blue PHOLEDs. Furthermore, a high triplet energy is normally accompanied by a large HOMO-LUMO gap. In that case, adjacent HTL and ETL materials with suitable HOMO- and LUMO levels have to be chosen to achieve efficient charge injection into the EML, which makes the device structure more complex [59, 76].

Mixed host structures

In a mixed host, both of the materials have to feature a higher triplet energy with respect to the dopant. However, the HTL is solely responsible for good hole injection and transport and the ETL likewise for electrons. This is possible because the weak van-der-Waals coupling between the organic materials leaves the molecular orbitals, i.e. the charge transport characteristics, unaltered [77]. A high HOMO-LUMO-gap of the single materials thus does not pose a problem, because only the HOMO respectively LUMO level have to be chosen for good charge injection into the EML.

In a uniformly mixed host structure (UMH), despite the concentration step of the HTL respectively ETL molecules at the interfaces of the EML, there are continuous pathways for electrons and holes into the EML. In the optimal case, the mixing of the mostly electron transporting and mostly hole transporting material results in a bipolar current so that the recombination zone is broadened and charge accumulations at the interfaces are suppressed. Yet, there is an energy barrier for electrons at the HTL/EML interface respectively for holes at the EML/ETL interface so that the charge carriers are efficiently confined inside the EML. However, the mixing ratio of the materials has to be fine-tuned to reach a good charge balance. Furthermore, the field dependant mobilities of both materials can result in a loss of charge balance with increasing current density [78]. In the last decade, OLEDs incorporating a uniformly mixed host structure with improved efficiency, low roll-off and improved

lifetime have been reported [7–9, 79–94]. In addition, this approach for the EML can also be applied to solution processed devices [9, 87, 95].

In devices with a graded mixed host structure (GMH) there are no energetic barriers for the respective charge carriers at the interfaces of the G-EML so that holes and electrons are efficiently injected into the EML. The graded structure results in a gradual change of the mobility for either charge carrier so that at the EML/ETL interface the mobility for holes and at the HTL/EML interface the mobility for electrons is very low. This self-balancing nature of the effective mobility shifts the recombination zone away from the interfaces and charge accumulations are efficiently suppressed [96]. Furtermore, the voltage drop in the EML is lowered and a reduced driving voltage can be obtained. Using a G-EML structure, high efficiencies, low roll-off and long lifetimes have been reported recently [48, 49, 97–102]. The main drawback of this OLED structure is the complex device fabrication.

2.3 Fundamentals of impedance spectroscopy

In this section the basic principles needed for the understanding of the impedance measurements performed in this thesis are presented.

2.3.1 Basic principles

Impedance is defined as the opposition of the flow of an alternating current (AC) in a complex electrical circuit. In general, impedance spectroscopy is used to measure the dielectric properties of a device as a function of frequency. The AC current induces an external electrical field which interacts with the electric dipole moments in the device defined by its permittivity. To ease analysis and to be able to understand the intrinsic origins of the measured dielectric properties, equivalent circuits are introduced. These consist of linear, passive elements - commonly resistor, capacitor and inductor - and the equivilent circuit should inhibit most of the electrical characteristics of a device. If a suitable equivalent circuit has been found, the properties of the single elements can be associated with the structure of the device to determine its properties [103].

In figure 2.12 the principle of an impedance measurement is depicted. An alternating voltage (AC voltage) - which can in general be overlaid by a constant DC voltage - applied to an electrical circuit made of passive elements results in an alternating current with the same frequency:

$$V = V_0 + V_1 \sin(\omega t) \Rightarrow I = I_0 + I_1 \sin(\omega t + \Delta\phi) \tag{2.24}$$

Here, V_0 and I_0 represent the DC contribution, V_1 and I_1 the AC amplitude and $\Delta\phi$ the phase shift between voltage and resulting current. For small AC amplitudes, which are commonly used for impedance spectroscopy ($V_1 \approx 20 - 100\,\mathrm{mV}$), the impedance of such a circuit can be calculated using the small-signal-model [103]:

$$Z = |Z|\exp^{i\phi} = \frac{V_1}{I_1}\left[\cos\left(\Delta\phi\right) + i\sin\left(\Delta\phi\right)\right] \tag{2.25}$$

$$= \mathrm{Re}(Z) + i\mathrm{Im}(Z) = B + iX \tag{2.26}$$

Equation 2.25 and 2.26 represent the polar respectively cartesian form of the impedance. In the cartesian form, the real part B describes the resistance of a device. The imaginary part X is the reactance and describes a devices opposition to an AC voltage respectively current due to an electric field (capacitive response) or magnetic field
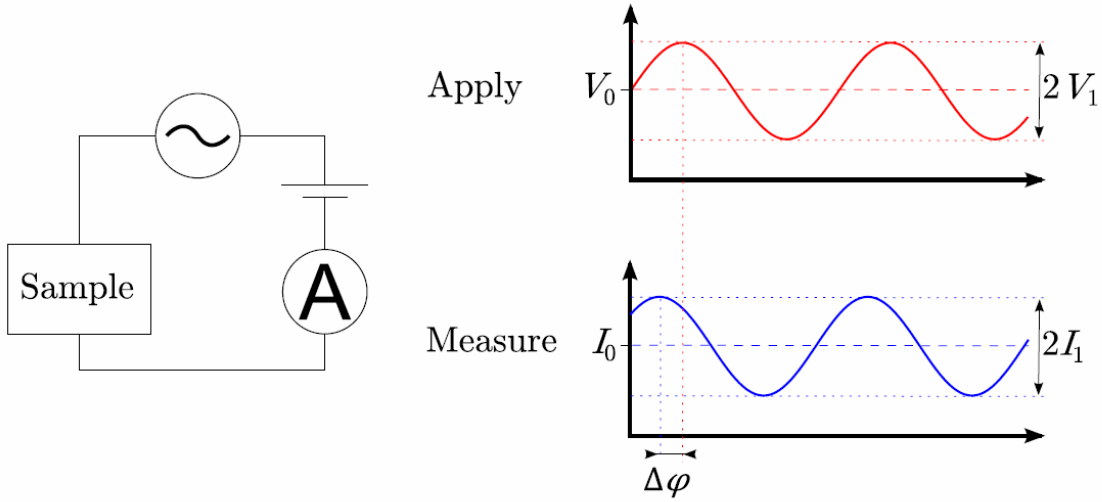
Figure 2.12: Principle of an impedance measurement.

(inductive response). A complete impedance spectrum is measured by varying the angular frequency ω over a bread region. In this thesis, thin organic semiconducting layers sandwiched between two electrodes are analyzed by impedance spectroscopy in the frequency range between 1mHz and 10MHz. The equivalent circuit can be described by a parallel circuit of a resistor and capacitor. The resistance R is defined as

$$R = \frac{d}{A\sigma}, \tag{2.27}$$

with conductivity σ, active area A and layer thickness d. The capacitance is equal to

$$C = \epsilon_0 \epsilon_r \frac{A}{d}, \tag{2.28}$$

where ϵ_0 is the vacuum permittivity ($\epsilon_0 \approx 8.85 \cdot 10^{-12} \frac{\text{F}}{\text{m}}$) and ϵ_r the relative permittivity. The impedances of these two components are defined as

$$Z_R = R \tag{2.29}$$

and

$$Z_C = \frac{1}{i\omega C}. \tag{2.30}$$

Neglecting the inductance [15], the total impedance of an ideal single layer can be
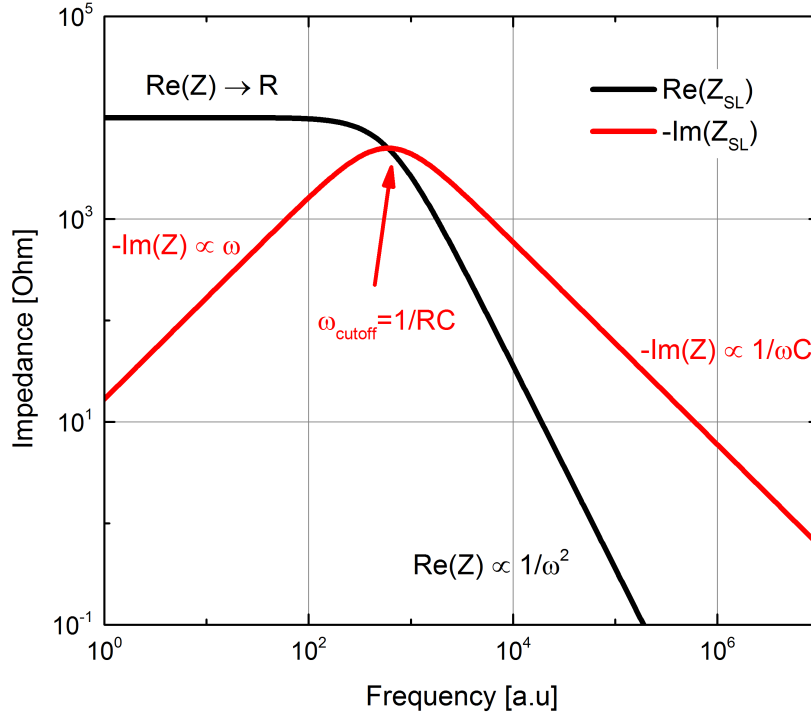
Figure 2.13: Impedance spectrum of an ideal single layer device.

expressed as:

$$Z_{\mathrm{SL}} = \frac{1}{\frac{1}{R} + i\omega C} = \frac{R}{1 + \omega^2 R^2 C^2} - \frac{i\omega R^2 C}{1 + \omega^2 R^2 C^2} \tag{2.31}$$

$$= \frac{d}{A} \cdot \frac{1}{\sigma + i\omega\epsilon_0\epsilon_r} \tag{2.32}$$

The corresponding spectrum is depicted in figure 2.13. At low frequencies most of the current is carried by the resistor and the impedance is governed by $Z_{\mathrm{SL}}(\omega \to 0) \approx R$. The negative imaginary part rises linear with ω (see equation 2.31) and the part of the current carried by the capacitance increases. -Im(Z) reaches the maximum at the cut-off frequency $\omega_c = \frac{1}{RC}$, the point where Re(Z)=-Im(Z)=$\frac{R}{2}$. For higher frequencies most of the current is carried by the capacitance and the spectrum is governed by $Z_{\mathrm{SL}}(\omega \to \infty) \approx -\frac{i}{\omega C}$.

For devices with more than one layer, the individual layers are connected in series so that their impedances can be summed. Furtermore, for a real device, there is always a contact resistance R_0 present in series with the ideal device. It accounts for the resistance of the devices electrical leads and for their connection to the measuring
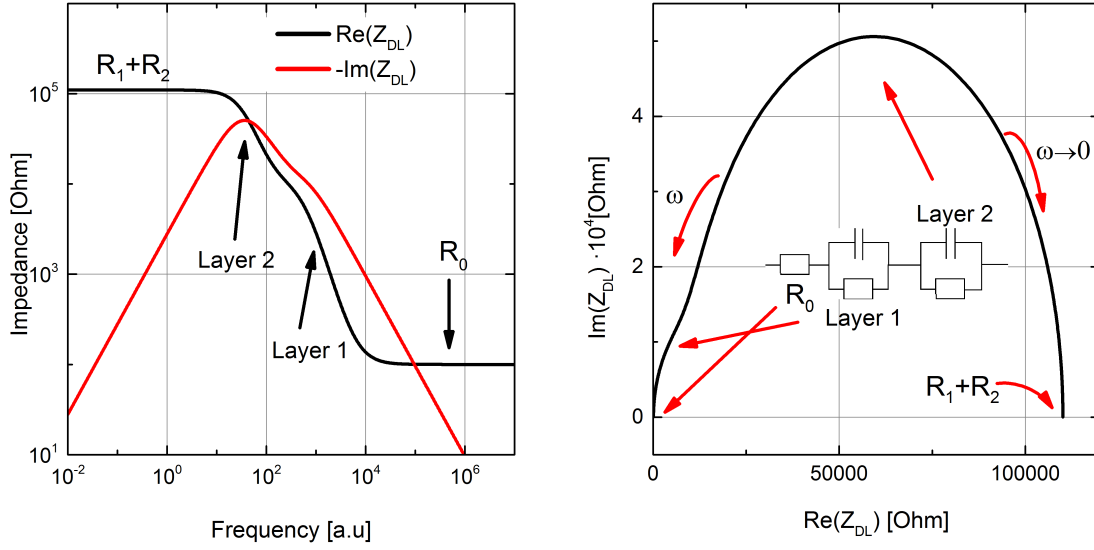
(a) Impedance spectrum of a typical double layer device. At low frequencies $\mathrm{Re}(Z_{\mathrm{DL}})$ yields the combined resistances.

(b) Cole-Cole plot representation of the impedance. The structures which can be attributed to the different parts of the equivalent circuit are shown.

Figure 2.14

instrument and to the organic layers. For a double layer device this results in:

$$Z_{\mathrm{DL}} = \frac{1}{\frac{1}{R_1} + i\omega C_1} + \frac{1}{\frac{1}{R_2} + i\omega C_2} + R_0 \tag{2.33}$$

$$= \frac{d_1}{A} \frac{1}{\sigma_1 + i\omega\epsilon_0\epsilon_{r1}} + \frac{d_2}{A} \frac{1}{\sigma_2 + i\omega\epsilon_0\epsilon_{r2}} + R_0 \tag{2.34}$$

A typical double layer impedance spectrum with $R_0 = \frac{R1}{100} = \frac{R1}{10^4} = 100\Omega$ and $C_2 = C_1$ is presented in figure 2.14a. Corresponding to the different layers, $\mathrm{Re}(Z_{\mathrm{DL}})$ shows two plateaus and $-\mathrm{Im}(Z_{\mathrm{DL}})$ two overlapping peaks. In figure 2.14b the Cole-Cole impedance plot for the same parameters is depicted and the shapes corresponding to the different layers are pointed out. In addition to these representations, the capacitance C and conductance $G = \frac{1}{R}$ of a device can be calculated using the fact that the relative dielectric function by definition is proportional to the inverse of the complex impedance [103]:

$$\epsilon_r(\omega) = \epsilon_r'(\omega) + i\epsilon_r''(\omega) = \frac{1}{i\epsilon_0\omega Z} \frac{A}{d} \tag{2.35}$$
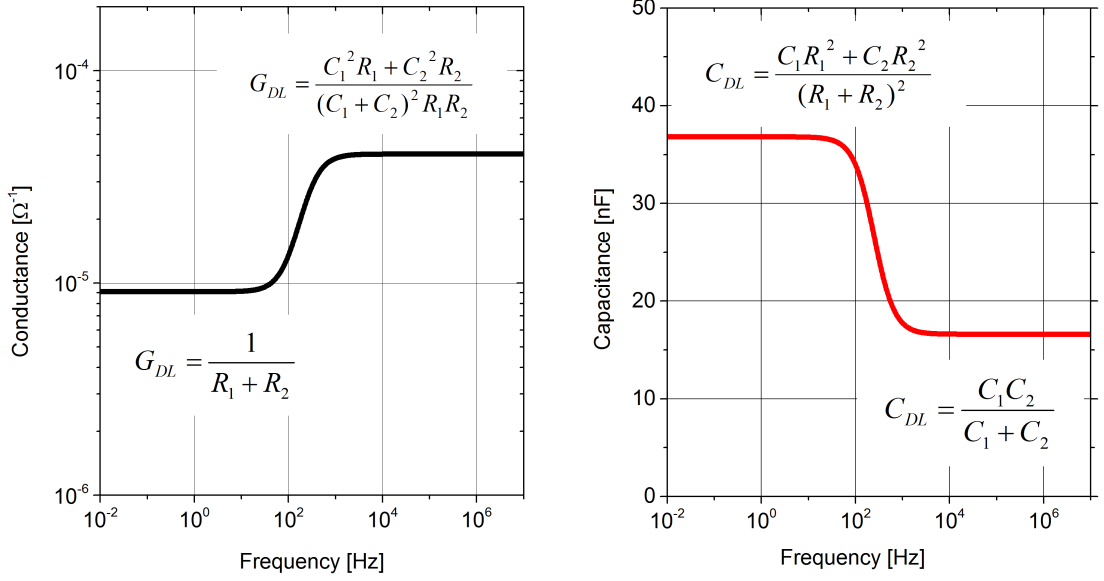
Figure 2.15: Typical behaviour of the Conductance (left) and Capacity (right) in a double layer device. The values for the limits of very high and very low frequencies are specified.

The conductivity σ is connected to the relative dielectric loss $\epsilon_r''(\omega)$ as:

$$\epsilon_r''(\omega) = -\frac{\sigma}{\omega\epsilon_0} \tag{2.36}$$

Equations 2.35 and 2.36 together with equations 2.27 and 2.28 result in the frequency dependant capacitance and conductance:

$$C = \frac{1}{\omega}\frac{-\mathrm{Im}(Z)}{\left[\mathrm{Re}(Z) - R_0\right]^2 + \mathrm{Im}^2(Z)} \tag{2.37}$$

$$G = \frac{\mathrm{Re}(Z) - R_0}{\left[\mathrm{Re}(Z) - R_0\right]^2 + \mathrm{Im}^2(Z)} \tag{2.38}$$

For a double layer device, the frequency dependant total capacitance und conductance can be calculated by inserting the real and imaginary parts of equation 2.33 in equation 2.37 and 2.38:

$$C_{\mathrm{DL}} = \frac{C_1 R_1^2 + C_2 R_2^2 + C_1 C_2 \left(C_1 + C_2\right) R_1^2 R_2^2 \omega^2}{\left(R_1 + R_2\right)^2 + \left(C_1 + C_2\right)^2 R_1^2 R_2^2 \omega^2} \tag{2.39}$$

$$G_{\mathrm{DL}} = \frac{R_1 + R_2 + \left(C_1^2 R_2 + C_2^2 R_2\right) R_1 R_2 \omega^2}{\left(R_1 + R_2\right)^2 + \left(C_1 + C_2\right)^2 R_1^2 R_2^2 \omega^2} \tag{2.40}$$

For analyzing the behaviour of C and G at very low and very high frequencies these equations can be evaluated at the limits of $\omega \to 0$ and $\omega \to \infty$:

$$C_{\mathrm{DL}}\left(\omega \to 0\right) = \frac{C_1 R_1^2 + C_2 R_2^2}{\left(R_1 + R_2\right)^2} \; \text{ and } \; G_{\mathrm{DL}}\left(\omega \to 0\right) = \frac{1}{R_1 + R_2} \tag{2.41}$$

and

$$C_{\mathrm{DL}}\left(\omega \to \infty\right) = \frac{C_1 C_2}{C_1 + C_2} \; \text{ and } \; G_{\mathrm{DL}}\left(\omega \to \infty\right) = \frac{C_1^2 R_1 + C_2^2 R_2}{\left(C_1 + C_2\right)^2 R_1 R_2} \tag{2.42}$$

At low frequencies, both capacitors are blocking and do not contribute to the conductance. The equivalent circuit can be approximated by two resistors in series so that the conductance $G_{\mathrm{DL}}(\omega \to 0)$ approaches the inverse of the sum of their resistances. Thus, the capacitance at low frequencies is determined by the resistors. As can be seen in equation 2.41, for $R1 >> R2$ the capacitance approaches $C_{\mathrm{DL}}(\omega \to 0) = C_1$

For high frequencies, the resistors are short circuited by the capacitors and C_{DL} approaches the capacitance of two capacitors in series. Thats why $G_{\mathrm{DL}}/\omega \to \infty)$ depends on the capacitors. In figure 2.15 the conductance and capacitance which correspond to the impedance spectrum in figure 2.14a are depicted.

2.3.2   AC conductivity of organic materials

In 1992 Joscher demonstrated that the AC response of disordered materials, e.g. glasses, ionic conductors and organic semiconductors, in a wide frequency range can be described by the so-called universal dielectric response (UDR) [104]. It is divided in a constant DC contribution and a frequency dependant AC contribution with a power-law behaviour:

$$\sigma(\omega) = \sigma_{\mathrm{DC}} + \sigma_{\mathrm{AC}} \cdot \omega^s \; \text{ with } \; 0 < s < 1 \tag{2.43}$$

The power-law behaviour origins in fact that the charge transport in disordered materials is dominated by hopping (or tunneling) processes between a distribution of localized states [105, 106]. For organic semiconductors at room temperature, a value of s between 0.6 and 1 can be expected [107, 108]. Using the Kramers-Kronig-relationship and the fact that the imaginary part of the dielectric function is linked to the conductivity ($\epsilon'' \propto \frac{\sigma(\omega)}{\omega}$), the frequency dependence of the dielectric constant
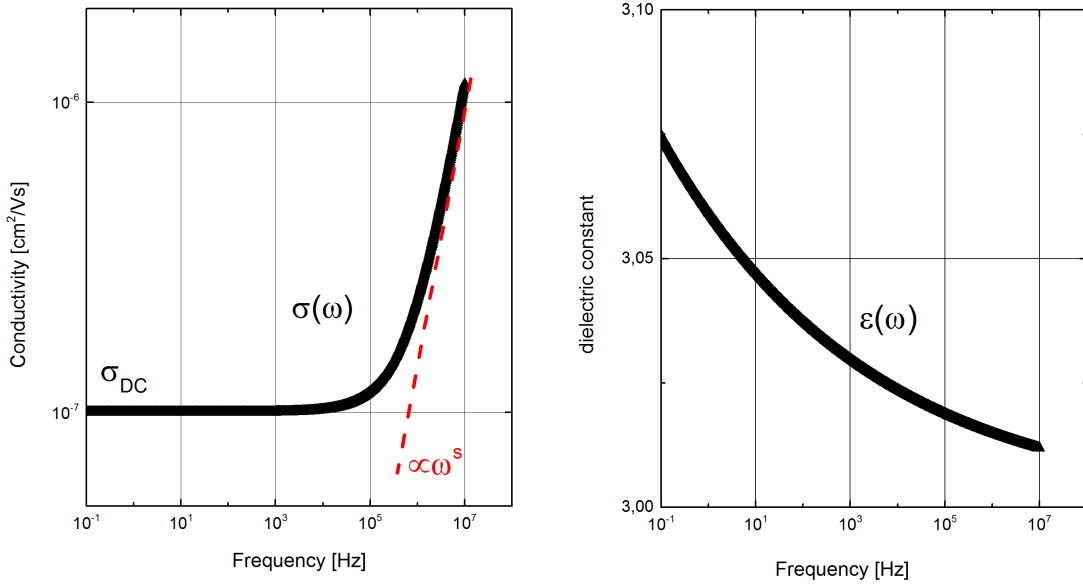
Figure 2.16: Typical frequency dependent UDR behaviour of the conductivity (left) and dielectric constant ϵ_r (right) in an organic semiconductor.

can be calculated [109, 110]:

$$\epsilon_r(\omega) = \epsilon_\infty + \frac{\sigma_{\mathrm{AC}}}{\epsilon_0} \cdot \tan\left(\frac{\pi s}{2}\right) \omega^{s-1} \tag{2.44}$$

ϵ_∞ is the dielectric constant for $\omega \to \infty$. In figure 2.16 the behaviour of the conductivity and dielectric constant for reasonable values of $\epsilon_\infty = 3$, $\sigma_{\mathrm{DC}} = 1 \cdot 10^{-7} \frac{1}{\Omega\mathrm{m}}$, $\sigma_{\mathrm{AC}} = 1 \cdot 10^{-13} \frac{1}{\Omega\mathrm{m}}$ and $s = 0.9$ is depicted.

2.3.3   External influences

Generally, when charge carriers are present in a device, at any interface an electrical double layer exists. Especially for electrochemical systems at the interface of an electrode and an electrolyte a double layer capacitance is present, which exhibits a distribution of reactivites and does not behave like an ideal capacitor [111, 112]. But also for other non-ideal-systems, deviations from the expected impedance spectra can often be found. Mostly the origin of these deviations are explained by physical properties in the system which are either not homogeneous or show a dispersion. It is common to model such effects on impedance measurements with a so called constant-phase-element (CPE) Q [112–116]. A CPE's impedance is defined by: $Z_{\mathrm{CPE}} = \frac{1}{Q(i\omega)^\alpha}$ with $0 < \alpha < 1$. The name originates from the fact that the phase angle of Q

is independent of frequency and has a constant value of -(90·α) degrees. In most models, the constant phase element has a resistor R in parallel to account for mobile charge carriers. In this case, De Levie et al. suggested an additional parameter β to account for CPE-like effects for electrodes with rough interfaces [117]. The most general form of such an impedance element can be written as:

$$Z_{R\|Q} = \frac{R}{(1 + RQ(i\omega)^\alpha)^\beta} \text{ with } 0 < \alpha, \beta < 1 \tag{2.45}$$

For $\alpha = \beta = 1$ $Z_{R\|Q}$ resembles an ideal RC-circuit and for $\alpha = \beta = 0$ an ideal resistor. The two parameters are used to account for non ideal behaviour found in impedance spectra. In this thesis, equation 2.45 was used to model the influence of the contacting layers.

Another external influence could be an inductance induced by the electrical leads of device. It can be estimated by using a formula valid for rectangular conductors with negligible height [118]:

$$L \approx \mu_0 2l \left[\ln\left(\frac{2l}{\omega}\right) - \frac{1}{2}\right] \tag{2.46}$$

The width w of the electrodes of the devices prepared in this thesis equals 4mm and the length l equals 15mm and 8mm for the cathode and anode respectively. At frequencies of 1MHz and 10MHz this estimation yields inductances of $Z_L(1\,\text{MHz}) = i\omega \cdot L \approx i0.64\,\Omega$ and $Z_L(10\,\text{MHz}) \approx i6.7\Omega$ so that the inductance could slightly influence the results for frequencies above 1MHz. Such an effect can be modelled by introducing an inductance $Z_L = i\omega L$ in series to the equivalent circuit of a device.

A last possibility for distortions of the impedance measurements could be space charges which arise from the difference in work function (the built-in voltage V_{bi}) of the electrode materials. An illustration of the energy level alignment for an organic double layer sandwiched between two electrodes at different voltages is shown in figure 2.17. Here it is assumed that there are no immobile charge carriers present in the device, which for example exist at the interface of Alq3 and NPB as reported in [119]. For the materials used in this thesis there were no hints for the presensce of such immobile charge carriers. When applying a negative bias voltage no charge carriers are injected into the device and the internal electric field is negative caused by the work function difference of the electrode materials. Therefore an equal amount of charges will be stored at the electrodes (b). The same is true for V=0 (and also small forward bias), only that the number of stored charges is decreasing (c). When V
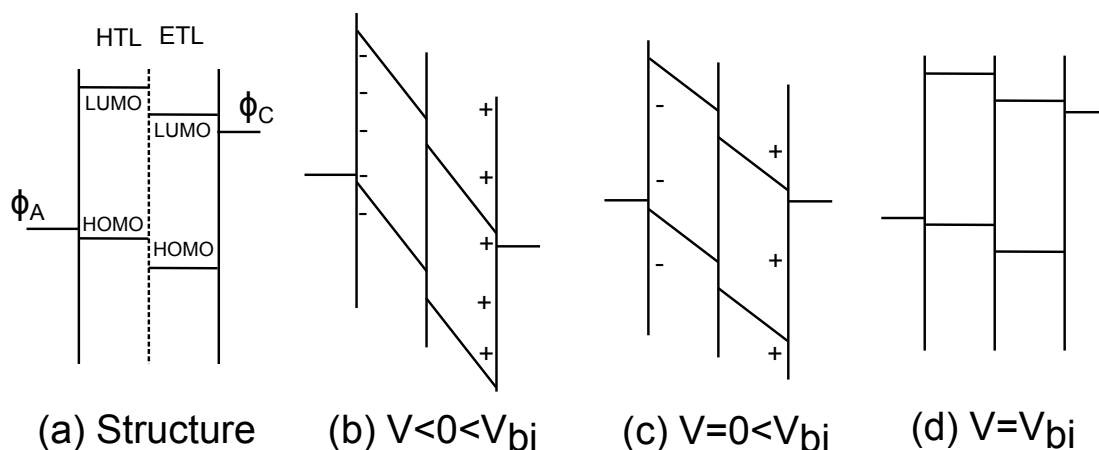
Figure 2.17: Schematic drawing of the energy alignments in an organic double layer device: (a) Position of the energy levels of the materials when they are not in contact. (b)-(d) Internal electric fields and charge distribution at the electrodes: (b) under reverse bias, the internal electric field is negative and no charges are injected into the device (c) under reverse bias V=0, equilibrium situation with $I = 0$ (d) V equals the built-in voltage V_{bi} (flat-band voltage). Adapted from [119].

equals the built-in voltage (flat-band voltage), the space charges vanish and for even higher voltages the internal electric field becomes positive and charges are injected into the device. For the measurements I chose a bias voltage of $0\,\text{V}$ and an AC signal of $50\,\text{mV}$ rms. This should ensure that no charges are injected into the device, the drift current is minimal and the amount of space charges is not too high.

2.3.4   Intermixed layers

For two organic materials, which exhibit an intermixed zone at their interface, the equivilent circuit can be divided into three layers. Layers 1 and 2 with thickness d_1 and d_2 consist of of pure material 1 and 2. Between them is an intermixed layer 12 with thickness h. The simplest approach to estimate the distribution of materials 1 and 2 in the intermixed zone is by assuming a diffusion equation. The concentration curve in such layers after time t at a concentration step from C_0=1 to C=0 at position x=0 then is defined as [120, 121]

$$C(x,t) = \frac{1}{2}\left[1 - \text{erf}\left(\frac{x}{\sqrt{4Dt}}\right)\right] \tag{2.47}$$

with diffusion constant D, time t and x the distance from the interface. The error function $\text{erf}(x) = \frac{2}{\sqrt{\pi}}\int_0^x \exp(-u^2)\mathrm{d}u$ can only be solved numerically. As described in
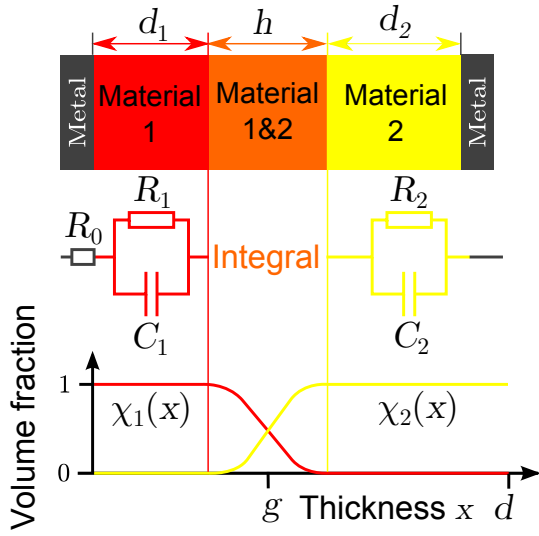
Figure 2.18: Illustration of the proposed equivalent circuit and the gradual change of the volume fraction of an intermixed double layer device. Adapted from [15].
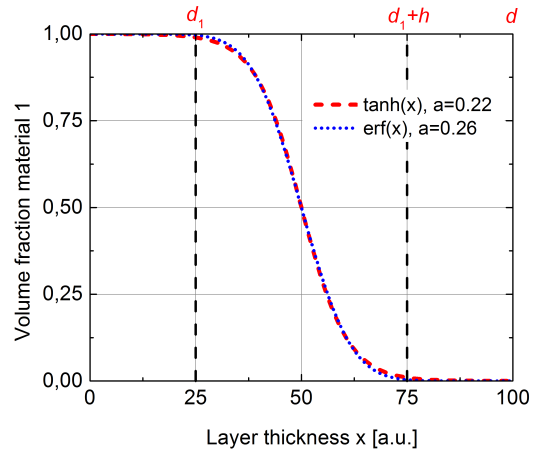

Figure 2.19: Comparison of the concentration profiles of a transition described by equation 2.49 with $a = 0.22$ and the more correct version where the tanh was replaced with the error function and $a = 0.26$ for a defined transition width $h = \frac{d}{2}$.

the previous section, the equivalent circuit of pure layers are simple RC elements. In the intermixed layer of the two materials, the fraction of each material changes gradually with position and the material parameters can also be expected to change. A simple approach for modelling the impedance of such a layer is to calculate the integral of the RC element over the layer thickness h with position dependant material parameters:

$$Z_{12} = \frac{1}{A} \int\limits_{d_1}^{d_1+h} \frac{\mathrm{d}x}{\sigma(\chi(x)) + i\omega\epsilon_0\epsilon_r(\chi(x))} \tag{2.48}$$

$\chi(x)$ is used to describe the transition of the material parameters. In [122] and [15] a tanh-function was used instead of the error function to avoid the only numerically solvable integral in $\mathrm{erf}(x)$ und thus speed up calculation:

$$\chi(x) = \frac{1}{2}\left[1 - \tanh\left(\frac{x-g}{ah}\right)\right] \tag{2.49}$$

By fixing the parameter g to $g = d_1 + \frac{h}{2}$, the function yields $\chi(d_1 + \frac{h}{2}) = \frac{1}{2}$ in the middle of the transition zone. The parameter a can be used to define the transition width h. Using the tanh-function, the dependence of the material parameters σ and

ϵ_r on position can be defined as:

$$\sigma(\chi(x), \omega) = \chi(x)\sigma_1(\omega) + (1 - \chi(x))\sigma_2(\omega) \tag{2.50}$$

and

$$\epsilon_\mathrm{r}(\chi(x), \omega) = \chi(x)\epsilon_{\mathrm{r},1}(\omega) + (1 - \chi(x))\epsilon_{\mathrm{r},2}(\omega) \tag{2.51}$$

The impedance of a device consisting of two materials with an intermixed region can be modeled as:

$$Z_\mathrm{mix,DL} = R_0 + \frac{d_1}{A}\frac{1}{\sigma_1 + i\omega\epsilon_0\epsilon_{r1}} + \frac{d_2}{A}\frac{1}{\sigma_2 + i\omega\epsilon_0\epsilon_{r2}} + \frac{1}{A}\int\limits_{d_1}^{d_1+h}\frac{\mathrm{d}x}{\sigma(\chi(x)) + i\omega\epsilon_0\epsilon_r(\chi(x))}$$

$$\tag{2.52}$$

This approach is illustrated in figure 2.19. However, dividing an intermixed double layer into three sublayer is suboptimal and also makes convergence harder to archieve. In [15] the tanh-function was used to model the impedance of the complete layer. That this can be done is illustrated in figure 2.19, where a comparison between a transition described by equation 2.49 with $a = 0.22$ and the more correct version with the error function with $a = 0.26$ for a defined transition width $h = \frac{d}{2} = 2d_1$ is shown. As can be seen, the tanh and the error function exhibit very similar curves by adjusting the parameter a. Furthermore, the value of $\chi(x)$ outside of the defined intermixed zone equals nearly 1 and can be used to describe the material parameters of the pure layers. The improved fit function by using the tanh-function for the whole layer can be written as:

$$Z_\mathrm{mix,DL} = R_0 + \frac{1}{A}\int\limits_{0}^{d}\frac{\mathrm{d}x}{\sigma(\chi(x)) + i\omega\epsilon_0\epsilon_r(\chi(x))} \tag{2.53}$$

In the intermixed layer, it can be expected that the local conductivity will change with position. This can be understood by looking at the DC part of the conductivity:

$$\sigma_{DC} = e(n_e\mu_e + n_h\mu_h) \tag{2.54}$$

It depends on both the charge carrier densities and the mobilities of holes respectively electrons. As the mobility also depends on the charge carrier density [26, 27], it can be expected that both parameters will change in an intermixed layer. In general, this can result in a change of σ in the intermixed differing from the transition described by 2.50 [123, 124]. To be able to account for these effects, an additional fit function

is introduced at this point. It is defined by adjusting equation 6.6 to:

$$Z'_{\text{mix,DL}} = Z_{\text{mix,DL}} - \int\limits_{d_1}^{d_1+h} \frac{\mathrm{d}x}{\sigma(\chi(x)) + i\omega\epsilon_0\epsilon_r(\chi(x))} + \int\limits_{d_1}^{d_1+h} \frac{\mathrm{d}x}{\sigma'(\chi(x)) + i\omega\epsilon_0\epsilon_r(\chi(x))}$$

$$\text{(2.55)}$$

with

$$\sigma'(\chi(x), \omega) = \chi(x)\sigma'_1(\omega) + (1 - \chi(x))\sigma'_2(\omega) \tag{2.56}$$

Here, the conductivities σ'_1 and σ'_2 in the intermixed regions were uncoupled from these for the pure layers and left as free parameter in the fit. In this way, the tanh-function could still be used to describe the transition of the dielectric constant, but it was possible to account for a different behaviour of the conductivity.

3. Experimental setup
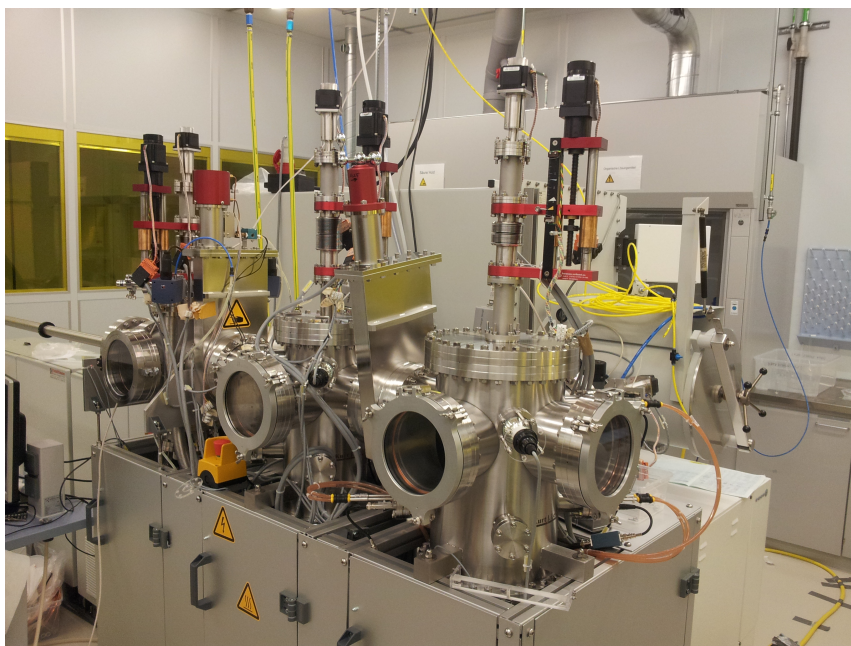
3.1 The evaporation system "Ausbildungsanlage"

Figure 3.1: Picture of the "Ausbildungsanlage" used for fabrication of the samples.

In figure 3.1 a picture of the "Ausbildungsanlage", the system used for the fabrication of all devices in this thesis, is shown. It consists of three vacuum chambers: One for the evaporation of organic small molecules, one for the evaporation of metals respectively inorganic compounds and one for transferring the samples in between the glovebox and the evaporation chambers. In figure 3.2 a schematic representation of the whole system and a picture of the glove box is shown. A vacuum of about $1 \cdot 10^{-7} - 1 \cdot 10^{-8}$ mbar is provided by two turbo molecular pumps which are connected to the metal- and organic chambers. A transfer bar is used to transport the substrate holder in between the chambers and the chambers can be isolated from each other by two gate valves.

3.1.1 Glovebox

A glovebox is a container which is hermetically sealed from the environment and contains (in this case) inert nitrogen. The pressure is kept a bit higher than on the
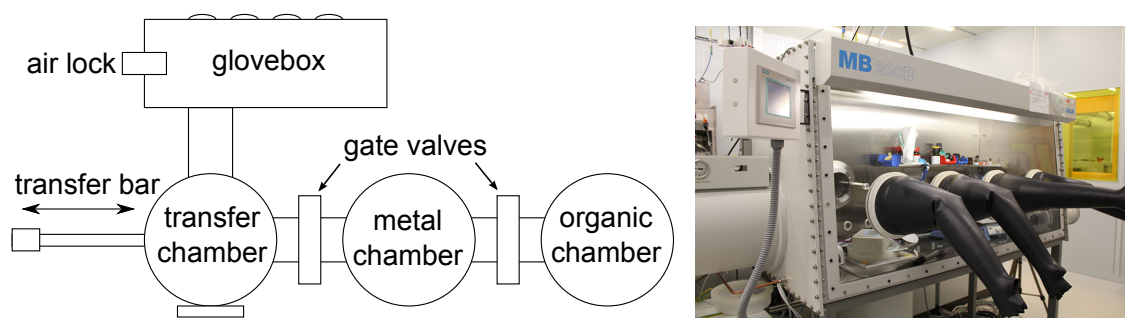
Figure 3.2: Left: Schematic drawing of the evaporation system and the connected glovebox. Right: Picture of the glovebox.

outside to avoid air penetrating the box in case of a leak. A molecular sieve and an active cole filter are cleaning the gas flow constantly providing puritiy grades of about 1ppm for O_2 and H_2O. The glovebox is directly connected to the vacuum system so that it was possible to encapsulate the samples within a high purity ambiance. This avoids chemical degradation of the materials.

3.1.2   Physical Vapor depostion

Physical vapor deposition is based on the evaporation of a heated source material and its condensation on a substrate. The high vaccuum provides a long mean free path for the evaporated particles which can travel to the substrate without colliding with too many gas particles. The better the vacuum, the more uniform the deposited film on the substrate will be. Anorganic materials are filled into a crucible, boat or filament which are heated resistively by applying a high electrical current ($\approx$ 100-200 A) at low voltages. Organic materials are filled in effusion cells made of glass and heated indirectly by a tantalum wire. The temperature in the vicinity of the cells is measured with a thermoelement. While metallic and inorganic compounds evaporate at high temperatures of about 1500 °C, for organic materials temperatures of about 100-500 °C are needed.

3.1.3   Evaporation chambers

In the organic chambers up to four materials can be evaporated at the same time (sources 1-4). The deposition rates are monitored instantaneously by four quartz micro balances (S1-S4). One is placed inside the metal chamber and three inside the organic chamber. This set-up is schematically shown in figure 3.3. To account for that the position of the quartz crystals are not placed at the maximum of the

gas stream, a proportionality factor (tooling factor) has to be determined for every material which connects the displayed layer thickness on the quartz crystals to the real layer thickness on the substrate. The substrate holder had room for a simultaneous deposition on up to nine substrates. For evaporation the substrate holder is placed in the sample holder which rotates during the deposition process to achieve a homogeneous film thickness distribution for all substrates. A shutter below the sample holder is used to define different layers and to adjust the evaporation rates.

The evaporation rates were controlled via a provided software by changing the power (voltage), which is applied to the heating units. It allowed the heating of more than one source so that co-evaporation of up to four organic materials was possible. Sadly, the system only offered a manual control of the power sources (by typesetting) rather than a PID-controlled rate adjustment. This complicated the handling of the rate control for the co-evaporation of multiple materials, especially for graded structures.
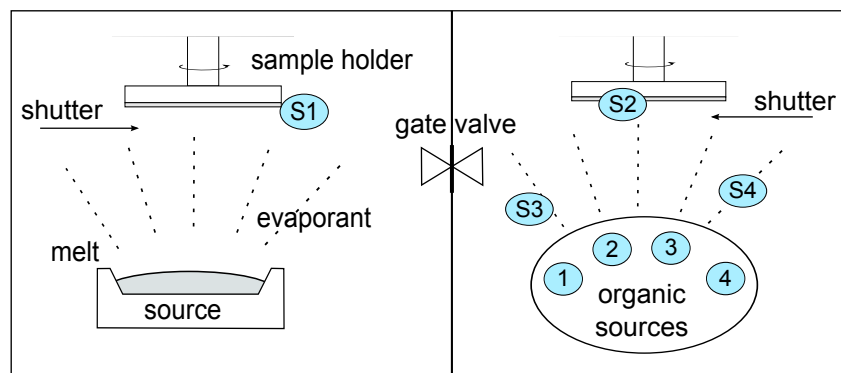
Figure 3.3: Schematic drawing of the metal- and organic chambers during an evaporation process.

3.1.4 Quartz crystal microbalances

A quarz crystal microbalance is a suitable tool to instantaneously measure the deposition rate of thin films in a vacuum and uses the fact that quartz crystals exhibits the piezoelectric effect: Mechanical stress induces an electric field in them. By applying an AC voltage to the crystals an oscillation is induced and the resonance frequency f_{res} can be found with high accuracy with a PID-control-loop which maximizes the power consumption of the crystal. When the mass of the quartz crystal is increased - e.g. by material evaporated onto it - the resonance frequency is lowered. The frequency change can be directly correlated to the mass change of the crystal and

the evaporation rate can be determined.

The precision of the microbalances is mainly limited by the amount of material already deposited on them. In general, they are very accurate down to about 85% of the initial resonance frequency. Another error is introduced by the distribution of the emission angle of the vapor. As it changes with the filling level of the materials in the crucibles, the tooling factor has to be reviewed after some time. Furthermore the tooling factors are determined by measuring the thickness of single layers of the respective material with a profilometer which itself has an error of about 5-10%. Another systematic error could be imposed by evaporating more than one material at a time. The density of a layer consisting of co-evaporated materials is possibly differerent from the averaged densities of all materials, which will slightly alter the real layer thickness. To reduce the uncertainty, the readings were double checked after evaporation of devices consisting of multiple materials by measuring the thickness of the whole stack with a profilometer. All in all, the error can be estimated to be below 15%.

3.2   Characterization methods

3.2.1   Profilometer

The layer thicknesses of the deposited films are measured with a Veeco Dektak 150 profilometer. A profilometer scans the surface of the sample with a diamond stylus with a diameter of 12,5 μm and records changes of the vertical position of the stylus. The result of the scan shows changes in height in absolute values. Owing to the use of shadow masks, the edges of the evaporated materials were quite clear, so I directly measured the height difference from the ITO to the organic or metallic layer. The layer thicknesses were measured for tooling the quartz crystals and also for double checking the sum of the displayed thicknesses after the evaporation of multiple layers.

3.2.2   BOTEST

The electrical and optical characterization and the lifetime measurements of the OLEDss were performed using a LIV BOTEST system. It is a computer controlled system which comes with a dedicated software, a source measure unit (SMU) and photodiode allowing for the simultaneous measurement of the current and luminance. The substrate holder and photodiode cover are shown in figure 3.4. Metallic pins are used to apply the voltage to the devices via the calibrated SMU. The cover shields

the devices from ambient light and the light signal of the device is transformed into an electrical signal by the photodiode (calibrated for different spectral regions) and subsequently the luminance is recorded in the software. The lifetime measurements were performed using a BOTEST system specifically designed for long time functionality testing of OLEDss. It came with a cover that shielded the different substrate pixels from each other and provided temperature control from $40\,°C$ to $90\,°C$ (not used in this thesis).
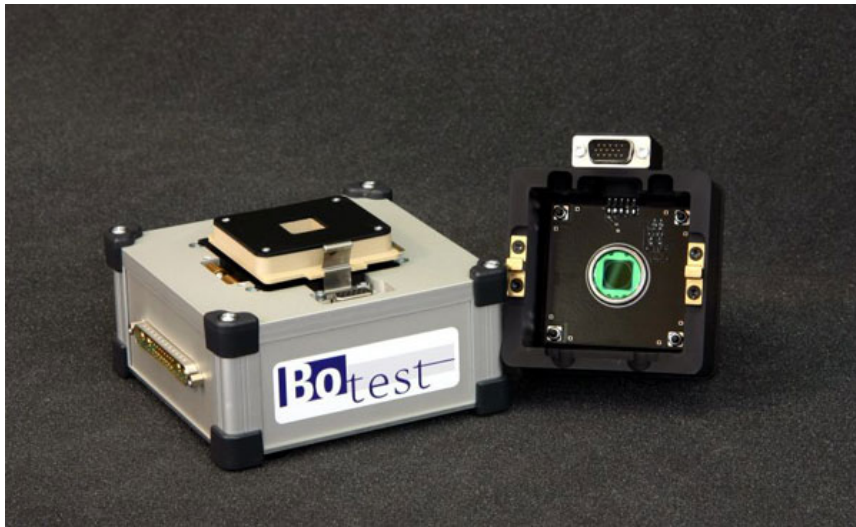

Figure 3.4: The substrate holder and photodiode cover of the LIV BOTEST system used for characterizing the OLEDs [125].

3.2.3 Impedance measurement devices

For the impedance measurements, an *Agilent 4294A* and a *Metrohm Autolab PG-STAT302N* impedance analyzer were used. The Autolab device covers a frequency range from $10\,\mu$Hz to $1\,$MHz. It was used for the measurements in the low frequency region, where a calibration is not necessary. To avoid possible hystersis effects of the conductivity, the minimum frequency used was about 1mHz. Furthermore, the measurements below that frequency became too long.

The Agilent device covers a frequency range from $40\,$Hz to $110\,$MHz, but due to phase shifts induced by the cables, the maximum frequency was limited to $20\,$MHz. All cables were shielded to reduce external influences. At high frequencies the capacitance and inductance of the cables becomes relevant, so that the Agilent device had to be user calibrated. The calibration is done by correlating the measured values of the voltage V_M and current I_M to the actual values V_D and I_D in a device by a

matrix ansatz:

$$\begin{pmatrix} V_\mathrm{M} \\ I_\mathrm{M} \end{pmatrix} = \begin{pmatrix} m_{11} & m_{12} \\ m_{21} & m_{22} \end{pmatrix} \begin{pmatrix} V_\mathrm{D} \\ I_\mathrm{D} \end{pmatrix} \tag{3.1}$$

The measured impedance Z_M can be written as:

$$Z_\mathrm{M} = \frac{V_\mathrm{M}}{I_\mathrm{M}} = \frac{m_{11}V_\mathrm{D} + m_{12}I_\mathrm{D}}{m_{21}V_\mathrm{D} + m_{22}I_\mathrm{D}} = \frac{m_{11}Z_\mathrm{D} + m_{12}}{m_{21}Z_\mathrm{D} + m22} \tag{3.2}$$

with the devices impedance $Z_\mathrm{D} = \frac{V_\mathrm{D}}{I_\mathrm{D}}$. Now, firstly a measurement without any sample was performed ($I_\mathrm{D} = 0$), which yields the open circuit impedance:

$$Z_\mathrm{O} = \frac{m_{11}}{m_{21}} \tag{3.3}$$

Directly connecting the needles to each other ($V_\mathrm{D} = 0$) yields the short circuit impedance:

$$Z_\mathrm{S} = \frac{m_{12}}{m_{22}} \tag{3.4}$$

Equations 3.3 and 3.4 result in:

$$Z_\mathrm{M} = \frac{m_{11}Z_\mathrm{D} + m_{22}Z_\mathrm{S}}{m_{11}Z_\mathrm{D} + m_{22}Z_\mathrm{O}} Z_\mathrm{O} \tag{3.5}$$

Now measuring the impedance Z_KD of a device with known impedance Z_K one obtains:

$$m_{22} = \frac{Z_\mathrm{K}Z_\mathrm{KD} - Z_\mathrm{K}Z_\mathrm{O}}{Z_\mathrm{O}Z_\mathrm{S} - Z_\mathrm{KD}Z_\mathrm{O}} m_{11} \tag{3.6}$$

With this, the correlation between a measured and real impedance can be calculated:

$$Z_\mathrm{D} = \frac{(Z_\mathrm{S} - Z_\mathrm{M})(Z_\mathrm{KD} - Z_\mathrm{O})}{(Z_\mathrm{M} - Z_\mathrm{O})(Z_\mathrm{S} - Z_\mathrm{KD})} Z_\mathrm{K} \tag{3.7}$$

For calibration, a 1kΩ resistor for Z_K was used. Its precise resistance was determined with the Autolab device directly before every calibration. The reason to do this was to guarantee that both the measurements of both devices were comparable.

An examination of the limits of both devices and an estimation of the statistical error was already carried out in [126] and is not specified here again. The Autolab yields reliable results up to a frequency of about 1kHz, where the inductance of the device distorts the measurements. The Agilent produces good results for frequencies between 100 Hz and 6 MHz, which is nearly its whole frequency range. I decided to use both devices for the same frequency ranges as in [126]: the Agilent for frequencies above 200 Hz and the Autolab for frequencies below 500 Hz. The overlap was used

to identifiy variations between both measurements, e.g. caused by bad contacts. If the measurements showed a strong deviation in this region, they were repeated or left out of the analysis, but this occured only for few devices.

4. Materials and sample preparation

In section 4.1 the semiconducting properties of the materials used for the OLEDs are described in detail. In section 4.2 the steps of preparation of the OLEDs are described and in section 4.3 the structures of the different OLED-stacks, which are analyzed in chapter 5, are introduced.

4.1 Material set

In this section an overview of the materials used in this thesis is given. The active organic materials are small molecules based on aromatic hydrocarbons. Their structural formulas, triplet energies and molecular weights are shown in figure 4.1 (a).

ITO-substrates

The ITO-substrates came on glass substrates with an area of $20\,\mathrm{cm}^2 \times 20\,\mathrm{cm}^2$ and a sheet resistance of $10\,\Omega/\mathrm{square}$. They were structured at the InnovationLab using a self developed lithographie-process and afterwards cutted into substrates with an area of $25\,\mathrm{mm}^2 \times 25\,\mathrm{mm}^2$. The structured ITO substrates are shown in figure 4.2 (a).

Molybdenum trioxide (MoO_3)

Molybdenum trioxide was used as a hole injection layer (HIL). It is a strongly n-type material and exhibits a very high work function of $\Phi \approx 6.7\,\mathrm{eV}$. For a long time it was controversely discussed why it works as an efficient hole-injection layer for organic materials. Kröger et al. showed that electrons from the HOMO of the organic material are injected into the conduction band of MoO_3 [127]. This corresponds to an injection of holes into the organic material and is illustrated in figure 4.1 (b). The conductivity of MoO3 is 2-3 orders of magnitude higher than that of organic materials.

4,4,4-Tris(N-carbazolyl)triphenylamine (TCTA)

TCTA is based on a triphenylamin-centrum. It shows good electrical conductivity and electroluminescence and is mostly used as an HTL. It exhibits an relatively large energy gap between the HOMO at 5.5 eV-5.8 eV and the LUMO at 2 eV-2.4 eV
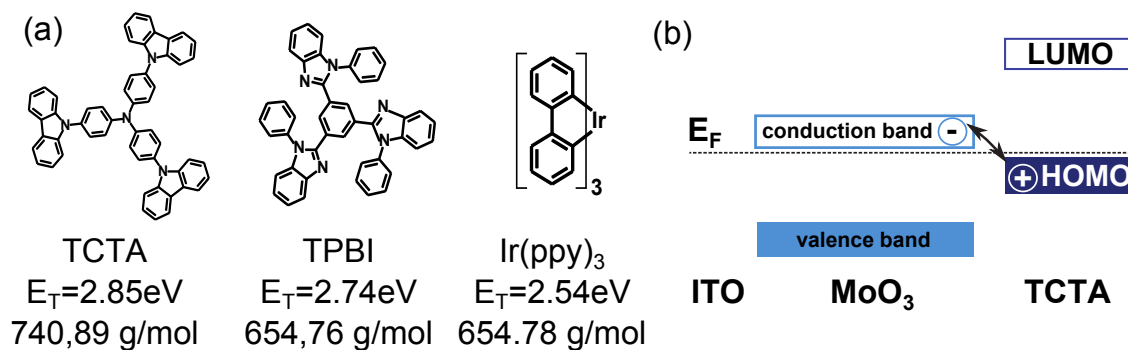
Figure 4.1: (a) Structural formulas, molecular weights and corresponding triplet energies of the organic materials. (b) Hole injection mechanism at the anode: Electrons are transferred from the HOMO of TCTA into the conduction band of MoO_3 [127]. Adapted from [136].

[8, 128–130]. The hole conductivity of TCTA is about $10^{-4} - 10^{-5} \frac{cm^2}{V\,s}$, whereas the electron conductivity cannot be measured by time-of-flight methods [131, 132]. Because of its low LUMO and low electron mobility TCTA is also often used as an electron blocking layer.

1,3,5-Tris(phenyl-2-benzimidazole)benzene (TPBI)

TPBI shows a large energy gap with the HOMO at about $6.3\,eV$ and the LUMO at about $2.7\,eV$. It is used as electron transport layer (ETL) and exciton blocking layer. The electron mobility of TPBI is of the order $10^{-5} \frac{cm^2}{V\,s}$ [133].

fac-Tris(2-phenylpyridin)iridium (Ir(ppy)$_3$)

Ir(ppy)$_3$ is a phosphorescent emitter complex with a relatively short triplet lifetime of about $2\,\mu s$ and a quantum effiency yield of nearly 100 % [134]. The central heavy Ir-atom leads to a high probability for ISC as described in chapter 2.2 caused by spin-orbital-interaction. The maximum of the emission spectrum lies at $513\,nm$ in the green spectral region, corresponding to a triplet energy of about $2.52\,eV$, which is lower than that of TPBI and TCTA. The LUMO level is at about $5.5\,eV$ whereas the reported values for the LUMO-level range from $2.2\,eV$-$3\,eV$ [8, 134]. To avoid agglomeration of Iridium and resulting quenching effects, the doping concentrations should be below 10 % [135]. At the same time for efficient short-range Dexter transfer it should not be too low. Concentrations of about 6 %-8 % have shown to yield very efficient devices so that a doping concentration of 7 % was chosen for all devices prepared in this thesis.
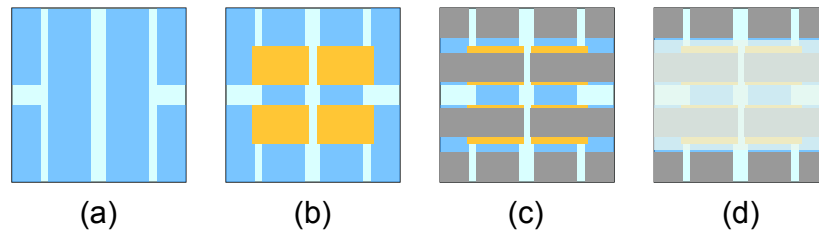
Figure 4.2: Illustration of the substrates during device fabrication: (a) Glass substrate (25mm x 25mm area, 0.7mm thick) with pre-structured 150nm thick ITO layer. (b) Device after the deposition of the hole-injection and organic layers. (c) Device after the deposition of the cathode. The active area of each of the four pixels is 6mm x 4mm. (d) Encapsulated device.

4.2 Preparation

In figure 4.2 the different steps of device fabrication are illustrated.The pre-structured ITO substrates were cleaned in acetone and isoproanol for 10 min in an ultrasonic bath and subsequently dried with highly purified nitrogen. After that they were treated with UV ozone for 10 min. The ozone treatment reduces the roughness of the ITO and increases the surface energy resulting in an increased work function. The reason for this is still controversially discussed and may be due to surface carbon removal, creation of surface dipoles or a change in the ratio of surface molecules [137]. In general it leads to a better electronic contact between the ITO and organic layers and improves charge injection and thus efficiency.

Directly after the ozone treatment the substrates were introduced into the glovebox. For deposition of MoO_3 and the organic layers a shadow mask was used which allowed covering of the two central ITO stripes at four positions. After the deposition of the organic layers, the shadow mask was changed inside the glovebox and the cathode was deposited yielding four pixels with an active area of $24\,mm^2$. Finally, the devices were transferred to the glovebox and immediately encapsulated with an adhesive foil from the supplier 3M to minimize device degradation. All devices were stored in the glovebox for a maximum of two days before the measurements were carried out.

4.3 OLED-stacks

The structures of the OLED stack which are compared in this thesis are summarized in table 4.1. One aim of this thesis is to examine the influence of the composition
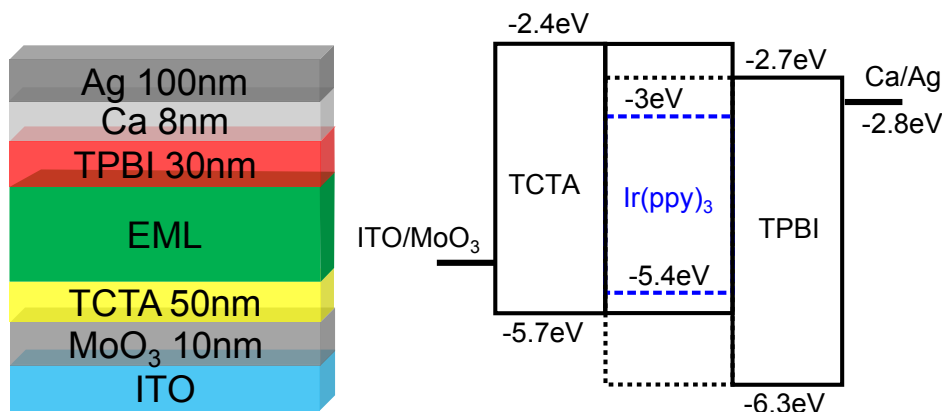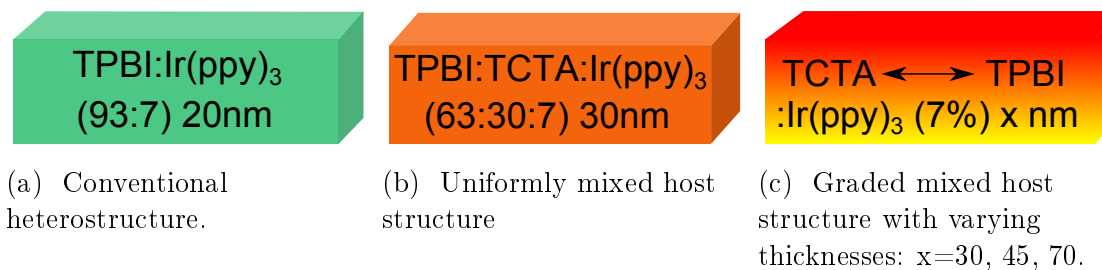
Figure 4.3: Top: The general structure of the stack used for the different OLEDs and the proposed energy level diagram of the organic materials. Bottom: The different compositions of the EML.

(a) Conventional heterostructure.

(b) Uniformly mixed host structure

(c) Graded mixed host structure with varying thicknesses: x=30, 45, 70.

of the light emitting layer (EML) on the performance and characteristics of OLEDs. For that purpose, apart from the EML, all OLED-layers were kept the same for all devices. The OLED-stack is depicted in figure 4.3 and is composed of a 10nm thick layer of MoO_3 as HIL, a 50nm thick TCTA layer as HTL, a 30nm thick TPBI layer as ETL. The anode and cathode layers are 150 nm ITO and 10 nm/100 nm Ca/Ag respectively. As a test device an OLED-stack developed at TU-Braunschweig was used [138]. It consists of a conventional heterostructure (HS) (figure 4.4a) and

Table 4.1: Device structures for comparison of heterostructure and mixed host EML devices. The numbers are thicknesses in nm. All stacks are sandwiched between ITO (150nm) and Ag (100nm). The $Ir(ppy)_3$ concentration is 7% for all devices.

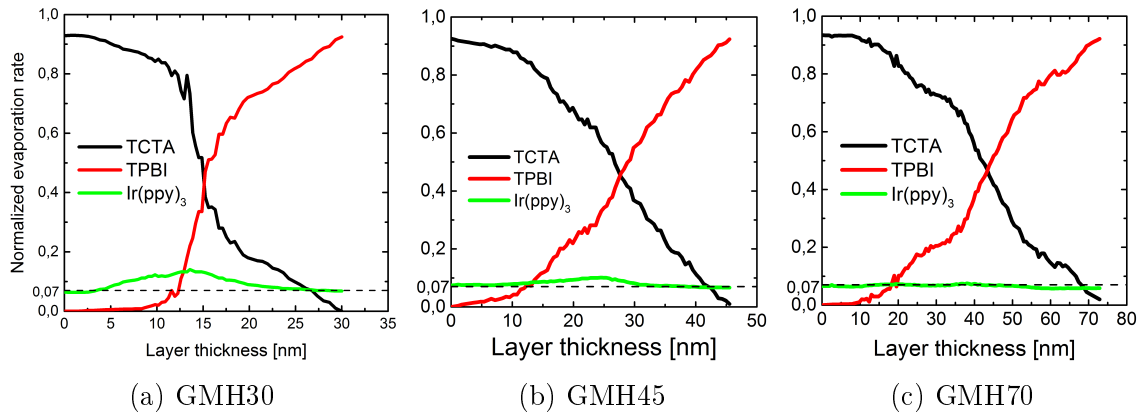| Stack	MoO_3 (HIL)	TCTA (HTL)	Host+7% $Ir(ppy)_3$	TPBI (ETL)	Ca
HS	10	50	TPBI, 20	30	10
UMH	10	50	TPBI+TCTA (63:30), 30	30	10
GMH30	10	50	TCTA↔TPBI, 30	30	10
GMH45	10	50	TCTA↔TPBI, 45	30	10
GMH70	10	50	TCTA↔TPBI, 70	30	10

Figure 4.5: Normalized evaporation rates over the position inside the light emitting layer for the three different OLEDs with a graded mixed host. As a guide for the eye, the dotted line equals a doping concentration of 7%.

the phosphorescent dye $Ir(ppy)_3$ is doped into 20 nm of the ETL material TPBI. This OLED structure shows a good charge balance caused by the outstanding hole injection properties of MoO_3 and current and power efficiencies of $44 \frac{cd}{A}$ respectively $40 \frac{lm}{W}$ with a relatively low roll-off behaviour were reported [127, 138].

OLEDs with four different mixed host structures are presented for comparison with the HS stack: Firstly, one uniformly mixed host structure (UMH) with a mixing ratio of 64:30:6 (TPBI:TCTA:$Ir(ppy)_3$) was prepared (figure 4.4b). This mixing ratio was reported to yield a good charge balance in similar devices incorporating these molecules [8, 78].

Secondly, three OLEDs with graded mixed host structures in the EML and thicknesses of 30 nm, 45 nm and 70 nm were prepared (figure 4.4c). The normalized evaporation rates of the three OLED structures are shown in figure 4.5 (a)-(c). The rates of TCTA, TPBI and $Ir(ppy)_3$ are shown in black, red and green color respectively. As can be seen, the GMH30 stack shows an increased doping concentration in the middle of the EML, because it was difficult to keep the total evaporation rate constant throughout the whole layer. For the GMH45 stack there is only a slight increase of the doping concentration and for the GMH70 stack it is nearly constant. Possible influences on the device performance caused by this effect are discussed in chapter 5.

5. Characterization of the OLEDs

In this chapter the OLED stacks introduced in section 4.3 are characterized and their performances compared to each other. A detailed discussion of the LIV-characteristics, spectra, efficiency, and lifetime of the OLEDs is presented.

5.1 LIV characteristics and efficiency

LIV characteristics

In figure 5.1 the Luminance-Current-Voltage (LIV) characteristics of all OLEDs with a conventinal heterostructure (HS) are shown. The I-V-behaviour can be divided into three sub-regions with different slopes and can be described by $I \propto V^{m+1}$: For low voltages, $V < 2.5$V, an ohmic behaviour in the conductivity with m=0 can be observed. At higher voltages, $2.5\,\mathrm{V}< V <5.5\,\mathrm{V}$, the slope can be described with $m \approx 8 - 11$ (dashed-dotted-line). For even higher voltages, $V >5.5\,\mathrm{V}$, the slope changes to lower values with $I \propto V^{5.2}$ (dotted line). The observed current follows a behaviour typical for trap-charge-limited-currents (TCLC) described in section 2.1.2. With increasing voltage, the traps are filled and the slope decreases. Taking a field dependant mobility (compare equation 2.1) into account, the slope at very high voltages can also be described by a space-charge-limited-current with $I \propto V^2 e^{a\sqrt{V}}$ and $a = 2.6$.

The turn-on voltage of all devices equaled about $2.7\,\mathrm{V}$. It is worth noting that this voltage is nearly equal to the minimum energy required for creating a triplet exciton on the dopant (E_T=2,54eV). The turn-on voltage can thus possibly not be be decreased much further for this OLED-structure.
In this section, the LIV characteristics and the efficiency of the different OLED stacks are analyzed. As an introduction, in 5.1 the properties of the stack with the conventional heterostructure (HS) are discussed. Subsequently, the averaged data of all OLED stacks are compared to each other and reasons for the different characteristics are implicated.

In figure 5.2 the averaged current efficiency and power efficacy of all 10 HS devices is plotted over the luminance. The maximum current efficiency is reached at about $100\,\frac{\mathrm{cd}}{\mathrm{m}^2}$, below this brightness the values were more widely scattered. At $200\frac{\mathrm{cd}}{\mathrm{m}^2}$, the analysis yields a maximum efficiency of $\eta_I = 36.1\,\frac{\mathrm{cd}}{\mathrm{A}}$ respectively $\eta_P = 29.1\,\frac{\mathrm{lm}}{\mathrm{W}}$ and
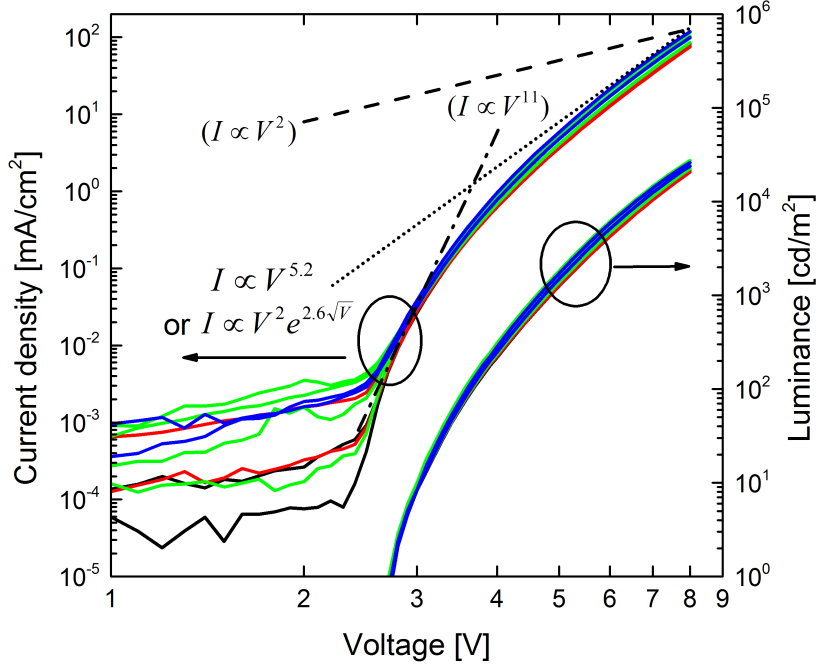
Figure 5.1: LIV characteristics of all devices with a conventional heterostructure.

averaged efficiencies of $\eta_I = (33.9 \pm 1.5)\,\frac{\text{cd}}{\text{A}}$ respectively $\eta_P = (27.2 \pm 0.7)\,\frac{\text{lm}}{\text{W}}$. We can compare the efficiencies with these reported for a similar stack [138], $\eta_I = 43\,\frac{\text{cd}}{\text{A}}$ and $\eta_P = 34\,\frac{\text{lm}}{\text{W}}$. The differences can possibly be explained by the fact that in this publication WO_3 and LiF/Al were used as hole- respectiveley electron injection layers. These might have slightly better injection properties compared to MoO_3 and Ca/Ag. Yet, the general characteristics, especially in terms of efficiency roll-off at higher luminance levels, are comparable.

Now, the performance of the OLEDs with a heterostructure (HS), an uniformly mixed host structure (UMH) and a graded mixed host structure (GMH) in the EML will be analyzed and compared to each other. The structures of the OLED-stacks presented here are described in section 4.3. In figure 5.3 the averaged LIV characteristics of all OLED-stacks are shown. The given data points are averaged values of 10-13 devices for each stack. For all stacks, the current behaviour exhibits three regions: Ohmic conductivity for low voltages, TCLC behaviour for higher voltages and a transition to SCLC at very high voltages. For all stacks it was possible to desribe the slope for high voltages by either a TCLC dependance of the current density with $I \propto V^m$ ($m \approx$ 4-7, depending on the stack) or by a SCLC behaviour taking a field dependant mobility into account with $I \propto V^2 e^{a\sqrt{V}}$ and $1 < a < 3$ (depending on the stack). This analysis is just a rough estimation and does not take recombination
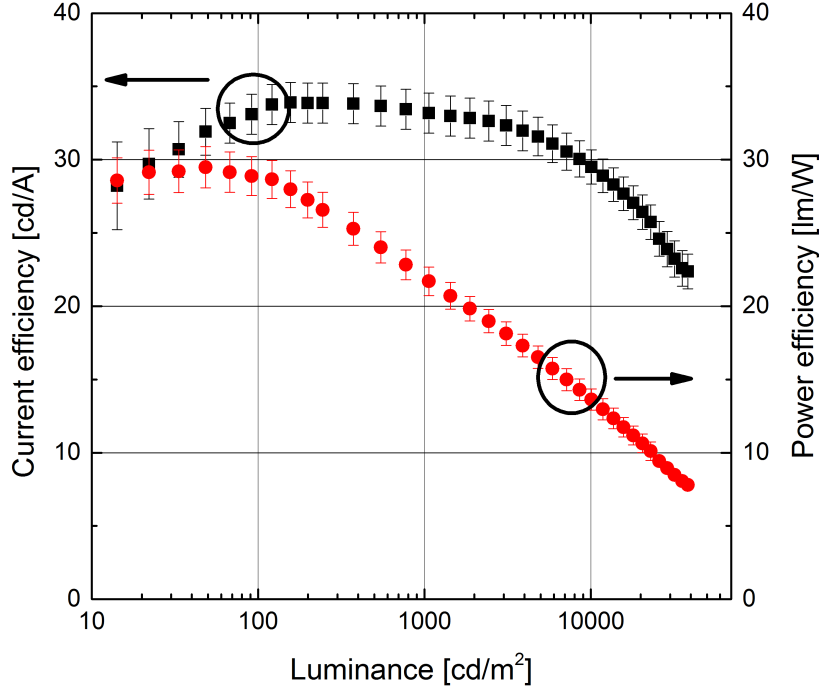
Figure 5.2: Averaged current efficiency and power efficacy off all devices with a conventional heterostructure.

effects into account. To find out if TCLC or SCLC is the dominant charge transport mechanism at high bias, measurements at different temperatures and layer thicknesses would be required to check the IV-dependance on these parameters, which was beyond the scope of this thesis.

The turn-on-voltage for all devices is around V_T=2.7 V and does not seem to be influenced by the layer thickness and/or mixed structures in the emitting layer. Thus, the injection properties for all stacks seem to be limited by the injecting and transporting layers which are the same for all devices. Variations of the characteristics at higher bias voltages can be exclusively attributed to the different structures in the EML and the layer thickness.

The effect of increasing layer thickness expresses itself in the reduction of current density and luminance (compare figure 5.3). For voltages slightly above the turn-on voltage the influence of the layer thickness is low and the current density is similar for all stacks. With increasing voltage, the slope of the current density is expected to be lower for the stacks with a thicker organic layer. However, the GMH30 compared to the HS as well as the GMH45 compared to the UMH exhibit nearly the same slopes, although the layer thickness for the graded devices is about 10 nm higher in
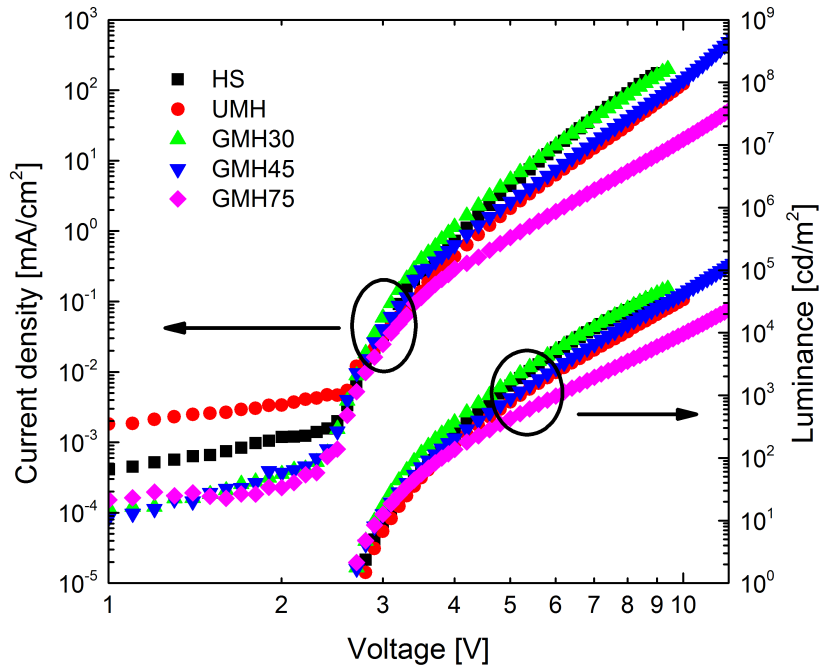
Figure 5.3: Averaged LIV characteristics of all OLED-stacks.

both cases. It can be assumed that the graded structure of the GMH stacks leads to a reduced voltage drop in the EML. This effect can be attributed to the fact that there are no accumulation of charge carriers at one of the interfaces in contrast to the abrupt interface of the HS. The UMH seemingly does not show an improved current density compared to the HS stack. That can possibly be attributed to the fact that the mixing ratio of the matrix molecules is not optimized resulting in an unbalanced charge transport inside the EML.

Efficiency and roll-off characteristics

In figure 5.4 the averaged current efficiency and power efficacy as a function of luminance of all stacks are depicted. As can be seen, the GMH70 outperforms all other stacks. At 200 $\frac{cd}{m^2}$ the stack reaches maximum efficiencies of 57.5 $\frac{cd}{A}$ and 42.6 $\frac{lm}{W}$, which are excellent values considering that it consists of only three organic layers.

Just like the GMH70, also the GMH45 and the UMH exhibit a slightly higher current efficiency compared to the HS, whereas the GMH30 shows a similar maximum current efficiency compared to the HS. For the GMH30 this could be attributed to the fact that the graded layer is not thick enough to profit from the effects of a broadened emission zone. Also the higher doping level in the middle of the EML as
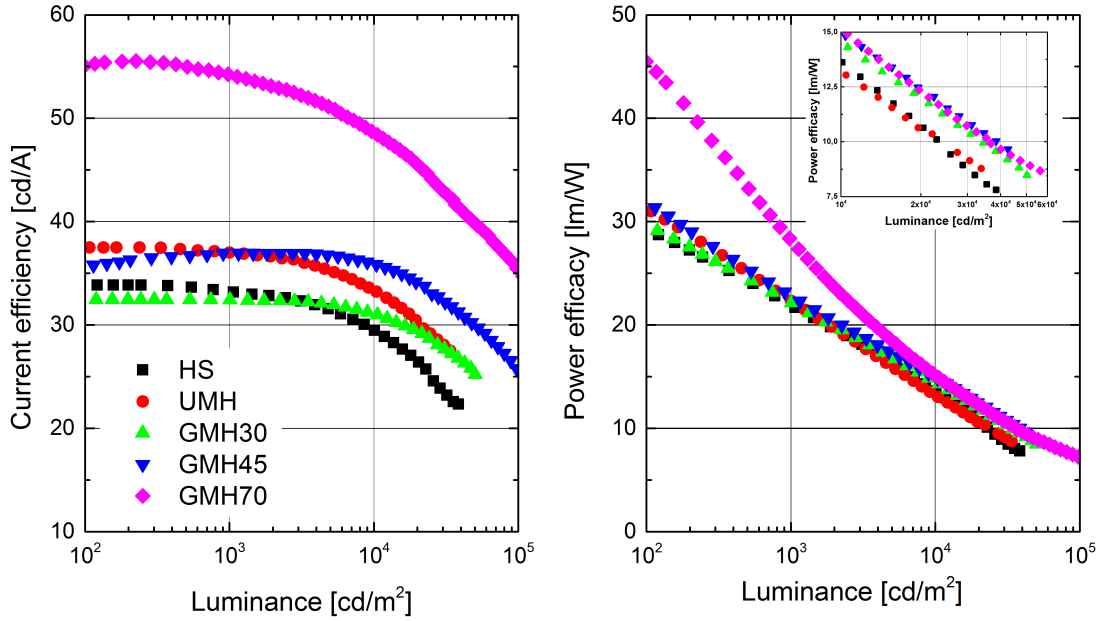
Figure 5.4: Averaged current efficiency (left) and luminous efficacy (right) of all stacks plotted over the luminance. The inset shows the power efficacy at high luminance levels.

described in 4.3 could be a reason that it does not show an increased efficiency. All stacks apart from the GMH45 reach their maximum current efficiency at luminances of 100-500 $\frac{cd}{m^2}$, whereas the efficiency of the GMH45 slightly increases till even $3\frac{kcd}{m^2}$. At this point, for the HS, UMH and GMH70 a decline in efficiency can already be observed. This effect could be attributed to a shift of the recombination zone to a distance from the cathode which result in slightly better microcavity effect.

Apart from the GMH70, the power efficacy is very similar for all stacks. Due to its increased driving voltage, at higher brightnesses the power efficacy of the GMH70 becomes comparable to the other stacks. Yet, at luminance levels above $10\frac{kcd}{m^2}$ (see inset of 5.4) all of the GMH stacks exhibit the same efficacy which is slightly better than that of the UMH and HS stacks. One reason for the higher efficiencies not related to an optimized structure of the EML, can be that the location of the recombination zone is placed in a distance relative to the cathode resulting in optimized microcavity effects (as already proposed for the GMH45). For a similar OLED stack, simulations found an optimized distance to an LiF/Al cathode of about 60 nm. However, the simulation also accounts for a certain ITO and HTL thickness and the reflectivity of Ca/Ag is slightly different from that of LiF/Al. The distance of the ETL/EML interface relative to the cathode in the HS of 50nm is possibly near
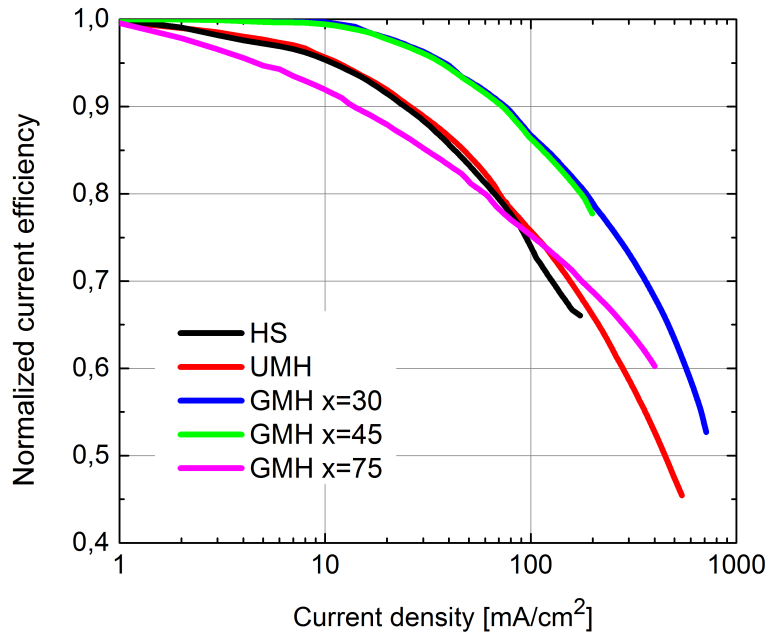
Figure 5.5: Normalized current efficiency as a function of current density of all stacks.

the optimum. For the GMH70, the distance of the recombination zone relative to the cathode can range from 30 nm to 100 nm. As already mentioned, TCTA exhibits a slightly better hole conductivity than TPBI, leading to the assumption that the recombination zone is closer to the EML/TPBI interface. But even if this effect in general can account for an increase in efficiency, it is not expected to be the main factor for the the strong enhancement in efficiency observed for the GMH70.

It is clearly visible that in terms of current efficiency roll-off the GMH stacks are outperforming the UMH and HS. To study this in more detail, in figure 5.5 the normalized current efficiencies as a function of current density of all stacks are depicted. In a recent publication [3], the critical current density $J_{90\%}$ was introduced as the current density for which the efficiency drops to 90 % of its initial value. As can be seen, $J_{90\%}$ is lowest for the GMH70 and equals $14\,\frac{\mathrm{mA}}{\mathrm{cm}^2}$. The HS and UMH exhibit nearly the same roll-off characteristics with $J_{90\%} = 25\,\frac{\mathrm{mA}}{\mathrm{cm}^2}$. The GMH30 and the GMH45 show a similar roll-off with $J_{90\%} = 77\,\frac{\mathrm{mA}}{\mathrm{cm}^2}$. Simulations directly attributed an increase of $J_{90\%}$ to an increase of the width of the recombination zone by approximately the same factor [3]. This leads to the assumption, that the recombination zone width w in the GMH30 and GMH45 is about 3 times broader compared to the HS and UMH. Assuming a narrow recombination zone $w \approx 10$ nm for the HS [64], this results in $w \approx 30$ nm for the graded devices. The GMH70 shows a flatter roll-off compared to the other stacks so that it even shows a smaller

roll-off above 100 $\frac{mA}{cm^2}$ compared to the HS and UMH. In literature, such a behaviour was recently attributed to changes in charge balance with increasing current density [98, 139], but simulations which took into account a change of the width of the recombination zone with increasing current density, $w(J)$, also can explain this effect [3].

A summary of the averaged and maximum power efficacies and the corresponding driving voltages at luminances of 200 $\frac{cd}{m^2}$ respectively 10 $\frac{kcd}{m^2}$ of all stacks are included in table 5.3. In conclusion it has been shown that graded mixed host structures in the light emitting layer can greatly enhance the efficiency of OLED devices. Furthermore, the efficiency roll-off at high current densities is strongly reduced. Both can be attributed to a better charge balance and a broadened recombination zone inside the EML.

5.2   Spectra and quantum efficiency

In figure 5.6 the normalized emission spectra of all stacks at a current density of 20 $\frac{mA}{cm^2}$ are shown. For comparison, the emission spectrum of a TCTA/TPBI heterostructure device without doping is also depicted. The doped stacks all exhibit typical green Ir(ppy)$_3$ emission with the peak at around 513 nm and no fluorescent emission from TCTA or TPBI can be identified in the spectra. This is true also for higher current densities and it can be concluded that all excitons are efficiently confined to the EML for all OLED-stacks and the exciton energy transfer from the host to the dopant is complete. This can be attributed to the good electron-, hole- and exciton blocking characteristics of TCTA and TPBI, which confine the excitons efficiently inside the EML. However, as can be seen in the inset, the shoulder of the spectrum at about 540nm is slightly differing. In general in literature, different reasons for variations of the emission spectrum of OLEDs with a phosphorescent dye were reported:

- It was reported that the emission spectrum and photophysical properties of heavy transition metal complexes can be influenced by the composition of its host matrix [140]. The host matrix of the HS consists of 100 % TPBI, that of the UMH has a fixed TCTA:TPBI ratio (63:30), while the composition of the host matrix is varying with position for the GMH stacks.

- Microcavity effects, which are dependant on the position of the recombination zone relative to the cathode inside the OLED-stack, can alter the spectrum as reported in [141].

- Variations of the doping concentration of the different stacks can lead to changes in the spectrum: With increasing doping concentration, the emission peak of the Ir(ppy)$_3$ spectrum becomes red shifted and the full width at half maximum increases [53]. As three materials were evaporated at the same time for the UMH and GMH stacks, the doping concentration possibly varies slightly between the different stacks. Also a position dependant variation of the doping concentration in the EML, like it is present for the GMH30 and GMH45 devices (see section 4.3), could have effects on the spectrum.

The spectrum of the UMH differs strongest compared to the other stacks. In contrast to the other stacks, TCTA molecules are present over the whole span of the uniformly mixed EML and possibly explain the variations. Additionally, a slightly higher doping concentration could be the reason for the deviation. The latter as-
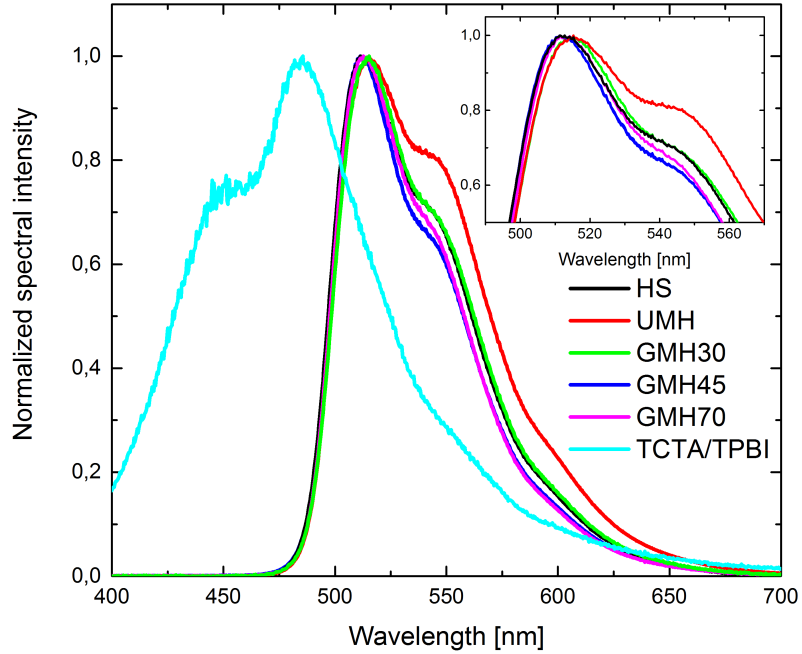
Figure 5.6: Normalized emission spectra off all stacks at 20 $\frac{mA}{cm^2}$. The inset is a zoom into the region with high intensity.

sumption is supported by the fact that also the emission peak of the UMH device is slightly red shifted and the spectrum is broader [53].

The emission spectra of the GMH stacks, which also include TCTA in the EML, are similar to that of the HS. If we assume that the presence of TCTA in the host matrix influences the spectrum, this leads to the presumption that the recombination zone is positioned at the vicinity of the EML/ETL interface, where the TPBI concentration is higher. This also corresponds to the fact that the hole mobility of TCTA is about one order of magnitude higher than the electron mobility of TPBI.

In this respect, it is interesting to look at the change of the emission spectrum of the GMH stacks with current density. This is shown in figure 5.7, using a GMH70 device as an example. The shoulder of the spectrum slightly shifts with increasing current density and the spectrum broadens. The reason for that is most probably a shifting position of the recombination zone, which on the hand results in a change of

Table 5.1: The values of the paramater K calculated with equation 5.1

	HS	UMH	GMH30	GMH45	GMH70
K [nm]	742.6	743.2	741.7	752	743.4

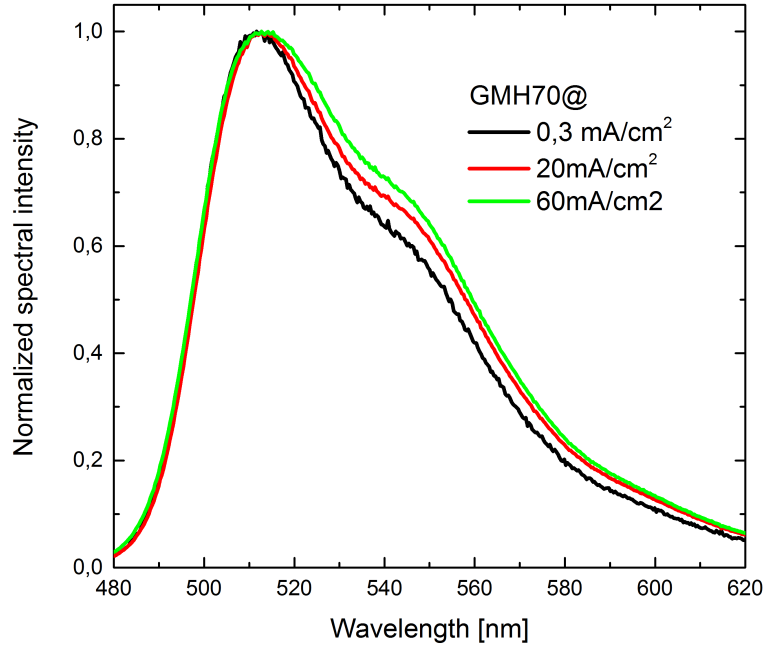Figure 5.7: Normalized emission spectra of a GMH70 device at current densities of $0.3 \frac{mA}{cm^2}$, $20 \frac{mA}{cm^2}$ and $60 \frac{mA}{cm^2}$.

microcavity effects and on the other hand in a steady change of the concentration of TCTA in the host matrix. This effect was most pronounced for the GMH stacks. The spectrum for the HS, for which the recombination zone is expected to be confined to a thin region at the EML/TCTA interface, stayed constant for all current densities. The spectrum of the UMH shifted slightly with increasing current density, but not so strong as that of the GMH stacks and this is probably also caused by minor shifts of the recombination zone.

The changes in the spectra with increasing current density are a strong hint for a shift of the recombination zone. This would also implifcate that the recombination zone is not confined to the vicinity of one of the interfaces and thus most probably also broader than in the HS.

Assuming the OLEDs to be lambertian radiators, the external quantum efficiency (EQE) can be estimated with equation 2.18 by measuring the LIV curves and the emission spectra of the devices [60]. The integrals in equation 2.18 for determining the EQE were calculated for all stacks. I defined as parameter K with the unit nm:

$$K = \frac{\int_{380\,nm}^{780\,nm} I\left(\lambda\right) \cdot \lambda \mathrm{d}\lambda}{\int_{380\,nm}^{780\,nm} I\left(\lambda\right) \cdot V\left(\lambda\right) \mathrm{d}\lambda}. \tag{5.1}$$
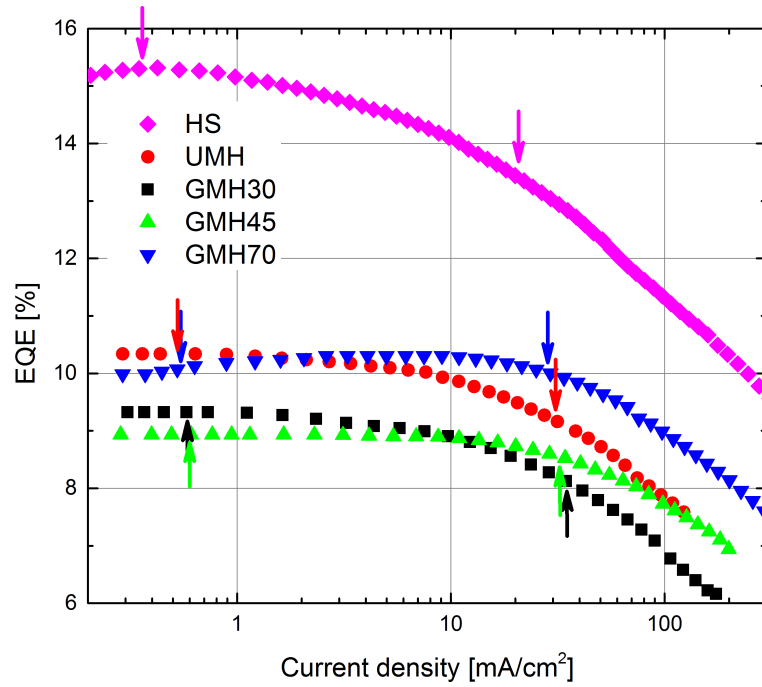
Figure 5.8: External quantum efficiency plotted over the current efficiency as calculated with equation 2.18. The current densities which correspond to $200 \frac{cd}{m^2}$ respectively $10 \frac{kcd}{m^2}$ are highlighted with arrows.

The values of K at a current density of $20 \frac{mA}{cm^2}$ for all stacks are presented in table 5.1 and differ only slightly. Additionally, the shift in the spectra of the UMH and GMH stacks with increasing current density as illustrated in figure 5.7 resulted in a change of K of only about 0.5 % and was ignored. Thus, the values of K can be used to calculate the EQE at all current densities.

In figure 5.8 the estimated external quantum efficiencies of all stacks are plotted over the current density. The arrows are highlighting the current densities corresponding to luminances of $100 \frac{cd}{m^2}$ respectively $10 \frac{kcd}{m^2}$. The GMH70 shows an outstanding EQE of 15.5 % at $100 \frac{cd}{m^2}$, while at a current density of $200 \frac{mA}{cm^2}$ the EQE is still above 11 % and higher than the maximum EQE of any other stack. As we have seen, the spectra of all stacks are only slightly varying with current density. In that case, the current efficiency and the EQE are directly proportional to each other. For that reason the roll-off behaviour of the EQE is equivalent to that of the current efficiency and does not have to be analyzed again.

As described in chapter 2.2, the out-coupling efficiency χ_{out} of a normal glass substrate is about 0.2. Using

$$\eta_{\text{ext}} = \chi_{\text{out}} \cdot \eta_{\text{int}}, \tag{5.2}$$

one can estimate the intrinsic quantum efficiency. At $100 \, \frac{\text{cd}}{\text{m}^2}$ the GMH70 shows an average intrinsic quantum efficiency of $\eta_{\text{int}} \approx 0.78$. Considering that the stack consists of only three different layers with two transporting materials, this is an excellent value. OLEDs incorporating Ir(ppy)_3 with an internal quantum efficiency of nearly 100 % have been reported [8, 53, 142], but they mostly consist of additional charge transporting and/or exciton blocking layers. Furthermore, the graded device could be even more optimized by fine-tuning the layer thicknesses, especially that of the EML. Additionally, an optimized doping concentration could further enhance the efficiency.

5.3   Lifetime

The lifetime of OLEDs plays a crucial role for industrial purposes, especially for display and lighting application. Much work has been attributed to understand the mechanisms behind the observed device degradation and to build optimized OLED-stacks with the aim to enhance their lifetime [6, 70–72, 128, 143].

In this thesis, with the aim to compare the lifetimes of the different stacks and to be able to extrapolate the lifetimes to lower luminance levels, devices were aged at current densities of $5 \, \frac{\text{mA}}{\text{cm}^2}$ and $20 \, \frac{\text{mA}}{\text{cm}^2}$. The measured lifetime-curves were normalized and fitted with a stretched exponential decay function which was introduced in section 2.2:

$$L'(t) = \frac{L(t)}{L_0} = \exp\left[-\left(\frac{t}{\tau}\right)^{\beta}\right] \text{ with } \tau_{1/2} = \ln(2)^{\frac{1}{\beta}} \cdot \tau \tag{5.3}$$

Afterwards, the fitted lifetime values at the two different current densities were used to extrapolate the lifetimes to a practical luminance of $100 \, \frac{\text{cd}}{\text{m}^2}$. The lifetime acceleration constant n can be determined using equation 2.23

$$\tau_{1/2} = \frac{\text{const}}{(L_0)^{\text{n}}} \tag{5.4}$$
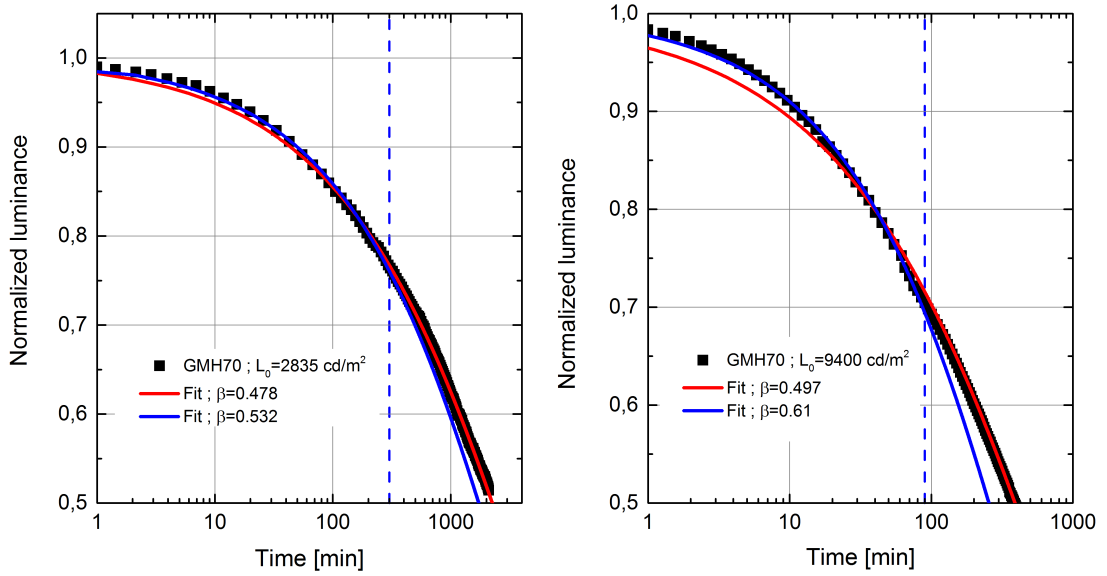
Figure 5.9: Lifetime curves of two GMH70 device at a constant driving current of $5\frac{mA}{cm^2}$ (left) respectively $20\frac{mA}{cm^2}$ (right) and corresponding fits with equation 2.22 (described in the text). The initial luminance is shown in the graph.

so that:

$$n = \frac{\log\left(\frac{\tau_{1/2}^{5mA}}{\tau_{1/2}^{20mA}}\right)}{\log\left(\frac{L_0^{20mA}}{L_0^{5mA}}\right)} \tag{5.5}$$

Now, the constant in equation 5.4 can be calculated and the lifetime can be extrapolated to arbitrary initial luminances. Not all measured devices of the OLED-stacks were aged long enough to justify an analysis. At this point, only a comparison between the GMH and the HS is presented. Furthermore, the properties of the fit function are tested to find out if it can be used for the analyzed OLEDs.

In figure 5.9 the normalized luminance over time (lifetime curves) of GMH70 devices at a current density of $5\frac{mA}{cm^2}$ respectively $20\frac{mA}{cm^2}$ and two fits with equation 2.22 are shown. One of the fits (red line) took into account all of the measured data points, whereas the other one (blue line) only took into account points until 100min (vertical blue dotted line). This particular illustration was chosen to point out that the decay at longer times can be overestimated by the fit, i.e. the lifetimes are underestimated, for the case that the decay was only measured till about 70 % of its initial luminance. Although the initial decay is described better, the long term decay is overestimated and also the value of β at the different current densities differs somewhat. For the case that data points are available till the luminance
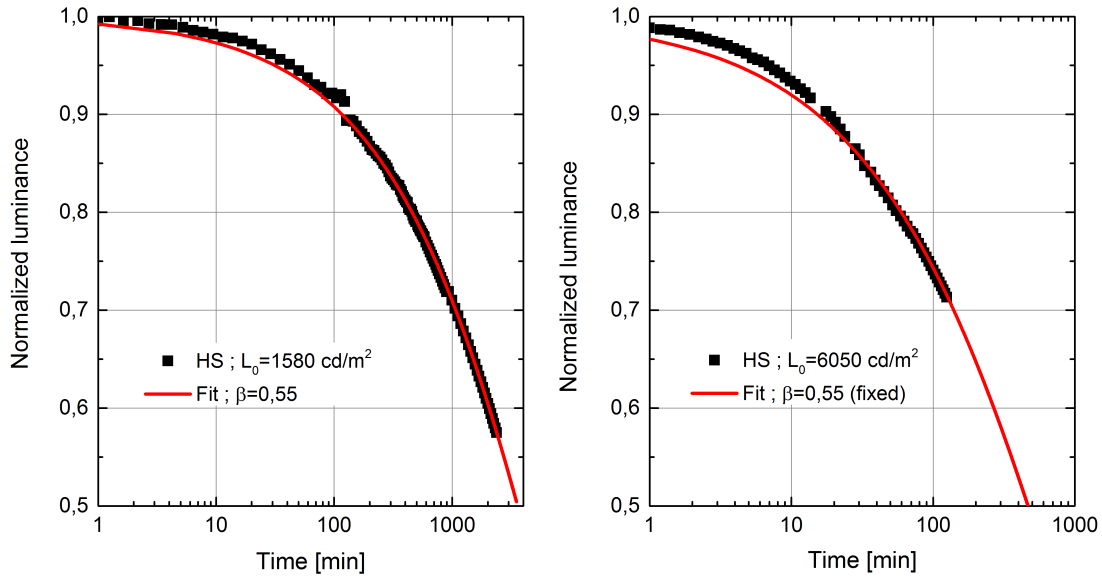
Figure 5.10: Lifetime curves of two HS devices at a constant driving current of $5\,\frac{\mathrm{mA}}{\mathrm{cm}^2}$ (left) respectively $20\,\frac{\mathrm{mA}}{\mathrm{cm}^2}$ (right) and corresponding fits with equation 2.22 (described in the text). The initial luminance is shown in the graph.

degraded to about half its inital value, the fit seems to overestimate the decay for short times slightly, but predicts the decay very well for longer times. Furthermore, the values of β are nearly the same for both current densities, as was also found by Fery and Meerheim [71, 74]. With increasing initial luminance, the overestimation of the decay at short times seems to become a little stronger. The lifetime curves of the HS devices at current densities of $5\,\frac{\mathrm{mA}}{\mathrm{cm}^2}$ respectively $20\,\frac{\mathrm{mA}}{\mathrm{cm}^2}$ are shown in figure 5.10. Here, for the device measured at $20\,\frac{\mathrm{mA}}{\mathrm{cm}^2}$ a shortcut occured before half its initial luminance was reached. From the findings of the two fits to the GMH devices, I decided to extract the fitted value of β from the fit at $5\,\frac{\mathrm{mA}}{\mathrm{cm}^2}$ and fixed it for the fit at $20\,\frac{\mathrm{mA}}{\mathrm{cm}^2}$. In that way, an underestimation of the half-life at $20\,\frac{\mathrm{mA}}{\mathrm{cm}^2}$ as described above was prevented. Similar to the GMH70 devices, the decay at short times is slightly overestimated and the long term decay is described very well. Now, using equation ??, it was possible to perform an estimation of the half-lifes of the two OLED-stacks at a lower luminance.

The fitted half-life values at $5\,\frac{\mathrm{mA}}{\mathrm{cm}^2}$ and $20\,\frac{\mathrm{mA}}{\mathrm{cm}^2}$ and the half-life values extrapolated to $100\,\frac{\mathrm{cd}}{\mathrm{m}^2}$ are presented in table 5.2. As it can be seen, the GMH70 has an extrapolated lifetime of 4938 hours compared to 3837 hours for the HS, which equals an improvement of 29 %. Although this analysis yields only a rough estimation, it can be presumed that the lifetime of the GMH devices in general is superior to that

of HS devices. This statement is further corrobarated by a lifetime measurement of a GMH30 device aged at $20 \frac{mA}{cm^2}$ (see also table 5.2), which exhibited nearly the same initial luminance as the HS device, but showed a higher lifetime of 10.3 hours compared to 6.7 hours, an improvement of 53%.

5.4 Summary

To conclude this chapter, the most important facts are summarized here:

- The GMH70 stack exhibits an outstanding performance compared to all other stacks. This can be attributed to a much better charge balance, broader recombination zone and improved recombination efficiency due to the graded structure. In general, the device structure can be even further improved by making the HTL layer thinner and optimizing the EML thickness. This would result in a reduced driving voltage and higher power efficacy. Possibly also the doping concentration can be fine-tuned. This can be a task for future works.

- The GMH45 and GMH30 stacks showed a superior roll-off behaviour compared to the other stacks. The current density where the roll-off reaches 90% was three times larger compared to the HS and is attributed to a broadened recombination zone. Although the roll-off for the GMH70 device was strongest for low current densities, it became weaker for higher current densities so that the roll-off was reduced for current densities above $100 \frac{mA}{cm^2}$. This effect is attributed to a change of charge balance or the width of the recombination zone with increasing current density.

- It is unclear, why the roll-off for the UMH was not reduced compared to that

Table 5.2: Lifetimes, the parameter β and the corresponding initial luminances of the HS, GMH30 and GMH70 devices at $5 \frac{mA}{cm^2}$ respectively $20 \frac{mA}{cm^2}$. Also shown are the lifetimes and acceleration constant of the HS and GMH70 devices extrapolated to $100 \frac{cd}{m^2}$ using equation 5.4.

	@5 $\frac{mA}{cm^2}$			@20 $\frac{mA}{cm^2}$			extrapolated		
Stack	$L_0 \left[\frac{cd}{m^2}\right]$	$\tau_{1/2}$ [h]	β	$L_0 \left[\frac{cd}{m^2}\right]$	$\tau_{1/2}$ [h]	β	$L_0 \left[\frac{cd}{m^2}\right]$	n	$\tau_{1/2}$ [h]
HS	1580	54.3	0.55	6050	6.7	0.55	100	1.5	3837
GMH70	2835	37.5	0.475	9410	6.5	0.483	100	1.7	4937
GMH30				6100	10.3	0.564			

of the HS. It can be assumed that it exhibits a loss of charge balance at higher current density so that the recombination zone is at the vicinity of one of the interfaces resulting in increased quenching effects. The applied mixing ratio of TCTA and TPBI was reported to yield efficient charge balance [78], but most possibly it has to be fine-tuned for this OLED structure.

- The measured emission spectra indicate that the recombination zone for the OLEDs with mixed structures is shifting with increasing current density. This implicates that for devices with graded host structures the recombination zone is not restricted to one of the interfaces, which should result in a broadened recombination zone

- The GMH70 and GMH30 show an improved lifetime compared to that of the HS. For the GMH70 device a lifetime improvement of 29 % was estimated at a luminance of $100\,\frac{cd}{m^2}$. At $6000\,\frac{cd}{m^2}$ a GMH30 device even showed an lifetime improvement of 53 % compared to a HS device.
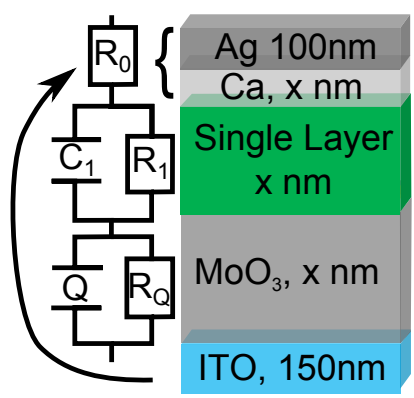
Table 5.3: Summary of the averaged and maximum efficiencies and the corresponding driving voltages of all devices at $200\,\frac{cd}{m^2}$ respectively $10\,\frac{kcd}{m^2}$.

Stack		@200 $\frac{cd}{m^2}$			@10 $\frac{kcd}{m^2}$		
		$\eta_P\left[\frac{lm}{W}\right]$	EQE[%]	V_D [V]	$\eta_P\left[\frac{lm}{W}\right]$	EQE[%]	V_D [V]
HS	average	29	9.3	3.63	13.7	8	6.77
	max	31.9	10.38		14.3	8.7	
UMH	avarage	31.3	10.3	3.70	13.2	9.2	7.93
	max	32.4	11.1		13.9	9.5	
GMH30	average	29.6	8.9	3.44	14.5	8.6	6.73
	max	30.8	9.5		14.9	8.9	
GMH45	average	31.9	10.1	3.64	14.9	10	7.55
	max	32.1	11		15.1	10.6	
GMH70	average	45.9	15.3	3.80	15.1	13.4	10.08
	max	48.2	16.4		15.9	14	

6. Identifying intermixing in the light emitting layer by impedance spectroscopy

In this chapter the results of the impedance measurements are presented. To be able to analyze multiple layers of organic materials with impedance spectroscopy, firstly the single materials have to be characterized. The results of such a characterization are presented in section 6.1. In section 6.2 the results of the measurements of devices with graded intermixed layers are presented. For all impedance spectra analyzed in this thesis, the total complex impedance Z of the chosen circuit representation was used as a fit function and the fits were weighed with $|Z|^2$ as suggested in the Agilent handbook. The fits yielded $\mathrm{Re}(Z)$ and $\mathrm{-Im}(Z)$ from which the conductance and capacitance spectra (equations 2.39 and 2.40) were calculated and directly compared to the measured spectra.

Table 6.1: Structures and equivalent circuit representation of all single layer devices investigated with impedance spectroscopy. The numbers are thicknesses in nm.

Stack	MoO$_3$	Layer	Ca
M1	70	-	-
M2	10	-	10
TCTA1	-	TCTA, 50	-
TCTA2	5	TCTA, 90	-
TCTA3	10	TCTA, 40	-
TPBI1	-	TPBI, 80	-
TPBI2	-	TPBI, 50	10
Mix	-	TCTA:TPBI (50:50), 50	-

6.1 Characterization of the materials

In this section the different materials used in this thesis are characterized. Several stacks of single materials with and without contacting layers and the contacting layers themselves are analyzed.

The ITO and Ag layers are expected to be too thick and too conductive to be visible in the impedance spectrum. Probably also Ca is also too conductive, but the Ca layer
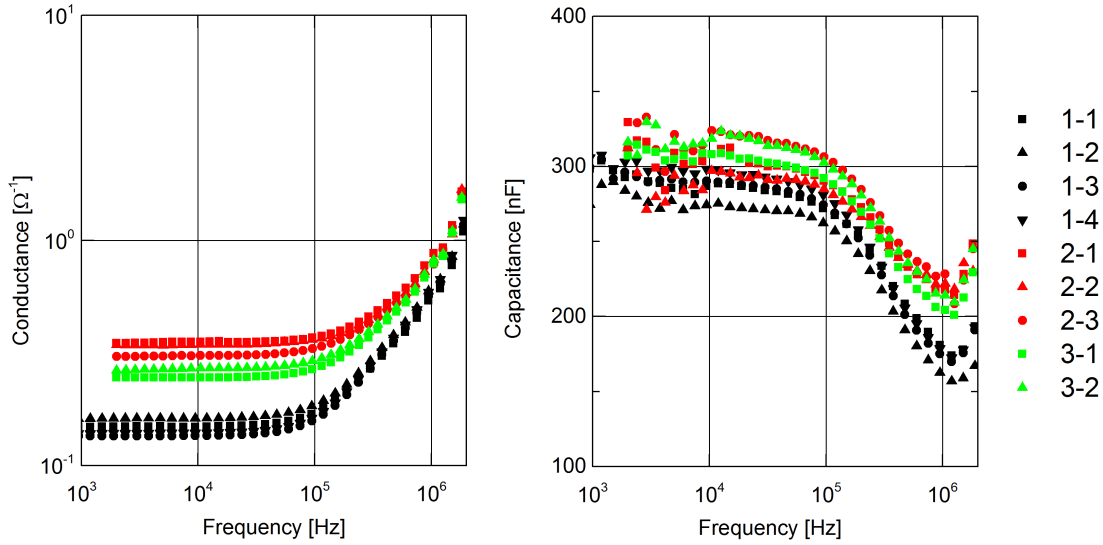
Figure 6.1: Conductance and Capacitance of all devices with a 70nm thick MoO_3 layer. For better visualisation, only every 4th data point is shown.

in the OLEDs with a dielectric constant of about 3 is only 10 nm thick so that its capacitance could influence the impedance spectra at very high frequencies. Furthermore, the workfunction difference of the contacting layers - ITO$\approx$5.2 eV, Ca$\approx$2.8 eV, Ag$\approx$ 4.4 eV - possibly result in the presence of space charges at the interfaces of the organic and contacting layers (compare figure 2.17) and could also influence the spectrum. To be able to quantify these effects also for the measurements for the complete OLEDs, all of the stacks presented in this section were sandwiched between between the 150 nm thick ITO and a 100 nm thick Ag layer. Furthermore, the influence of Ca and MoO_3 was analyzed. The structures of all stacks examined in this section are summarized in table 6.1.

6.1.1   Contacting layers: MoO_3 and Ca

For the analysis of stacks with multiple layers it will be important to model the influence of MoO_3, Ca and the effect of space charges on the impedance spectra as precise as possible. Two different equivalent circuits were fitted to the impedance data of two stacks containing a MoO_3 layer and both yielded reasonable results. The first one is a parallel circuit of a resistance R_1 and capacitance C_1 in series with a parallel combination of a resistance and a constant phase element Q using the parameter α:

$$Z_1 = \frac{R_1}{1 + i\omega R_1 C_1} + \frac{R_2}{1 + (i\omega)^{\alpha} R_2 Q} + R_0 \tag{6.1}$$

Figure 6.2: Conductance and capacitance spectra of device 3-2, a single layer fit with equation 6.2 and a double layer fit with equation 6.1. Above 1MHz, the capacitance spectrum is influenced by the inductance and excluded from the fit.

The second one is a single-layer circuit consisting of a parallel combination of a resistance and Q using the parameter β:

$$Z_2 = \frac{R_1}{(1 + i\omega R_1 Q)^\beta} \tag{6.2}$$

Stack M1: MoO$_3$ (70 nm)

For thick layers of MoO$_3$ ($d \approx 500\,\text{nm}$) a three layer behaviour with dielectric constants for each layer of above 100 has been reported in impedance measurements [144]. These layers account for the contributions of the lattice bulk, the grain boundaries (caused by trapped charges due to impurities) and mobile ionic charge carriers respectively. Furthermore, it was reported that the capacitance in MoO$_3$ single layers is mainly defined by an accumulation of the mobile ionic charge carriers at the electrodes leading to space charge polarization when applying an AC voltage [145]. At higher frequencies a reduced capacitance was found, attributed to a declining concentration of these accumulated charge carriers.

Due to the high conductivity of MoO$_3$ compared to the organic materials, the effect of a thin MoO$_3$ layer in combination with thin nearly insulating layers of organic materials on the impedance measurements is not expected to be strong at

low frequency (compare equation 2.41). However, the capacitance possibly cannot be ignored for high frequencies (compare equation 2.42). To analyze this in detail, devices with a 70 nm layer of MoO_3 between ITO and Ag were prepared. In figure 6.1 the conductance and capacitance spectra of all such devices are presented. Devices on the same substrate (depicted with the same colour) show similar characteristics. This effect was observed for most of the impedance measurements carried out in this thesis and can probably be attributed to slight differences in the layer characteristics on the different substrates. The capacitance indeed exhibits a decrease at high frequencies as reported in [145] and the conductance shows an UDR like AC behaviour (compare section 2.3.2).

The data of device 3-2 and the corresponding fits with equations 6.1 and 6.2 are depicted in figure 6.2. Both equivalent circuits describe the characteristics of conductance and capacitance very well. At high frequencies there is a steep increase in the capacitance, which can be attributed to the inductance. An inductance will be included in the fit for the organic layers in the next section. The advantage of the single layer representation in equation 6.2 is that it consists of only 3 free parameters for the fit as opposed to 5 parameters in equation 6.1. This can be helpful for more complicated layers with even more free parameters.

Stack M2: MoO_3 (10 nm) + Ca(10 nm)

Table 6.2: Averaged results of the fits for the two stacks containing MoO_3.

Parameter	M1 (9 devices)	M2 (8 devices)
σ_{DC_1} in $\frac{1}{\Omega m}$	$(3.2 \pm 0.4) \cdot 10^{-3}$	$(6.2 \pm 1.4) \cdot 10^{-5}$
ϵ_r	148 ± 21	14.0 ± 1.0
σ_{DC_2} in $\frac{1}{\Omega m}$	$(9.5 \pm 0.4) \cdot 10^{-4}$	$(2.8 \pm 1.0) \cdot 10^{-5}$
Q in $F^{1/\alpha}$	$(5.8 \pm 0.7) \cdot 10^{-6}$	$(1.4 \pm 1.8) \cdot 10^{-6}$
α	0.81 ± 0.08	0.79 ± 0.06
σ_{DC} in $\frac{1}{\Omega m}$	$(7.2 \pm 2.7) \cdot 10^{-4}$	$(3.2 \pm 0.4) \cdot 10^{-3}$
Q in F	$(4.2 \pm 0.2) \cdot 10^{-7}$	$(3.3 \pm 1.0) \cdot 10^{-7}$
β	0.72 ± 0.02	0.5 ± 0.1

To check if equation 6.2 is also applicable as a fit function for thinner layers of MoO_3 in combination with a thin layer of Ca as they are present in the GMH OLEDs,
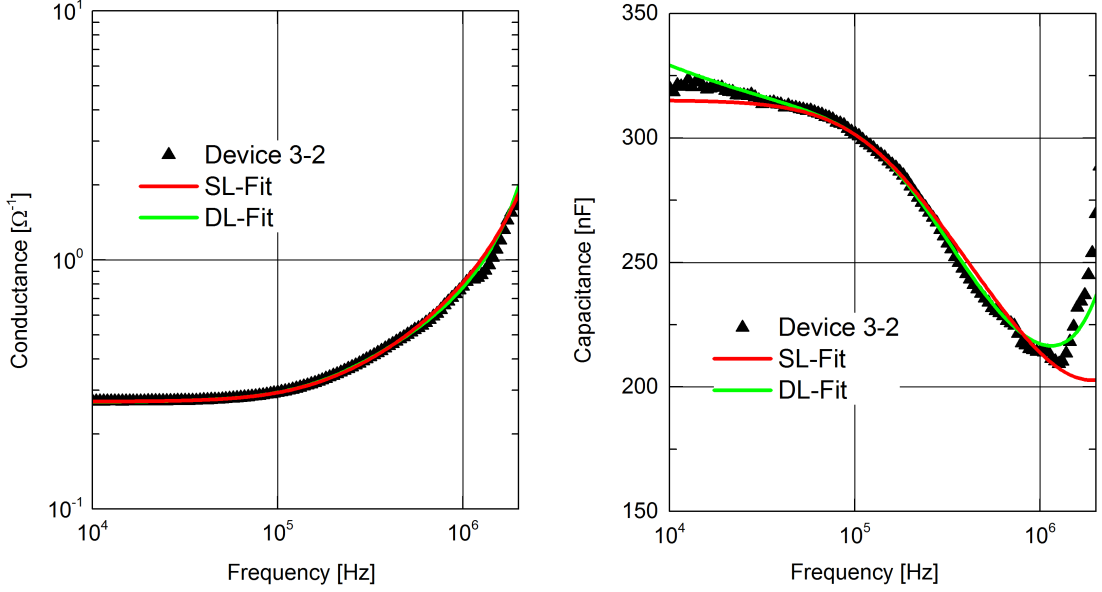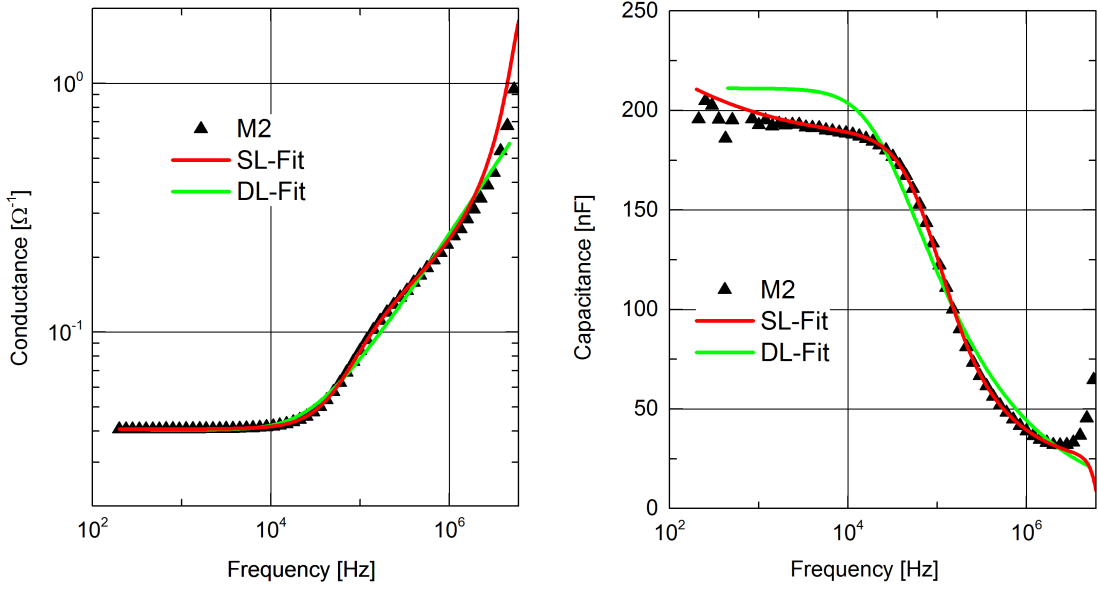
Figure 6.3: Conductance and capacitance spectra of device 1-2, a single layer fit with equation 6.2 and a double layer fit with equation 6.1.

devices with a 10nm thick MoO_3 and 10nm thick Ca layer were prepared. Fits with equations 6.1 and 6.2 were performed and the results for device 3-3 are shown in figure 6.3. The characteristics resemble these of the thicker MoO_3 layer and no direct influence of Ca on the spetrum can be identified. Although the single layer fit in this case is not describing the data as well as the double layer fit, it still models the general behaviour quite well. In the next section the use of equation 6.2 to model the influence of MoO_3 (plus possible space charge effects) on the impedance spectra will be justified. The averaged fit parameters for all devices of the M1 and M2 stacks are presented in table 6.2. Here it was assumed that the capacitance can be described by equation 2.28 for the RC-element in the fit with equation 6.1. In that case, for the M1 stack a dielectric constant of $\epsilon = 148 \pm 21$ was found, similar to the values reported in [144].

6.1.2 Single semiconducting layers

As a next step, single layers of TCTA and TPBI with varying thicknesses with and without MoO_3 respectively Ca were prepared. This was done to characterize the organic layers and also to check the influence of the contacting layers on the spectra. For the single organic layers, equation 2.32 in combination with the frequency dependence of the conductivity and dielectric constant described by equations 2.43
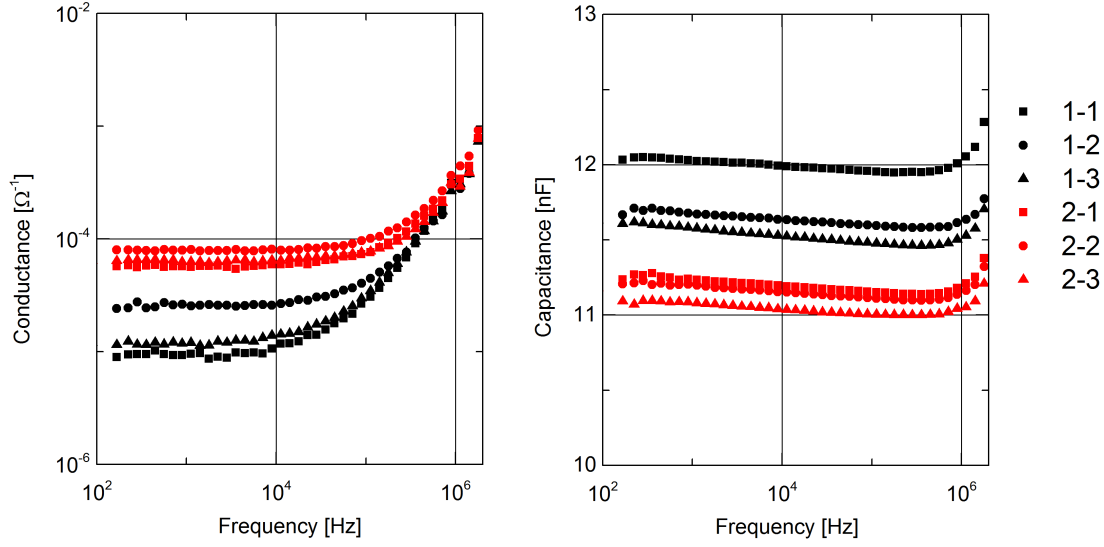
Figure 6.4: Conductance and Capacitance of all devices with a 50nm thick TCTA layer.

and 2.44 was used as an equivalent circuit. The possible influence of the contacting layers and space charges was modelled by equation 6.2. Taking the inductance of the electrical circuit into account, the modified total impedance of an organic single layer was defined as

$$Z_{\mathrm{SL}} = \frac{d}{A} \cdot \frac{1}{\sigma(\omega) + i\omega\epsilon_0\epsilon_{\mathrm{r}}(\omega)} + \frac{R_{\mathrm{Q}}}{(1 + i\omega R_{\mathrm{Q}} Q)^{\beta}} + i\omega L + R_0, \qquad (6.3)$$

with the frequency dependent conductivity and dielectric constant:

$$\sigma(\omega) = \sigma_{\mathrm{DC}} + \sigma_{\mathrm{AC}} \cdot \omega^s \qquad (6.4)$$

$$\epsilon_{\mathrm{r}}(\omega) = \left(\epsilon_{\infty} + \frac{\sigma_{\mathrm{AC}}}{\epsilon_0} \cdot \tan\left(\frac{\pi s}{2}\right) \omega^{s-1} \right) \qquad (6.5)$$

Stack TCTA1: TCTA (50 nm)

To make sure, that all effects which could arise from Ca or MoO_3 are excluded, devices with a single 50 nm thick TCTA layer were prepared. The only possible influence are space charges at the interfaces of TCTA to ITO or Ag, caused by the work function difference of the electrodes. In figure 6.4 the conductance and capacitance spectra of all such devices are depicted. As expected from UDR theory, they all exhibit a
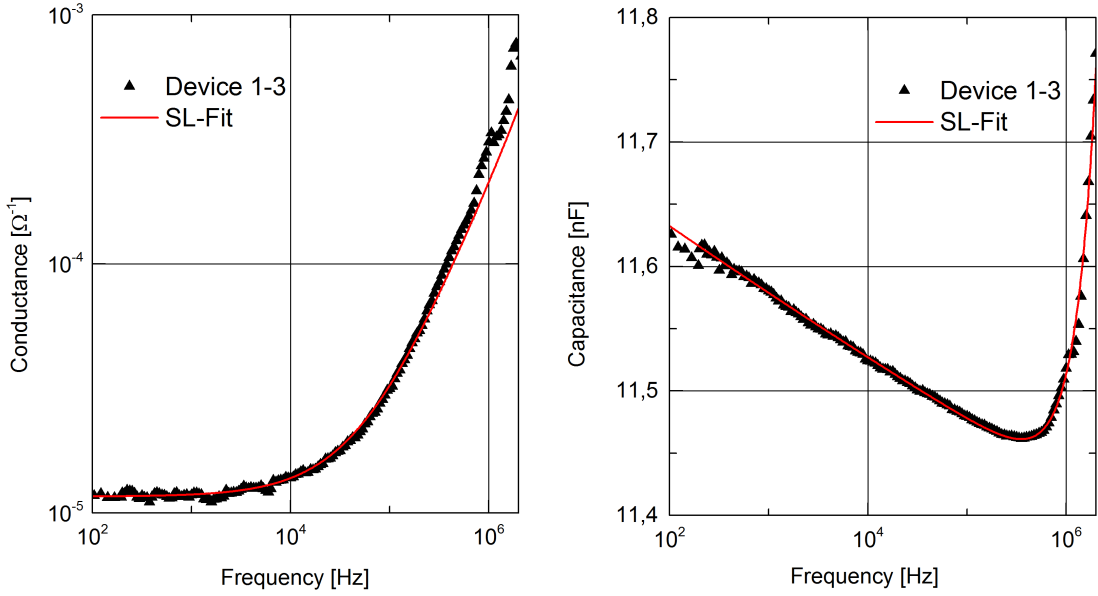
Figure 6.5: Conductance and Capacitance of sample 2-2 and the corresponding fit with equation 6.3. The fit parameters are shown.

slight decrease in capacitance with increasing frequency and the conductivity exhibits an AC behaviour at high frequencies. The values of the capacitance are scattered between 11 nF and 12 nF. On the one hand, this can be explained by small variations of the layer thickness, which are caused by the different positions of the substrates in the substrate holder. This is further supported by noticing that devices on the same substrate show very similar capacitances. One the other hand, even if the dielectric constant is expected to be quite constant, small variations from layer to layer are not unrealistic. As can be seen, the values of the DC-conductance at low frequencies vary over about one order of magnitude. Differences of the intrinsic charge carrier concentration or of the density of trapped charges are probably a reason for that effect.

The imaginary part of the impedance is influenced by the inductance of the electrical leads in the region above 1MHz. This results in a steep increase of the capacitance spectra. This influence can be modelled by the fit and was present for all impedance measurements performed in this thesis. It always equaled about $(3 \pm 1) \cdot 10^{-8}$ H. The spectra of device 1-3 and a corresponding SL-Fit fit with equation 6.3 are presented in figure 6.5. It is possible to describe the spectrum over the whole frequency range without the CPE term in equation 6.3, i.e. $R_Q = 0$. For the other parameters, the fit yielded $\sigma_{DC} = 2.4 \cdot 10^{-8} \frac{1}{\Omega m}$, $\sigma_{AC} = 8.6 \cdot 10^{-14} \frac{1}{\Omega m}$ and

$s = 0.982$.

The parameters σ_{AC} and s are both used to describe the frequency behaviour of the conductance and capacitance. For a better comparison, I decided to take the average value of s of all fits of the 50 nm TCTA layer which gave reasonable values between 0.9 and 1: $s = 0.976 \pm 0.008$. All the fits were afterwards repeated with s fixed at this value and the parameter σ_{AC} was left a free parameter. This value for s was also used for the fits of the other layers incorporating TCTA. The averaged results for the fit parameters of the TCTA1 stack are included in table 6.3.

Stack: TCTA2: TCTA $(40\,\text{nm})$ **+ MoO$_3$** $(10\,\text{nm})$

A double layer consisting of 40 nm TCTA and 10 nm MoO$_3$ was prepared to check if the fit function introduced in 6.1.1 can be used to model the influence of MoO$_3$ on the impedance spectra when combined with thin layers of organic materials. As all single layer stacks in this section show a behaviour similar to that of the TCTA1 stack in figure 6.4, I decided to present the data and fits for one characteristic device for all stacks from here on.

In figure 6.6a and 6.6b the conductance and capacitance spectra and the corresponding fits of such a characteristic device are shown. As can be be seen, at high frequencies the capacitance exhibits a slight decrease, which possibly can be attributed to MoO$_3$. Due to its much higher conductivity, MoO$_3$ should not influence the spectra at low frequencies. Therefore, to extract the parameter values for TCTA, a SL-Fit for frequencies of $f < 1 \cdot 10^4\,\text{Hz}$ (plateau of the capacitance) was performed ($R_Q = 0$ and $L = 0$ in equation 6.3). To varify that this can be done, the data of device 2-2 from the TCTA1 stack are also included in the graph. The data points have been scaled by the factor $\frac{d1}{d2}$ according to the thickness difference of the layers and then been shifted on the y-axis for better visualisation. The frequency dependence of conductance and capacitance then should exhibit the same characteristics as the TCTA2 layer at low frequencies. Having a look at the capacitance, one can see that this is true. That verifies that the additional decrease of the capacitance at high frequencies and the earlier onset of the increase of the conductance can solely be attributed to the MoO$_3$ layer.

The results of this fit are $\sigma_{DC} = 5.7 \cdot 10^{-8}\,\frac{1}{\Omega\text{m}}$, $\sigma_{AC} = 8 \cdot 10^{-14}\,\frac{1}{\Omega\text{m}}$ and $\epsilon_\infty = 2.42$ (with s fixed at 0.9764). The value of σ_{AC} was fixed for the DL-Fit, which incooperates the CPE-element. The DL-Fit yields $R_Q = 1.2\,\Omega$, $Q = 5.7 \cdot 10^{-7}\,\text{F}$, $\beta = 0.8$ and can describe the data over the whole frequency range. The averaged data of all TCTA2 devices are included in table 6.3.
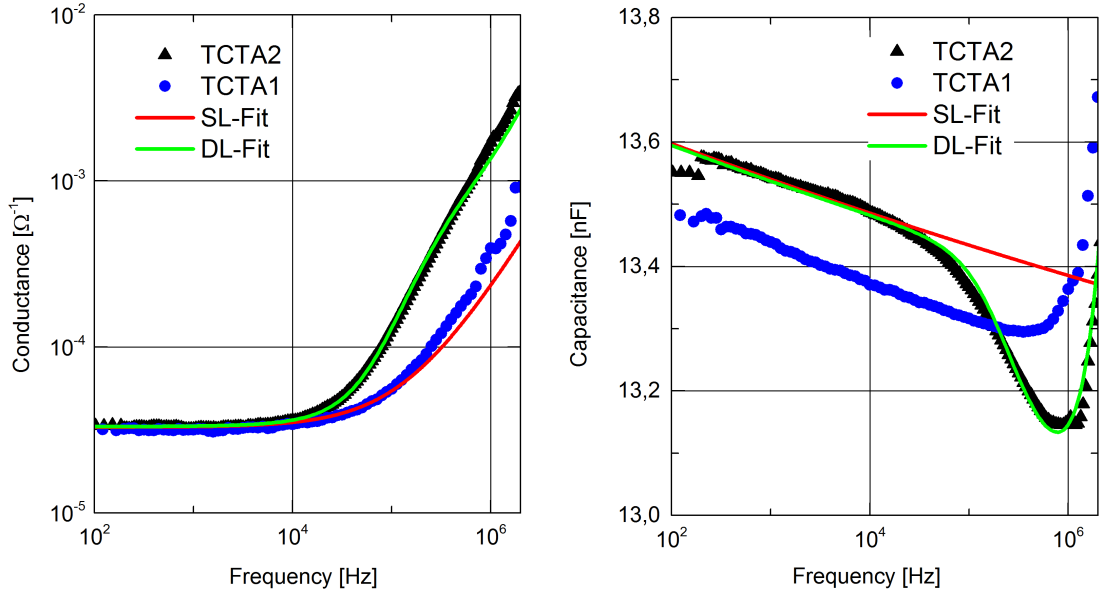
(a) Conductance of a device with a 40 nm thick TCTA+10 nm thick MoO$_3$ layer and the corresponding single- and double layer fits. Also included are the scaled data of a TCTA1-device.

(b) Capacitance of a device with a 40 nm thick TCTA+10 nm thick MoO$_3$ layer and the corresponding single- and double layer fits.

Figure 6.6

Stack TCTA3: TCTA (90 nm) + MoO$_3$ (5 nm)

A double layer of 90 nm TCTA and 5 nm MoO$_3$ was prepared to check if the material parameters of TCTA change for higher layer thicknesses and to see the effect of an even thinner layer of MoO$_3$. The spectra of a characteristic device and the corresponding fits are depicted in figure 6.7a. The scaled data of device 2-2 from the TCTA1 stack are again included for comparison. The SL-fit is again a fit to the plateau of the capacitance and shows similar characteristics compared to the TCTA1 spectra. It yields values of $\sigma_{DC} = 6.1 \cdot 10^{-8} \frac{1}{\Omega m}$, $\sigma_{AC} = 5 \cdot 10^{-14} \frac{1}{\Omega m}$ and $\epsilon_\infty = 2.77$ (s fixed at 0.9764) and were fixed for the DL-Fit. The DL-Fit describes the data over the whole frequency range very well and the results are: $R_Q = 18.2\Omega$, $Q = 4.7 \cdot 10^{-7}$ F and $\beta = 0.89$. The earlier onset of the additional decrease of the capacitance and increase of the conductance can be explained by the higher resistance of the MoO$_3$ layer compared to that in the TCTA2 stacks. Such variations of the MoO$_3$ resistance were also present for the measurements in section 6.2 and can always be modelled by the CPE-element. The averaged data of all TCTA3 devices are included in table 6.3.

The strong deviation of ϵ_∞ between the three TCTA stacks can be explained by the fact that the frequency dependance defined by σ_{AC} and s in equation 6.5 is varying. Iin the frequency range of interest for impedance spectroscopy, the absolute values of the dielectric constant defined by equation 6.5 are similar. To point that out, the averaged parameters of the three stacks were used to calculate the values of ϵ_r at a frequency of 1000 Hz with equation 6.5 and are also included in 6.3. As can be seen, all stacks yield a similar dielectric constant.

(a) Conductance of sample 1-1 with a 90 nm thick TCTA+10nm thick MoO_3 layer and the corresponding single- and double layer fits.
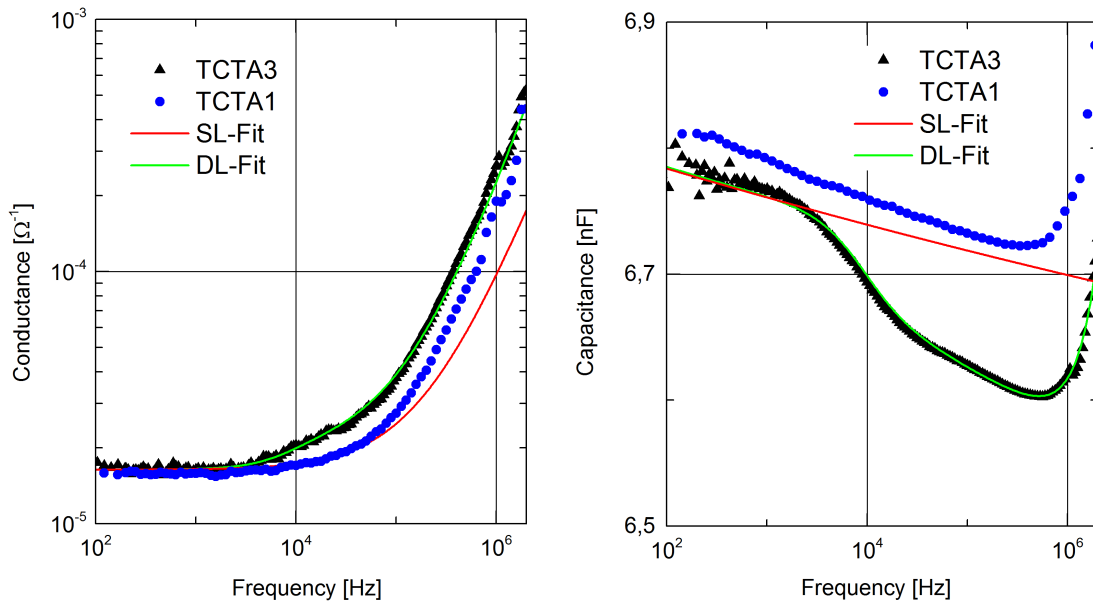
(b) Capcitance of sample 1-1 with a 90 nm thick TCTA+10nm thick MoO_3 layer and the corresponding single- and double layer fits.

Figure 6.7

Stack TPBI1: TPBI (80 nm)

A 80nm thick TPBI layer was prepared to extract the material parameters of TPBI and minimize influences of additional layers. The spectra of conductance and capacitance for a characteristic device and the corresponding fits are shown in figure 6.8. Same as for the TCTA2 and TCTA3 stacks, the SL-Fit to the plateau of the capacitance alone cannot explain the slope of the conductance at high frequencies. Applying a DL-Fit resolves this issue and the whole spectrum can be fitted very well. The fit results are: $\sigma_{DC} = 1.4 \cdot 10^{-7} \frac{1}{\Omega m}$, $\sigma_{AC} = 3 \cdot 10^{-14} \frac{1}{\Omega m}$, $\epsilon_\infty = 3.56$, $R_Q = 0.4\Omega$, $Q = 3.6 \cdot 10^{-6} F$ and $\beta = 0.63$. As can be seen, the resistance of the CPE-element
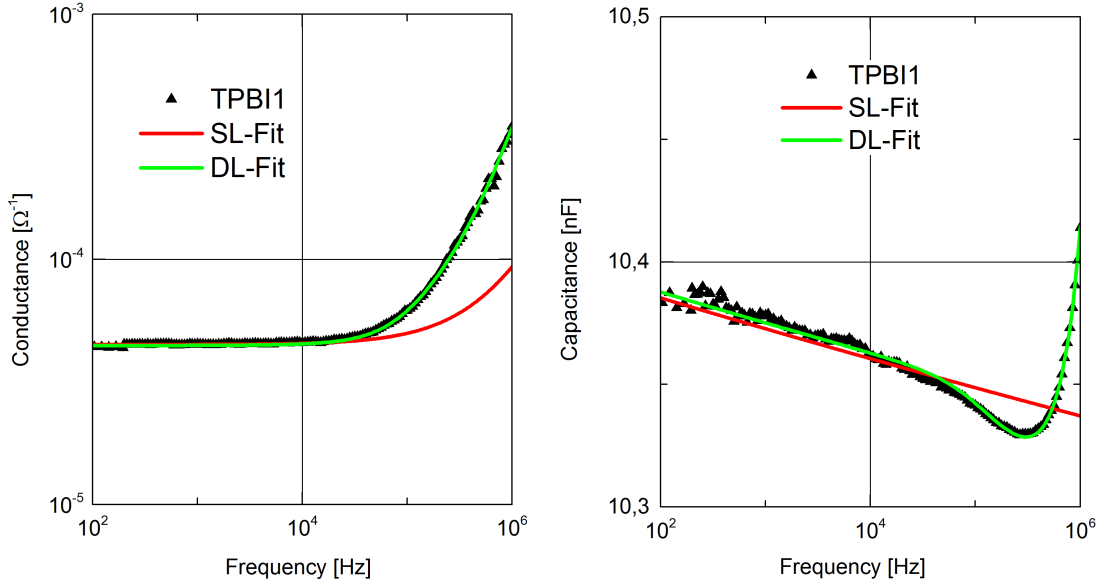
Figure 6.8: Conductance and Capacitance of a device with a 80 nm thick TPBI layer.

was quite low and was possibly caused by space charges at the interfaces. Same as for the TCTA stacks, I decided to extract the average value of s from all fits which gave a reasonable value, $s = 0.987 \pm 0.004$ and repeat the fits with a fixed s. The averaged values of all devices are summarized in table 6.4.

Stack TPBI2: TPBI $(50\,\text{nm}) + \textbf{Ca}\ (10\,\text{nm})$

The influence of Ca was examined by preparing devices with a 50nm thick TPBI layer and a 10nm Ca layer. The spectra of a characteristic device and the corresponding fits are depicted in figure 6.9. Again the characteristic UDR behaviour can be observed, but at high frequencies an additional decrease of the capacitance can be observed. This is either caused by the higher workfunction difference of Ca/ITO compared to Ag/ITO and the resultant increased number of space charges at the interfaces or by the capacitance of the Ca layer. Same as for the TCTA2 and TCTA3 stacks, the SL-fit was fitted to the plateau of the capacitance to extract the material parameters of TPBI. Subsequently, the CPE-element was included in the fit and the additional decrease in capacitance and increase in conductance can be modelled very well. The results of the fits are: $\sigma_{\text{DC}} = 2.4{\cdot}10^{-7}\frac{1}{\Omega\text{m}}$, $\sigma_{\text{AC}} = 4.2{\cdot}10^{-14}\frac{1}{\Omega\text{m}}$, $\epsilon_\infty = 2.96$, $R_2 = 3.8\Omega$, $Q = 3.8 \cdot 10^{-6}\text{F}$ and $\beta = 0.73$. The averaged parameters of this stack are included in 6.4.
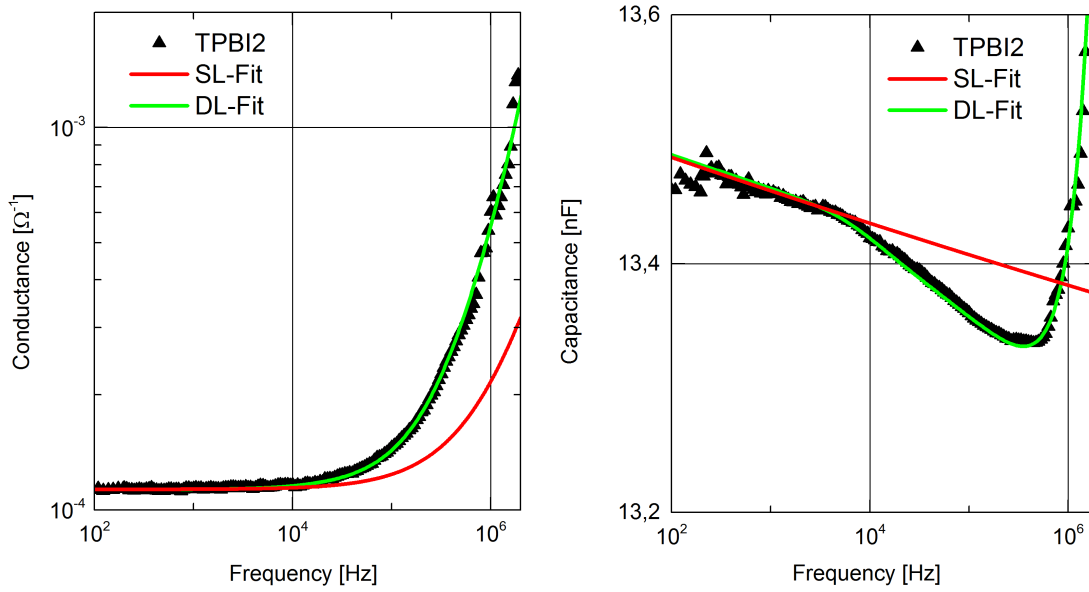
Figure 6.9: Conductance and capacitance of a device with a 50 nm thick TPBI+10 nm thick Ca layer and the corresponding single- and double layer fits.

Stack Mix: TCTA:TPBI (50:50) (50 nm)

An estimation of the material parameters in a mixed layer of TCTA and TPBI was performed by preparing devices with a 50nm thick uniformly mixed layer of TCTA:TPBI with a ratio of 50:50. The spectra of conductance and capacitance of a characteristic device and a DL-Fit are shown in figure 6.10. The spectra resemble very much the characteristics of the single layer devices and there is a slight additional decrease of the capacitance at high frequencies. The data can be very well described by the DL-fit and the results are: $\sigma_{\mathrm{DC}} = 2.4{\cdot}10^{-7}\,\frac{1}{\Omega\mathrm{m}}$, $\sigma_{\mathrm{AC}} = 4.2{\cdot}10^{-14}\,\frac{1}{\Omega\mathrm{m}}$, $\epsilon_{\infty} = 2.96$, $R_2 = 3.8\,\Omega$, $Q = 3.8 \cdot 10^{-6}\,\mathrm{F}$ and $\beta = 0.73$. The averaged parameters of all devices are included in table 6.4. As can be seen, the averaged values of σ_{AC} and ϵ_{∞} are somewhere in between the values of the pure materials. The important information is, that the dielectric constant is not completely different from that of the pure materials. That means, we can expect some kind of transition from the value for pure TCTA to that of pure TPBI in an intermixed layer. Even if the mixed layer exhibits a slightly higher dielectric constant than expected from the transition described by equation 2.51, this would only result in a slight overestimation of the layer thickness of the intermixed region.
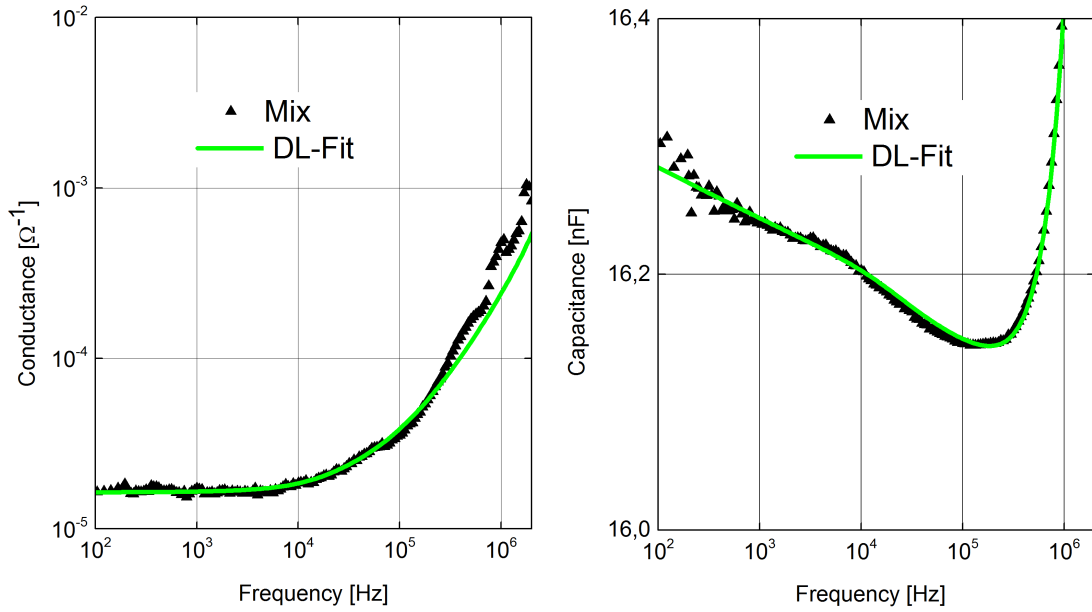
Figure 6.10: Conductance and capacitance of a device with a 50 nm uniformly mixed layer of TCTA:TPBI (50:50) and the corresponding double layer fit.

Conclusion

For the fits of the stacks with multiple layers we need to fix the material parameters of the pure materials. The conductivity σ_{DC} always has to remain a free parameter for the fits, because it varies slightly from layer to layer. For the other parameters it is straight forward to take the average of the parameter values of all stacks examined in this section. The averaged values are summarized in table 6.5. The CPE-element has proven to be able model additional influences introduced by MoO_3, Ca or space charges very well. Yet, the parameters of the CPE-elements also have to remain free parameters. For the stacks presented in the next section, these external influences are only observable at very high frequencies and should not impede the identifying of intermixing.

Table 6.3: Averaged results of the fits of the three stacks containing a TCTA layer. The paramaters of all stacks were averaged.

Stack Parameter	TCTA1 (9 devices)	TCTA2 (6 devices)	TCTA3 (7 devices)
σ_{DC} in $\frac{1}{\Omega m}$	$5.8 \cdot 10^{-8}$	$3.7 \cdot 10^{-8}$	$3.4 \cdot 10^{-8}$
σ_{AC} in $\frac{1}{\Omega m}$	$(7.9 \pm 0.8) \cdot 10^{-14}$	$(1.3 \pm 0.3) \cdot 10^{-13}$	$(4.0 \pm 0.6) \cdot 10^{-14}$
ϵ_∞	2.49 ± 0.08	2.32 ± 0.10	2.76 ± 0.04
s	0.9764 ± 0.0023	0.9764 (fixed)	0.9764 (fixed)
$\epsilon_r(\omega)@10^3$ Hz	2.69	2.64	2.84
R_Q in Ω	0	14 ± 8	1.3 ± 0.3
Q in F	-	$(9.4 \pm 4.1) \cdot 10^{-7}$	$(7.8 \pm 2.5) \cdot 10^{-7}$
β	-	0.7 ± 0.1	0.77 ± 0.12

Table 6.4: Averaged results of the fits for the two stacks containing a TPBI layer and the stack with a uniformly mixed layer of TCTA:TPBI (50:50).

Stack Parameter	TPBI1 (14 devices)	TPBI2 (9 devices)	Mix1 (6 devices)
σ_{DC} in $\frac{1}{\Omega m}$	$9.3 \cdot 10^{-8}$	$5.9 \cdot 10^{-8}$	$4.1 \cdot 10^{-8}$
σ_{AC} in $\frac{1}{\Omega m}$	$(3.9 \pm 1.2) \cdot 10^{-14}$	$(3.4 \pm 0.4) \cdot 10^{-14}$	$(4.9 \pm 0.6) \cdot 10^{-14}$
ϵ_∞	3.02 ± 0.15	3.33 ± 0.21	2.90 ± 0.05
s	0.987 ± 0.002	0.987 (fixed)	0.987
R_Q in Ω		4.6 ± 2.7	1.9 ± 1.5
Q in F	-	$(5.6 \pm 1.7) \cdot 10^{-6}$	$(8.5 \pm 3.2) \cdot 10^{-6}$
β	-	0.74 ± 0.05	0.7 ± 0.1

Table 6.5: Averaged parameter values for the pure materials.

Parameter	TCTA	TPBI
σ_{AC} in $\frac{1}{\Omega m}$	$8.6 \cdot 10^{-14}$	$3.7 \cdot 10^{-14}$
ϵ_∞	2.51 ± 0.05	3.17 ± 0.13
s	0.976	0.987

6.2 Analysis of devices with a graded mixed structure.

Finally, we can analyze devices with a graded structure. As introduced in section 2.3.4, the two equivalent circuits to model the impedance of an organic double layer are:

$$Z_{\text{mix,DL}} = R_0 + \frac{1}{A} \int_0^d \frac{\mathrm{d}x}{\sigma(\chi(x)) + i\omega\epsilon_0\epsilon_r(\chi(x))} \tag{6.6}$$

$$Z'_{\text{mix,DL}} = Z_{\text{mix,DL}} - \int_{d_1}^{d_1+h} \frac{\mathrm{d}x}{\sigma(\chi(x)) + i\omega\epsilon_0\epsilon_r(\chi(x))} + \int_{d_1}^{d_1+h} \frac{\mathrm{d}x}{\sigma'(\chi(x)) + i\omega\epsilon_0\epsilon_r(\chi(x))} \tag{6.7}$$

The concentration profile describing the transition of the material parameters is defined by:

$$\chi(x) = \frac{1}{2}\left[1 - \tanh\left(\frac{x-g}{ah}\right)\right] \tag{6.8}$$

In section 4.3 the normalized evaporation rates of the three OLED stacks with graded mixed host structures are illustrated (compare figure 4.5). It is straight forward to fix the parameter a 6.8 in such a way that the modelled transition width of the material parameters exhibits a similar shape. For that purpose, I defined $a = \frac{1}{4.6} \approx 0.22$. In that case, equation 6.8 at the transition to the pure layers equals $\chi(x) = 0.99$ as shown in figure 2.19. Taking into account the influence of the MoO_3 layer, space charges and the inductance, the two fit functions compared in this section are:

$$\textbf{Fit1}: \quad Z_{\text{tot,mix1}} = Z_{\text{mix,DL}} + \frac{R}{(1 + RQ(i\omega))^\beta} + R_0 + i\omega L \tag{6.9}$$

Table 6.6: Structures of all devices with a graded mixed structure investigated with impedance spectroscopy. The numbers are thicknesses in nm.
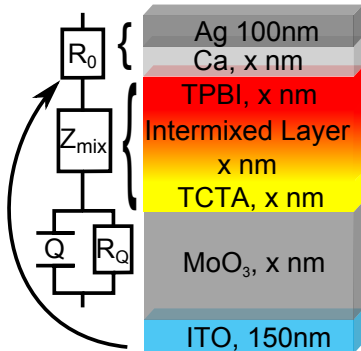
Stack	MoO_3	TCTA	Intermixed layer	TPBI	Ca
GM35	0	50	35	45	0
GMH30	10	50	$30 + \text{Ir(ppy}_3)(7\%)$	30	10
GMH45	10	50	$45 + \text{Ir(ppy}_3)(7\%)$	30	0
GMH70	10	50	$70 + \text{Ir(ppy}_3)(7\%)$	30	0
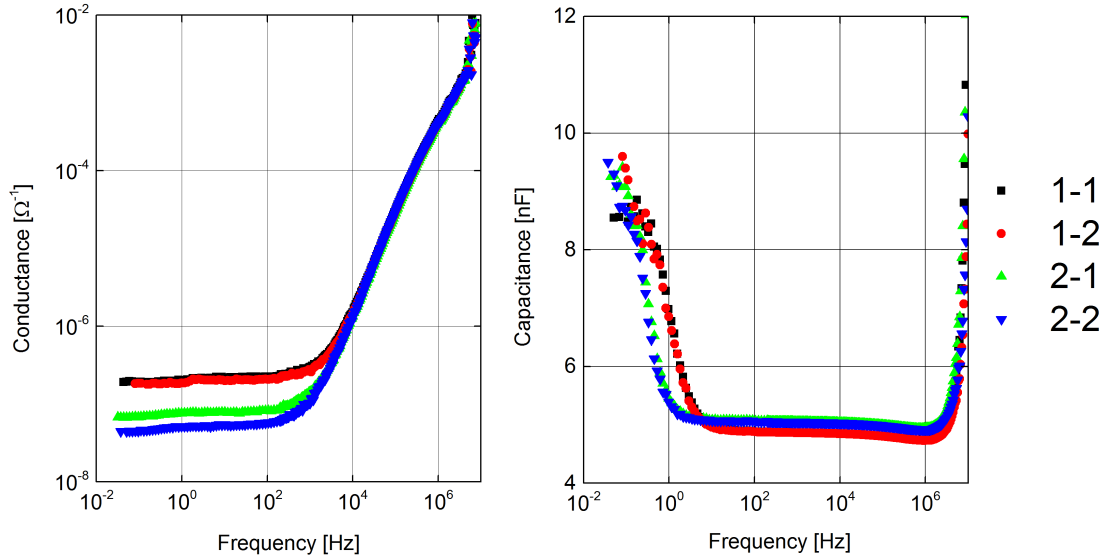
Figure 6.11: Conductance and Capacitance all devices with a 35nm thick intermixed transition layer.

$$\textbf{Fit2}: \quad Z_{\text{tot,mix2}} = Z'_{\text{mix,DL}} + \frac{R}{(1 + RQ(i\omega))^{\beta}} + R_0 + i\omega L \qquad (6.10)$$

The structures of all stacks analyzed in this section are summarized in table 6.6.

The OLEDs with the graded mixed structures are doped with the phosphorescent dye $Ir(ppy)_3$. A measurement of a pure $Ir(ppy)_3$ layer not shown here yielded a dielectric constant of about 3.2. Thus, the implementation of the phoshpor at low weight percentage will not change the dielectric constant of the mixed layer severly. For the conductivity however, it has been reported that the HOMO states of $Ir(ppy)_3$ act as traps for charge carriers in TCTA doped devices lowering the mobility by 1-2 orders of magnitude [132]. Thus, the phosphpor could have strong effects on the intrinsic charge carrier density respectively mobility in the mixed regions. This will be examined for the GMH devices.

Stack GM35

To exclude effects, which could be introduced by the phosphorescent dye $Ir(ppy)_3$, devices with a 35 nm thick graded intermixed region of TCTA and TPBI without MoO_3 and Ca were prepared. In figure 6.11 the conductance and capacitance spectra of all GM35 devices is shown. At first sight it is difficult to observe a two layer behaviour for the conductance. The capacitance however exhibits a strong increase at low frequencies, which possibly can be attributed to a multilayer behaviour. To
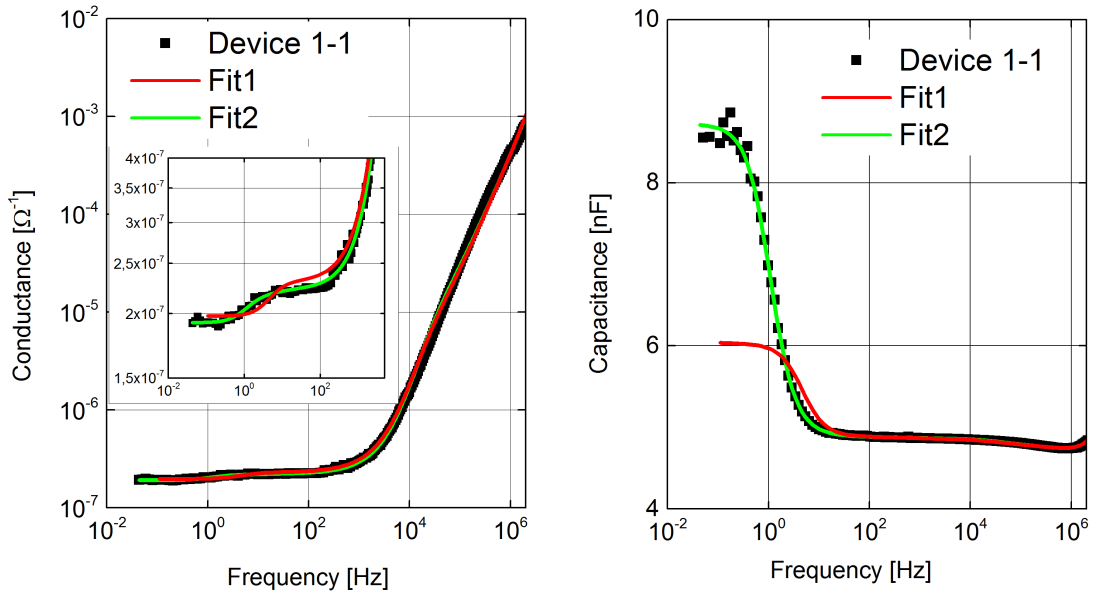
Figure 6.12: Conductance and Capacitance of device 1-1 of the GM35 stack and the corresponding fits with equations 6.9 and 6.10.

examine the conductance in more detail, the spectra of device 2-1 and the two fits with equations 6.9 and 6.10 are presented in figure 6.11. The inset is a zoom in into the region at low frequencies. Here, the two plateaus of the conductance can be identified. For high frequencies, both fits yield reasonable results: The total capacitance of a multilayer device is independent of the resistance of the layers and the behaviour of the conductance is mainly defined by σ_{AC}, which is similar for both layers. At low frequencies however, Fit 1 and Fit 2 are deviating. Fit 1 cannot describe the steep increase of the capacitance as well as the characterics of the two plateus very good, whereas Fit 2 yields a good description over the whole frequency range. In fact, Fit 1 did not even converge for two of the four devices. Thats why in table 6.7 only the averaged results of Fit 2 are presented. Furthermore the values estimated from the measurements with the microbalances are included, where an error of 10 % was assumed. The parameter values of the CPE-element are also included, but as it influenced the spectrum only at high frequencies it will not be further discussed for the following stacks. Because of the variations of the DC-conductivities from device to device, no error for σ_{DC} is specified.

The total layer thickness is predicted very well by the fit. In the intermixed zone, the fit yields a decreased conductivity compared to that of the pure layers, as can be seen by looking at the value of $\sigma_{\mathrm{DC,mix2}}$, which is about one order of
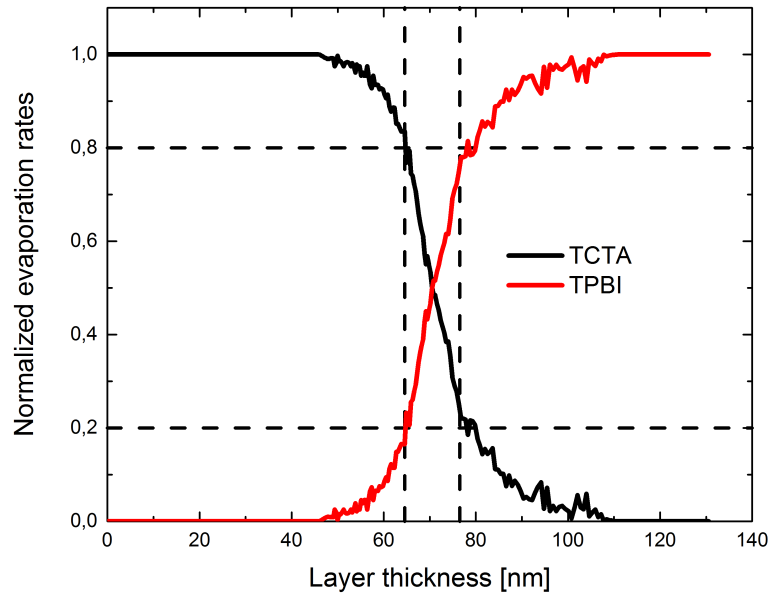
Figure 6.13: Normalized evaporation rates of the GM35 stack and an illustration of the width of the zone which was identified as intermixed by the fit.

magnitude lower than that of the pure layers. The result for the TCTA layer thickness of $d_{\mathrm{TCTA}} = (50 \pm 5)\,\mathrm{nm}$ is very good. The result for the transition width is $h = (12 \pm 12)\,\mathrm{nm}$ and thus, the TPBI layer thickness is slightly overestimated. The real transition width is underestimated by about 66%. However, this can be understood by looking at figure 6.13, where the normalized evaporation rates of the GM20 stack are shown. Here, the dotted black lines illustrate the region which is identified as intermixed by the fit. It is not unrealistic, that the overall mobility does not change abrubtly at the edges of the intermixed layers. When the concentration of the respective molecules are lowered, there are fewer and fewer paths for both, electrons and holes so that the overall mobility can be expected to be lowered in the intermixed region. Such a decrease in the overall mobility in an intermixed region was for example reported for intermixed layers of NPD and Alq3 [124].

Stack GMH30

In figure 6.14 the conductance and capacitance spectra of all GMH30 devices are shown. The conductance values at low frequencies are scattered somewhat, similar to these of the TCTA 1 stack. The capacitance exhibits similar characteristics for all devices and a multilayer behaviour with two plateus can be identified. In figure 6.15 the data of device 2-1 and the two fits are depicted. Both fits can describe the impedance spectrum very well. In fact, both fits lie more or less on top of each other.

This was found for all devices of this stack, so that it is more meaningful to directly compare the averaged fitting results. They are summarized in table 6.8. For the conductivites no error is specified, because of the varying values between the devices at low frequencies. Looking at the values, Fit2 seems to estimate more reasonable results. Fit 1 underestimates the transition width to be $h = (9.4 \pm 5.0)\,\mathrm{nm}$, while Fit 2 gives a value of $h = (22 \pm 8)\,\mathrm{nm}$. Furthermore, the layer thickness of TCTA is modelled better by Fit 2. Thus, both fits were able to identify an intermixing, with Fit 2 yielding more realistic results.

Stack GMH45

Same as seen for the devices of the GMH30 stack, the spectra of the devices of the GMH45 stack all exhibit a similar behaviour for the capacitance and slightly varying conductances at low frequencies. In figure 6.16 the conductance and capacitance spectra of a characteristic device and the corresponding fits are depicted. Again, both fit functions can describe the spectra over the whole frequency range very well. Fit2 even can account for the slight additional increase of the capacitance at very low frequencies.

The averaged results of both fits are shown in table 6.9. Again, the total layer thickness is very well predicted by both fit functions. However, while Fit1 predicts an intermixed zone of $h_{\mathrm{Fit1}} = (9.4 \pm 5.0)\,\mathrm{nm}$, the result of Fit2 is $h_{\mathrm{Fit2}} = (58.5 \pm 2.8)\,\mathrm{nm}$. The difference lies in the conductivites: Fit1 only has two free parameters for the

Table 6.7: Averaged results of the two fits for all GM35 devices.

Parameter	Fit2	Microbalances
$\sigma_{\mathrm{DC,TCTA}}$ in $\frac{1}{\Omega\,\mathrm{m}}$	$7.1 \cdot 10^{-10}$	
$\sigma_{\mathrm{DC,TPBI}}$ in $\frac{1}{\Omega\,\mathrm{m}}$	$8.5 \cdot 10^{-10}$	
$\sigma'_{\mathrm{DC,mix1}}$ in $\frac{1}{\Omega\,\mathrm{m}}$	$1.1 \cdot 10^{-9}$	
$\sigma'_{\mathrm{DC,mix2}}$ in $\frac{1}{\Omega\,\mathrm{m}}$	$1.4 \cdot 10^{-10}$	
d_{tot} in nm	130 ± 2	130 ± 13
d_{TCTA} in nm	50 ± 7	50 ± 5
h in nm	12 ± 2	35 ± 5
R_{Q} in Ω	7 ± 3	
Q	$(4.0 \pm 0.7) \cdot 10^{-8}$	
β	0.74 ± 0.02	
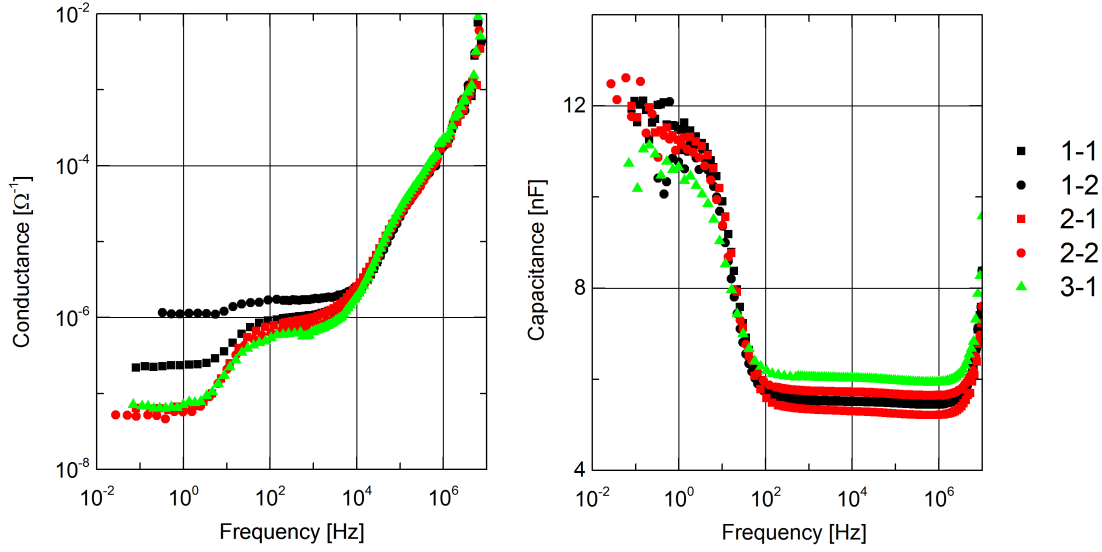
Figure 6.14: Conductance and Capacitance of all GMH30 devices.

conductivy and therefore must attribute the low conductivity found in the spectra at low frequencies to either the TCTA or TPBI layer. On the contrary, Fit2 fully attributes the low conductivity to the intermixed region and yields similar conductivities for the TCTA and TPBI layers as was also found for the single materials. The effect of a lowered mobility by introducing a dopant has been described above and could explain these fit results [132]. One reason for the fact that Fit2 even

Table 6.8: Averaged results of the two fits for all GMH30 devices.

Parameter	Fit1	Fit2	Microbalances
$\sigma_{\mathrm{DC,TCTA}}$ in $\frac{1}{\Omega\,\mathrm{m}}$	$5.7 \cdot 10^{-9}$	$5.7 \cdot 10^{-9}$	
$\sigma_{\mathrm{DC,TPBI}}$ in $\frac{1}{\Omega\,\mathrm{m}}$	$1.9 \cdot 10^{-10}$	$1.7 \cdot 10^{-9}$	
$\sigma'_{\mathrm{DC,mix1}}$ in $\frac{1}{\Omega\,\mathrm{m}}$		$2.1 \cdot 10^{-9}$	
$\sigma'_{\mathrm{DC,mix2}}$ in $\frac{1}{\Omega\,\mathrm{m}}$		$3.6 \cdot 10^{-10}$	
d_{tot} in nm	114 ± 4	112 ± 5	110 ± 11
d_{TCTA} in nm	35.8 ± 13.0	44 ± 11	50 ± 5
h in nm	9.4 ± 5.0	22 ± 8	30 ± 3
R_{Q} in Ω	3.5 ± 1.5		
Q	$(8.5 \pm 2.1) \cdot 10^{-7}$		
p	0.8 ± 0.1		
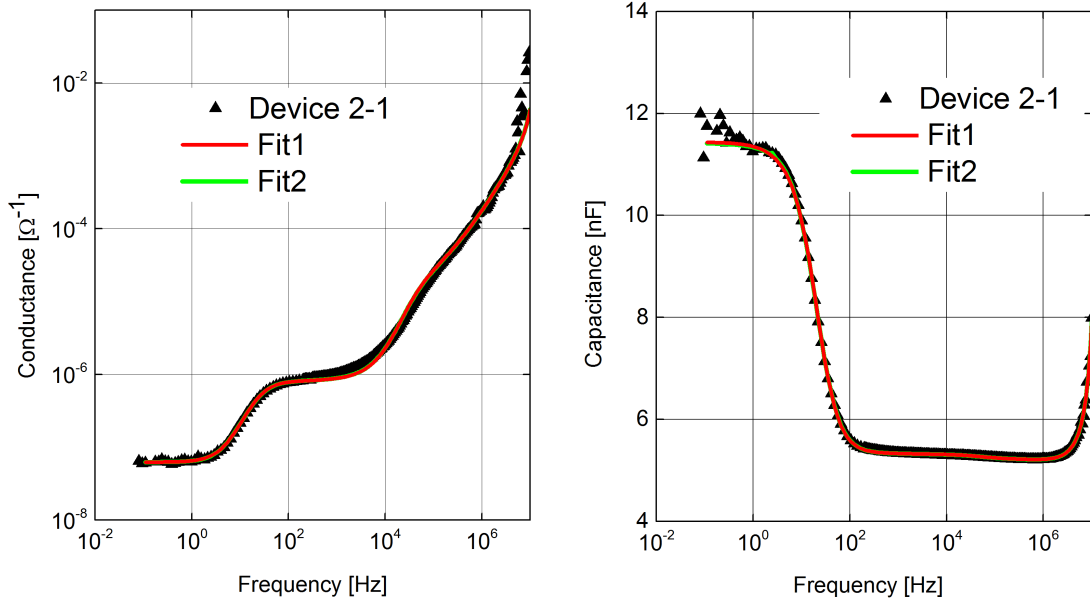
Figure 6.15: Conductance and Capacitance of device 2-1 and the corresponding fits.

overestimates the transition width might be attributed to a slightly higher dielectric constant in the mixed layer which would lead to an overestimation of the layer thickness. However, same as for the GMH30, the total layer thickness is quite well predicted by both fits, so it can be expected that the fixed material parameters for TCTA and TPBI are consistent.

Table 6.9: Averaged results of the two fits for seven GMH45 devices.

Parameter	Fit1 (7 devices)	Fit2	Microbalances
$\sigma_{\mathrm{DC,TCTA}}$ in $\frac{1}{\Omega\,\mathrm{m}}$	$3.5 \cdot 10^{-8}$	$3.9 \cdot 10^{-8}$	
$\sigma_{\mathrm{DC,TPBI}}$ in $\frac{1}{\Omega\,\mathrm{m}}$	$5 \cdot 10^{-10}$	$2.5 \cdot 10^{-8}$	
$\sigma'_{\mathrm{DC,mix1}}$ in $\frac{1}{\Omega\,\mathrm{m}}$		$4.5 \cdot 10^{-10}$	
$\sigma'_{\mathrm{DC,mix2}}$ in $\frac{1}{\Omega\,\mathrm{m}}$		$5.1 \cdot 10^{-10}$	
d_{tot} innm	122.6 ± 3.6	120.8 ± 3.6	125 ± 12
d_{TCTA} innm	50 ± 2	39 ± 9	50 ± 5
h innm	9.4 ± 5.0	58.5 ± 2.8	45 ± 5
R_{Q} in Ω	56 ± 13		
Q	$(3.6 \pm 1.4) \cdot 10^{-8}$		
p	0.86 ± 0.04		
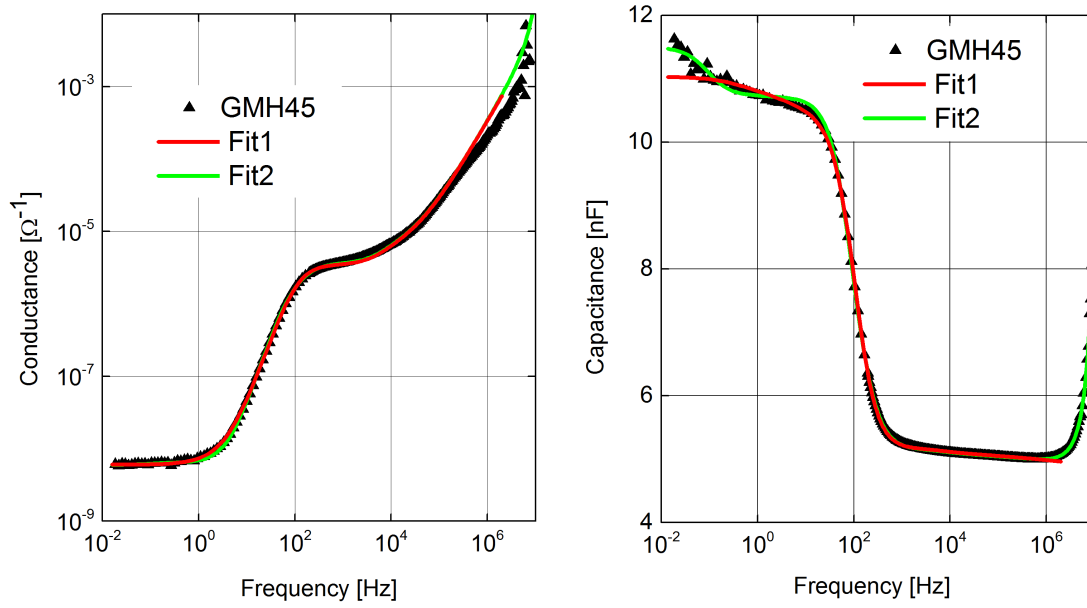
Figure 6.16: Conductance and Capacitance of a characteristic GMH45 device and the corresponding fits.

Stack GMH70

The spectra of a characteristic GMH70 device and the two fits are shown in figure 6.17. Again, both fits describe the general shape of the spectrum nicely and Fit2 can again even account for the additional increase of the capacitance at very low frequencies. The averaged results of both fits are presented in table 6.10. The results very much resemble these of the GMH45: Fit1 attributes the low conductance found at low frequency to the TPBI layer, whereas Fit2 fully attributes it to the doped region and yields a similar conductivity for the TPBI and TCTA layers. Fit1 again strongly underestimates the intermixing and yields a width of the intermixed zone of $h_{\mathrm{Fit1}} = (12 \pm 8)\,\mathrm{nm}$, while Fit2 predicts the real transition width very good: $h_{\mathrm{Fit2}} = (69 \pm 15)\,\mathrm{nm}$. The total layer thickness is underestimated by about 10%, but this is still in the error range of the microbalances.

6.2.1   Conclusion

Four different structures with graded intermixed structures have been analyzed. For the undoped GM35 stack, an intermixing of $h = (12 \pm 2)\,\mathrm{nm}$ was found with the fit function defined by equation 6.10. It was able to account for a decrease of the conductivity of the intermixed layer and the resulting steep increase of the capacitance at low frequencies which could not be described by the other fit function. The real
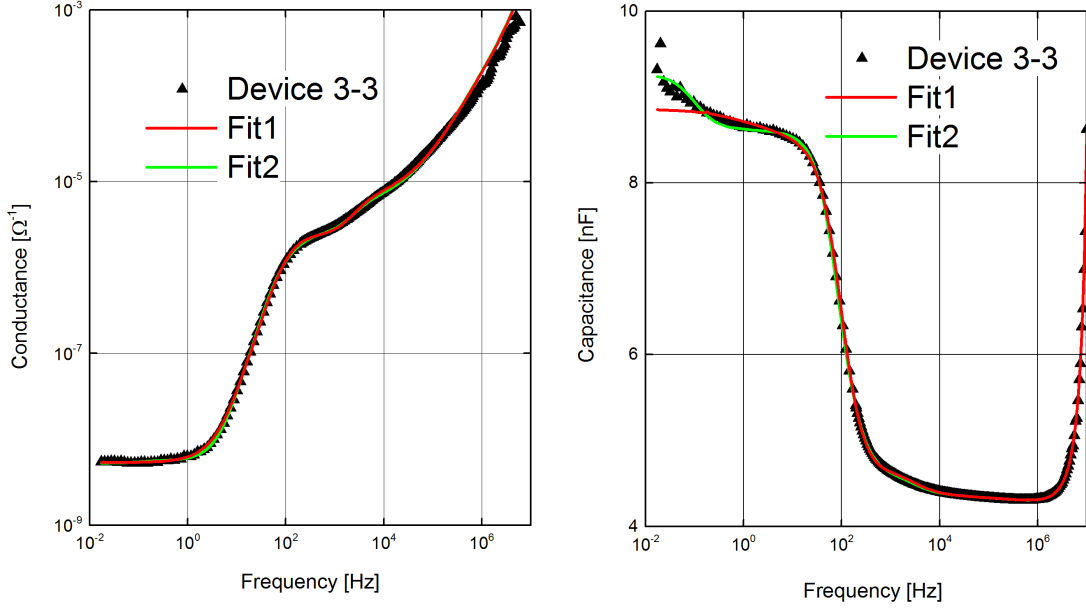
Figure 6.17: Conductance and Capacitance of a characteristic GMH70 device and the corresponding fits.

transition width is underestimated by about 66%. By assuming that the mobility only noticeably changes for a certain mixing ratio of both molecules, this is a reason-

Table 6.10: Averaged results of the two fits for eleven GMH70 devices.

Parameter	Fit1	Fit2	Microbalances
R_0	150		
$\sigma_{\text{DC,TCTA}}$ in $\frac{1}{\Omega\,\text{m}}$	$3.1 \cdot 10^{-8}$	$3.7 \cdot 10^{-8}$	
$\sigma_{\text{DC,TPBI}}$ in $\frac{1}{\Omega\,\text{m}}$	$4 \cdot 10^{-10}$	$2.7 \cdot 10^{-8}$	
$\sigma'_{\text{DC,mix1}}$ in $\frac{1}{\Omega\,\text{m}}$		$7.4 \cdot 10^{-10}$	
$\sigma'_{\text{DC,mix2}}$ in $\frac{1}{\Omega\,\text{m}}$		$1 \cdot 10^{-10}$	
d_{tot} in nm	$(140 \pm 5)\,\text{nm}$	$(136 \pm 5)\,\text{nm}$	$(150 \pm 15)\,\text{nm}$
d_{TCTA} in nm	$(52 \pm 4)\,\text{nm}$	$(42 \pm 11)\,\text{nm}$	$(50 \pm 5)\,\text{nm}$
h in nm	$(12 \pm 8)\,\text{nm}$	$(69 \pm 15)\,\text{nm}$	$(70 \pm 7)\,\text{nm}$
R_{Q} in Ω	659 ± 92		
Q	$(8.4 \pm 0.9) \cdot 10^{-8}$		
p	0.95 ± 0.01		

able result [124]. Furthermore, the fit function can possibly be improved to account for this effect.

For the OLEDs incorporating the phosphorescent dye Ir(ppy)$_3$ in the graded mixed structure, Fit1 underestimated the width of the transition zone for all three stacks, while Fit2 attributed the low conductance found in these devices to the intermixed zone [132] and yielded reasonable values for the transition width for all examined stacks.

In conclusion it has been shown, that the newly introduced fit function was able to identify the intermixed layers for all presented structured and gave reasonable values for the transition width h. In these intermixed layers, the fit modelled the conductivity to be different from the ideal behaviour for pure layers. If similar effects on the conductivity are also present for intermixed layers which result from a printing process, impedance spectroscopy can be a suitable tool for the identifying of these layers. In the future, more layers without dopant in the mixed region should be analzyed to verify the results for the GM35 stack presented here and furthermore printed layers should be analyzed.

7. Summary and Outlook

In the first part of this thesis, phosphorescent OLEDs with mixed host structures in the light emitting layer have been examined. For that purpose a simple OLED stack, consisting of MoO_3 as a hole injection layer (HIL), TCTA as a hole transport layer (HTL) and TPBI as an electron transporting layer (ETL) was introduced. The basic structure of these three layers was fixed for all devices. Different approaches for the emitting layer have been examined: Devices with a conventional heterostructure, a uniformly mixed host structure with a mixing ratio of TPBI:TCTA (63:30) and three graded mixed host structures with thicknesses of 30 nm, 45 nm and 70 nm were prepared by thermal vacuum evaporation and compared to each other in detail. The emitting layer was doped with 7% of the phosphorescent dye $Ir(ppy)_3$. The PHOLEDs with a 70 nm broad graded emitting layer show the best perfomance with a maximum power efficiency and external quantum efficiency of 48.2 lm W and 16.4% respectively. Compared to the efficiencies of the heterostructure, that corresponds to an improvement of about 50 %. Furthermore the graded OLEDs with a 45 nm and 30 nm broad emitting layer show a reduced efficiency roll-off at high current densities. The critical current density for which the efficiency drops to 90 % of its initial value is three times higher compared to that of the heterostructure and the uniformly mixed host devices. Furthermore, lifetime measurements were performed which allowed for an extrapolation of the lifetimes to lower luminance levels. For an initial luminance of 100 $\frac{cd}{m^2}$ the PHOLEDs with a 70 nm graded emission layer yield a lifetime improvement of 29 % compared to that of the heterostructure devices. These effects are attributed to a broadened emission zone and an improved charge balance of the OLEDs with a graded mixed host structure. Further support for that assumption comes from measurements of the emission spectra of the devices. The spectra of the OLEDs with a graded structure show a slight red shift with increasing current density, while there was no change of the spectra for the heterostructure devices. This effect is explained by assuming a shift of the recombination zone inside the emitting layer with the conclusion that the recombination zone in the graded structure is not resticted to one of the interfaces.

The devices with a uniformly mixed host shows a slightly improved quantum efficiency compared to the heterostucture devices. However, the observed efficiency roll-off is not reduced. Most probably the mixing ratio of 63:30 of TPBI:TCTA

can be further fine-tuned to yield a better charge transport also for higher current densities. In conclusion, the OLEDs with a graded structure in the light emitting layer have shown to bear the potential for an increased quantum efficiency, a reduced efficiency roll-off behaviour and a longer lifetime. By fine tuning the structure of the stacks examined in this thesis, e.g. by reducing the layer thicknesses of the HTL and using a lower doping concentration, it is expected that the characteristics of the graded structure can be even further improved.

In the second part of this thesis, impedance spectroscopy was tested as a tool to detect intermixing in OLEDs with graded mixed structures. Single layers of pure TCTA and TPBI were prepared to characterize the materials. Their conductivities are found to be scattered over about one order of magnitude. A better control over the fabrication process, especially a better vacuum in the evaporation chambers probably can resolve this issue. It was possible to describe the frequency dependence of the material's conductivity and dielectric constant by applying the UDR-theory of Jonscher. The dielectric constants of TCTA and TPBI are estimated to be 2.7 respectively 3.2 at a frequency of 1000Hz. One uniformly mixed device was examined to estimate the material parameters in the mixed device. The parameters are found to be somewhere in between the values for the pure materials. Using a constant-phase-element in parallel with a resistor it was possible to model the observed impedance of pure MoO_3 layers. The influence of MoO_3 and the contacting layers on the measured impedance spectra for devices of multiple layers were described by introducing such a CPE-element in the equivalent circuit.

Finally, impedance spectroscopy was used to identify the degree of intermixing in four different graded devices. A new fit function was introduced which allowed for modelling a non-steady change of the conductance in the intermixed region. This fit function is able to identify the width of the intermixed region for all devices analyzed in this thesis quite well. Improving this fit function even further, it can be expected that impedance spectroscopy can be used as a tool for the detection of intermixing in solution processed devices. Executing impedance measurements for solution processed layers can be a next step to achieve this goal.

Bibliography

[1] C. W. Tang and S. a. VanSlyke, "Organic electroluminescent diodes," *Applied Physics Letters*, vol. 51, no. 12, p. 913, 1987.

[2] M. A. Baldo and S. R. Forrest, "Highly efficient phosphorescent emission from organic electroluminescent devices," vol. 395, no. September, pp. 151–154, 1998.

[3] C. Murawski, K. Leo, and M. C. Gather, "Efficiency Roll-Off in Organic Light-Emitting Diodes.," *Advanced materials (Deerfield Beach, Fla.)*, pp. 1–27, Sept. 2013.

[4] M. C. Gather, A. Koehnen, and K. Meerholz, "White organic light-emitting diodes.," *Advanced materials (Deerfield Beach, Fla.)*, vol. 23, pp. 233–48, Jan. 2011.

[5] C. Gaertner, C. Karnutsch, C. Pflumm, and U. Lemmer, "Numerical Device Simulation of Double- Heterostructure Organic Laser Diodes Including Current-Induced Absorption Processes," *IEEE Journal of Selected Topics in Quantum Electronics*, vol. 43, no. 11, pp. 1006–1017, 2007.

[6] R. Meerheim, S. Scholz, S. Olthof, G. Schwartz, S. Reineke, K. Walzer, and K. Leo, "Influence of charge balance and exciton distribution on efficiency and lifetime of phosphorescent organic light-emitting devices," *Journal of Applied Physics*, vol. 104, no. 1, p. 014510, 2008.

[7] S. Lee, C. W. Tang, and L. J. Rothberg, "Effects of mixed host spatial distribution on the efficiency of blue phosphorescent organic light-emitting diodes," *Applied Physics Letters*, vol. 101, no. 4, p. 043303, 2012.

[8] M. E. Kondakova, T. D. Pawlik, R. H. Young, D. J. Giesen, D. Y. Kondakov, C. T. Brown, J. C. Deaton, J. R. Lenhard, and K. P. Klubek, "High-efficiency, low-voltage phosphorescent organic light-emitting diode devices with mixed host," *Journal of Applied Physics*, vol. 104, no. 9, p. 094501, 2008.

[9] C.-c. Lee, C.-h. Yuan, S.-w. Liu, L.-a. Liu, and Y.-s. Chen, "Solution-Processed Electrophosphorescent Devices Based on Small-Molecule Mixed Hosts," *Journal of Display Technology*, vol. 7, pp. 636–639, Dec. 2011.

[10] D. Wang, Z. Wu, X. Zhang, B. Jiao, S. Liang, D. Wang, R. He, and X. Hou, "Solution-processed organic films of multiple small-molecules and white light-emitting diodes," *Organic Electronics*, vol. 11, pp. 641–648, Apr. 2010.

[11] H. H. Fong, J.-K. Lee, Y.-F. Lim, A. a. Zakhidov, W. W. H. Wong, A. B. Holmes, C. K. Ober, and G. G. Malliaras, "Orthogonal processing and patterning enabled by highly fluorinated light-emitting polymers.," *Advanced materials (Deerfield Beach, Fla.)*, vol. 23, pp. 735–9, Mar. 2011.

[12] C. a. Zuniga, S. Barlow, and S. R. Marder, "Approaches to Solution-Processed Multilayer Organic Light-Emitting Diodes Based on Cross-Linking †," *Chemistry of Materials*, vol. 23, pp. 658–681, Feb. 2011.

[13] M. Lekstrom, M. a. McLachlan, S. Husain, D. W. McComb, and B. a. Shollock, "Using the in situ lift-out technique to prepare TEM specimens on a single-beam FIB instrument," *Journal of Physics: Conference Series*, vol. 126, p. 012028, Aug. 2008.

[14] J. B. Gilbert, M. F. Rubner, and R. E. Cohen, "Depth-profiling X-ray photo-electron spectroscopy (XPS) analysis of interlayer diffusion in polyelectrolyte multilayers.," *Proceedings of the National Academy of Sciences of the United States of America*, vol. 110, pp. 6651–6, Apr. 2013.

[15] R. Tone, *Impedance Spectroscopy as a Tool for the Detection of Mixed Layers in Organic Devices.* PhD thesis, 2013.

[16] J. Meyer, S. Hamwi, T. Buelow, H.-H. Johannes, T. Riedl, and W. Kowalsky, "Highly efficient simplified organic light emitting diodes," *Applied Physics Letters*, vol. 91, no. 11, p. 113506, 2007.

[17] M. Schwoerer and H. C. Wolf, *Organic molecular solids.* Physics textbook, Weinheim: Wiley-VCH, 2007.

[18] W. H. Brütting, ed., *Physics of organic semiconductors.* Weinheim: Wiley-VCH, 2. compl. ed., 2012.

[19] M. Schwarze, *Photoelektronenspektroskopie am lösungsprozessierten Donor-Akzeptor-System P3HT:PCBM.* Master thesis, University Heidelberg, 2012.

[20] Wikipedia, "Orbital hybridisation sp3." http://en.wikipedia.org/wiki/File:AE4h.svg [Online; accessed 01-September-2013], 2013.

[21] Wikipedia, "Orbital hybridisation sp2." http://en.wikipedia.org/wiki/File:AE3h.svg [Online; accessed 01-September-2013], 2013.

[22] Wikipedia, "Representation of benzene." http://en.wikipedia.org/wiki/File:Benzene_Representations.svg [Online; accessed 01-September-2013], 2013.

[23] S. Stolz, *Photoelektronenspektroskopie an organischen Charge-Transfer-Komplexen.* Diploma thesis, University Heidelberg, 2012.

[24] I. Vladimirov, *Entwicklung eines Nahfeld-Rastersondenmikroskops auf Grundlage Organischer Leuchtdioden.* Diploma thesis, Universität Heidelberg, 2011.

[25] H. Baessler, "Charge Transport in Disordered Organic Photoconductors," *Physica Status Solidi (B)*, vol. 15, no. 1, pp. 15–56, 1993.

[26] W. F. Pasveer, J. Cottaar, C. Tanase, R. Coehoorn, P. a. Bobbert, P. W. M. Blom, D. M. de Leeuw, and M. a. J. Michels, "Unified description of charge-carrier mobilities in disordered semiconducting polymers.," *Physical review letters*, vol. 94, p. 206601, May 2005.

[27] M. Bouhassoune, S. V. Mensfoort, P. Bobbert, and R. Coehoorn, "Carrier-density and field-dependent charge-carrier mobility in organic semiconductors with correlated Gaussian disorder," *Organic Electronics*, vol. 10, pp. 437–445, May 2009.

[28] Y. Yimer, P. Bobbert, and R. Coehoorn, "Charge transport in disordered organic host–guest systems: Effects of carrier density and electric field," *Synthetic Metals*, vol. 159, pp. 2399–2401, Nov. 2009.

[29] R. Coehoorn, W. Pasveer, P. Bobbert, and M. Michels, "Charge-carrier concentration dependence of the hopping mobility in organic materials with Gaussian disorder," *Physical Review B*, vol. 72, p. 155206, Oct. 2005.

[30] L. Wang, H. Zhang, X. Tang, C. Mu, and J. Li, "An improved unified description of charge-carrier mobilities in disordered organic semiconductors," *Current Applied Physics*, vol. 10, pp. 1182–1187, July 2010.

[31] H. Baessler, "Injection , Transport and Recombination of Charge Carriers in Organic Light- emitting Diodes," *Polymers for Advanced Technologies*, vol. 9, pp. 402–418, 1998.

[32] W. Brütting, "Charge carrier injection and transport in organic electronic devices," in *Organic Electronics: Emerging Applications*, 2007.

[33] R. H. Fowler and L. Nordheim, "Electron Emission in Intense Electric Fields," *Proceedings of the Royal Society A: Mathematical, Physical and Engineering Sciences*, vol. 119, pp. 173–181, May 1928.

[34] P. N. Murgatroyd, "Theory of space-charge-limited current enhanced by Frenkel effect," *Journal of Physics D: Applied Physics*, vol. 3, no. 2, p. 151, 1970.

[35] P. Blom and M. De Jong, "Electrical characterization of polymer light-emitting diodes," *IEEE Journal of Selected Topics in Quantum Electronics*, vol. 4, no. 1, pp. 105–112, 1998.

[36] V. I. Arkhipov, E. V. Emelianova, Y. H. Tak, and H. Baessler, "Charge injection into light-emitting diodes: Theory and experiment," *Journal of Applied Physics*, vol. 84, no. 2, p. 848, 1998.

[37] M. Baldo and S. Forrest, "Interface-limited injection in amorphous organic semiconductors," *Physical Review B*, vol. 64, p. 085201, Aug. 2001.

[38] "The Photochemistry Portal." http://photochemistryportal.net/home/wp-content/uploads/2009/08/jablonski.png [Online; accessed 02-September-2013].

[39] T. Forster, "10th Spiers Memorial Lecture. Transfer mechanisms of electronic excitation," *Discuss. Faraday Soc.*, vol. 27, no. 0, pp. 7–17, 1959.

[40] D. L. Dexter, "A Theory of Sensitized Luminescence in Solids," *The Journal of Chemical Physics*, vol. 21, no. 5, p. 836, 1953.

[41] M. a. Baldo and S. R. Forrest, "Transient analysis of organic electrophospho-rescence - 1- Transient analysis of triplet energy transfer," *Physical Review B*, vol. 62, pp. 10958–10966, Oct. 2000.

[42] M. Samiullah, D. Moghe, U. Scherf, and S. Guha, "Diffusion length of triplet excitons in organic semiconductors," *Physical Review B*, vol. 82, pp. 1–6, Nov. 2010.

[43] M. Segal, M. Baldo, R. Holmes, S. Forrest, and Z. Soos, "Excitonic singlet-triplet ratios in molecular and polymeric organic materials," *Physical Review B*, vol. 68, p. 075211, Aug. 2003.

[44] W. Helfrich and W. G. Schneider, "Recombination Radiation in Anthracene Crystals," *Phys. Rev. Lett.*, vol. 14, pp. 229–231, Feb. 1965.

[45] F. So, J. Kido, and P. Burrows, "Organic Light-Emitting Devices for Solid-State Lighting," *MRS Bulletin*, vol. 33, pp. 663–669, Jan. 2008.

[46] L. Xiao, Z. Chen, B. Qu, J. Luo, S. Kong, Q. Gong, and J. Kido, "Recent pro-gresses on materials for electrophosphorescent organic light-emitting devices.," *Advanced materials (Deerfield Beach, Fla.)*, vol. 23, pp. 926–52, Mar. 2011.

[47] T. A. S. Hameed, P. Predeep, and M. R. Baiju, "Organic Light Emitting Diodes : Device Physics and Effect of Ambience on Performance Parameters," in *Op-toelectronics - Devices and Applications*, pp. 1–23, 2011.

[48] L. Hung and C. Chen, "Recent progress of molecular organic electroluminescent materials and devices," *Materials Science and Engineering: R: Reports*, vol. 39, pp. 143–222, Dec. 2002.

[49] S. Kappaun, C. Slugovc, and E. J. List, "Phosphorescent organic light-emitting devices: working principle and iridium based emitter materials.," *International journal of molecular sciences*, vol. 9, pp. 1527–47, Aug. 2008.

[50] M. A. Baldo, M. E. Thompson, and S. R. Forrest, "Excitonic singlet-triplet ratio in a semiconducting organic thin film," *Physical Review B*, vol. 60, no. 20, pp. 422–428, 1999.

[51] Y. Cao, I. Parker, G. Yu, C. Zhang, and A. Heeger, "Improved quantum effi-ciency for electroluminescence in semiconducting polymers," *Nature*, vol. 397, no. February, pp. 414–417, 1999.

[52] M. Wohlgenannt, K. Tandon, S. Mazumdar, S. Ramasesha, and Z. V. Vardeny, "Formation cross-sections of singlet and triplet excitons in pi-conjugated polymers.," *Nature*, vol. 409, pp. 494–7, Jan. 2001.

[53] Y. Kawamura, K. Goushi, J. Brooks, J. J. Brown, H. Sasabe, and C. Adachi, "100% phosphorescence quantum efficiency of Ir(III) complexes in organic semiconductor films," *Applied Physics Letters*, vol. 86, no. 7, p. 071104, 2005.

[54] C. Adachi, M. a. Baldo, M. E. Thompson, and S. R. Forrest, "Nearly 100% internal phosphorescence efficiency in an organic light-emitting device," *Journal of Applied Physics*, vol. 90, no. 10, p. 5048, 2001.

[55] B. Diouf, W. S. Jeon, R. Pode, and J. H. Kwon, "Efficiency Control in Iridium Complex-Based Phosphorescent Light-Emitting Diodes," *Advances in Materials Science and Engineering*, vol. 2012, no. Figure 1, pp. 1–14, 2012.

[56] W. R. MacCluney, *Introduction to radiometry and photometry.* The Artech house optoelectronics library, Boston [u.a.]: Artech House, 1994.

[57] K. Saxena, V. Jain, and D. S. Mehta, "A review on the light extraction techniques in organic electroluminescent devices," *Optical Materials*, vol. 32, pp. 221–233, Nov. 2009.

[58] W. Brütting, J. Frischeisen, T. D. Schmidt, B. J. Scholz, and C. Mayr, "Device efficiency of organic light-emitting diodes: Progress by improved light outcoupling," *Physica Status Solidi (a)*, vol. 210, pp. 44–65, Jan. 2013.

[59] Y. Tao, C. Yang, and J. Qin, "Organic host materials for phosphorescent organic light-emitting diodes.," *Chemical Society reviews*, vol. 40, pp. 2943–70, May 2011.

[60] M. Shukla, N. Brahme, R. S. Kher, and M. S. K. Khokhar, "Elementary approach to calculate quantum efficiency of polymer light emitting diodes," vol. 49, no. February, pp. 142–145, 2011.

[61] J. Kalinowski, W. Stampor, J. Mezyk, M. Cocchi, D. Virgili, V. Fattori, and P. Di Marco, "Quenching effects in organic electrophosphorescence," *Physical Review B*, vol. 66, p. 235321, Dec. 2002.

[62] E. B. Namdas, A. Ruseckas, I. D. W. Samuel, S.-C. Lo, and P. L. Burn, "Triplet exciton diffusion in fac-tris(2-phenylpyridine) iridium(III)-cored electroluminescent dendrimers," *Applied Physics Letters*, vol. 86, no. 9, p. 091104, 2005.

[63] M. Baldo, C. Adachi, and S. Forrest, "Transient analysis of organic electrophos-phorescence -2- Transient analysis of triplet-triplet annihilation," *Physical Review B*, vol. 62, pp. 10967–10977, Oct. 2000.

[64] S. Reineke, K. Walzer, and K. Leo, "Triplet-exciton quenching in organic phos-phorescent light-emitting diodes with Ir-based emitters," *Physical Review B*, vol. 75, pp. 1–13, Mar. 2007.

[65] H. Aziz and Z. D. Popovic, "Degradation Phenomena in Small-Molecule Or-ganic Light-Emitting Devices," *Chemistry of Materials*, vol. 16, pp. 4522–4532, Nov. 2004.

[66] M. Jahnel, *Bestimmung charakteristischer Parameter zur Vorhersage von Frühausfällen bei großflächigen organischen Leuchtdioden (OLED)*. PhD the-sis, Fachhochschule Lausitz, 2008.

[67] R. Seifert, I. Rabelo de Moraes, S. Scholz, M. C. Gather, B. Luessem, and K. Leo, "Chemical degradation mechanisms of highly efficient blue phospho-rescent emitters used for organic light emitting diodes," *Organic Electronics*, vol. 14, pp. 115–123, Jan. 2013.

[68] T. Glaser, *Infrarotspektroskopie und Photolumineszenzmessungen an Emitter-schichten für organische Leuchtdioden*. PhD thesis, 2009.

[69] G. Vamvounis, H. Aziz, N.-X. Hu, and Z. D. Popovic, "Temperature depen-dence of operational stability of organic light emitting diodes based on mixed emitter layers," *Synthetic Metals*, vol. 143, pp. 69–73, May 2004.

[70] K. Fehse, R. Meerheim, K. Walzer, K. Leo, W. Loevenich, and A. Elschner, "Lifetime of organic light emitting diodes on polymer anodes," *Applied Physics Letters*, vol. 93, no. 8, p. 083303, 2008.

[71] C. Fery, B. Racine, D. Vaufrey, H. Doyeux, and S. Cina, "Physical mechanism responsible for the stretched exponential decay behavior of aging organic light-emitting diodes," *Applied Physics Letters*, vol. 87, no. 21, p. 213502, 2005.

[72] L. Duan, D. Zhang, K. Wu, X. Huang, L. Wang, and Y. Qiu, "Controlling the Recombination Zone of White Organic Light-Emitting Diodes with Extremely Long Lifetimes," *Advanced Functional Materials*, vol. 21, pp. 3540–3545, Sept. 2011.

[73] W. E. Howard and O. F. Prache, "Microdisplays based upon organic light-emitting diodes," *IBM Journal of Research and Development*, vol. 45, no. 1, pp. 115–127, 2001.

[74] R. Meerheim, K. Walzer, M. Pfeiffer, and K. Leo, "Ultrastable and efficient red organic light emitting diodes with doped transport layers," *Applied Physics Letters*, vol. 89, no. 6, p. 061111, 2006.

[75] Z. Popovic, S. Xie, N. Hu, a. Hor, D. Fork, G. Anderson, and C. Tripp, "Life extension of organic LED's by doping of a hole transport layer," *Thin Solid Films*, vol. 363, pp. 6–8, Mar. 2000.

[76] A. Chaskar, H.-F. Chen, and K.-T. Wong, "Bipolar host materials: a chemical approach for highly efficient electrophosphorescent devices.," *Advanced materials (Deerfield Beach, Fla.)*, vol. 23, pp. 3876–95, Sept. 2011.

[77] D. Ma, C. S. Lee, S. T. Lee, and L. S. Hung, "Improved efficiency by a graded emissive region in organic light-emitting diodes," *Applied Physics Letters*, vol. 80, no. 19, p. 3641, 2002.

[78] O. Young Kim, H. Jin Park, and J. Yeob Lee, "Dependence of hole and electron current density of mixed host devices on mixed host composition," *Journal of Luminescence*, vol. 138, pp. 150–152, June 2013.

[79] S. Liu, C. Huang, J. Lee, K. Yang, C. Chen, and Y. Chang, "Blue mixed host organic light emitting devices," *Thin Solid Films*, vol. 453-454, pp. 312–315, Apr. 2004.

[80] J.-H. Lee, C.-I. Wu, S.-W. Liu, C.-A. Huang, and Y. Chang, "Mixed host organic light-emitting devices with low driving voltage and long lifetime," *Applied Physics Letters*, vol. 86, no. 10, p. 103506, 2005.

[81] Y.-C. Tsai and J.-H. Jou, "Long-lifetime, high-efficiency white organic light-emitting diodes with mixed host composing double emission layers," *Applied Physics Letters*, vol. 89, no. 24, p. 243521, 2006.

[82] C.-H. Hsiao, Y.-H. Chen, T.-C. Lin, C.-C. Hsiao, and J.-H. Lee, "Recombination zone in mixed-host organic light-emitting devices," *Applied Physics Letters*, vol. 89, no. 16, p. 163511, 2006.

[83] S. H. Kim, J. Jang, K. S. Yook, and J. Y. Lee, "Stable efficiency roll-off in phosphorescent organic light-emitting diodes," *Applied Physics Letters*, vol. 92, no. 2, p. 023513, 2008.

[84] J. Lee, J.-I. Lee, J. Y. Lee, and H. Y. Chu, "Improved performance of blue phosphorescent organic light-emitting diodes with a mixed host system," *Applied Physics Letters*, vol. 95, no. 25, p. 253304, 2009.

[85] J. Lee, "Improved Performance of White Phosphorescent Organic Light-Emitting Diodes through a Mixed-Host Structure," *ETRI Journal*, vol. 31, pp. 642–646, Dec. 2009.

[86] J. Lee, J.-I. Lee, J. Y. Lee, and H. Y. Chu, "Stable efficiency roll-off in blue phosphorescent organic light-emitting diodes by host layer engineering," *Organic Electronics*, vol. 10, pp. 1529–1533, Dec. 2009.

[87] J. J. Park, S. T. Lee, T. J. Park, W. S. Jeon, J. Jang, and J. H. Kwon, "Stable Efficiency Roll-off in Solution-processed Phosphorescent Green Organic Light-emitting Diodes," *Journal of the Korean Physical Society*, vol. 55, no. 1, pp. 327–330, 2009.

[88] K. S. Yook and J. Y. Lee, "Recombination zone study of phosphorescent organic light-emitting diodes with triplet mixed host emitting structure," *Journal of Industrial and Engineering Chemistry*, vol. 16, pp. 181–184, Mar. 2010.

[89] N. Chopra, J. S. Swensen, E. Polikarpov, L. Cosimbescu, F. So, and A. B. Padmaperuma, "High efficiency and low roll-off blue phosphorescent organic light-emitting devices using mixed host architecture," *Applied Physics Letters*, vol. 97, no. 3, p. 033304, 2010.

[90] Z. Wang, S. Naka, and H. Okada, "Solution-Processed Small Molecular Organic Light-Emitting Devices with a Mixed Single Layer," *Japanese Journal of Applied Physics*, vol. 50, p. 01BC06, Jan. 2011.

[91] Z. Wang, Y. Lou, S. Naka, and H. Okada, "Direct comparison of solution- and vacuum-processed small molecular organic light-emitting devices with a mixed single layer.," *ACS applied materials and interfaces*, vol. 3, pp. 2496–503, July 2011.

[92] Y. Chen, J. Chen, Y. Zhao, and D. Ma, "High efficiency blue phosphorescent organic light-emitting diode based on blend of hole- and electron-transporting

materials as a co-host," *Applied Physics Letters*, vol. 100, no. 21, p. 213301, 2012.

[93] C. W. Seo and J. Y. Lee, "High external quantum efficiency in deep blue phosphorescent organic light emitting diodes using a simple device structure," *Thin Solid Films*, vol. 520, pp. 7022–7025, Sept. 2012.

[94] Q. Fu, J. Chen, C. Shi, and D. Ma, "Solution-processed small molecules as mixed host for highly efficient blue and white phosphorescent organic light-emitting diodes.," *ACS applied materials and interfaces*, vol. 4, pp. 6579–86, Dec. 2012.

[95] Y. J. Doh, J. S. Park, W. S. Jeon, R. Pode, and J. H. Kwon, "Soluble processed low-voltage and high efficiency blue phosphorescent organic light-emitting devices using small molecule host systems," *Organic Electronics*, vol. 13, pp. 586–592, Apr. 2012.

[96] N. C. Erickson and R. J. Holmes, "Highly efficient, single-layer organic light-emitting devices based on a graded-composition emissive layer," *Applied Physics Letters*, vol. 97, no. 8, p. 083308, 2010.

[97] S. W. Liu, X. W. Sun, and H. V. Demir, "Graded-host phosphorescent light-emitting diodes with high efficiency and reduced roll-off," *AIP Advances*, vol. 2, no. 1, p. 012192, 2012.

[98] N. C. Erickson and R. J. Holmes, "Relating charge transport and performance in single-layer graded-composition organic light-emitting devices," *Journal of Applied Physics*, vol. 110, no. 8, p. 084515, 2011.

[99] A. B. Chwang, R. C. Kwong, and J. J. Brown, "Graded mixed-layer organic light-emitting devices," *Applied Physics Letters*, vol. 80, no. 5, p. 725, 2002.

[100] W. Quirino, K. Teixeira, C. Legnani, V. Calil, B. Messer, O. V. Neto, M. Pacheco, and M. Cremona, "Improved multilayer OLED architecture using evolutionary genetic algorithm," *Thin Solid Films*, vol. 518, pp. 1382–1385, Dec. 2009.

[101] Y. Bai, M. Khan, W.-Q. Zhu, X.-Y. Jiang, and Z.-L. Zhang, "A blue organic light emitting diodes with graded junction," *Displays*, vol. 29, pp. 365–368, Oct. 2008.

[102] S. Lee and C. W. Tang, "Fabrication of a blue organic light-emitting diode with a novel thermal deposition boat," *Journal of Vacuum Science and Technology B: Microelectronics and Nanometer Structures*, vol. 29, no. 6, p. 062401, 2011.

[103] V. F. Lvovich, *Impedance spectroscopy.* Oxford [u.a.]: Wiley, 2012.

[104] A. K. Jonscher, "The Universal dielectric response and its Physical Significance," *IEE Transactions on electrical insulation*, vol. 27, No.3, no. June, 1992.

[105] J. C. Dyre, "The random free-energy barrier model for ac conduction in disordered solids," *Journal of Applied Physics*, vol. 64, no. 5, p. 2456, 1988.

[106] S. Elliot, "A . c . conduction in amorphous chalcogenide and pnictide semiconductors," *Advances in Physics*, vol. 36, no. 2, pp. 135–218, 1987.

[107] N. A. Hegab and H. M. El-mallah, "AC Conductivity and Dielectric Properties of Amorphous Te 42 As 36 Ge 10 Si 12 Glass," *ACTA Physica Polonica A*, vol. 116, no. 6, pp. 1048–1052, 2009.

[108] J. Dyre and T. Schrø der, "Universality of ac conduction in disordered solids," *Reviews of Modern Physics*, vol. 72, pp. 873–892, July 2000.

[109] P. D'Angelo, *Dynamic measurements for the electrical characterization of organic materials and related devices.* PhD thesis, 2009.

[110] V. Bobnar, P. Lunkenheimer, J. Hemberger, a. Loidl, F. Lichtenberg, and J. Mannhart, "Dielectric properties and charge transport in the (Sr,La)NbO3.5-x system," *Physical Review B*, vol. 65, p. 155115, Apr. 2002.

[111] T. Pajkossy, "Impedance spectroscopy at interfaces of metals and aqueous solutions — Surface roughness, CPE and related issues," *Solid State Ionics*, vol. 176, pp. 1997–2003, Aug. 2005.

[112] P. Zoltowski, "On the electrical capacitance of interfaces exhibiting constant phase element behaviour," *Journal of Electroanalytical Chemistry*, vol. 443, pp. 149–154, Feb. 1998.

[113] A. Maritan, "On skewed arc plots of impedance of electrodes with an irreversible electrode process," *Electrochimica Acta*, vol. 35, no. I, pp. 141–145, 1990.

[114] T. Pajkossy, "Impedance of rough capacitive electrodes," *Journal of Electroanalytical Chemistry*, vol. 364, pp. 111–125, 1994.

[115] B. Hirschorn, M. E. Orazem, B. Tribollet, V. Vivier, I. Frateur, and M. Musiani, "Determination of effective capacitance and film thickness from constant-phase-element parameters," *Electrochimica Acta*, vol. 55, pp. 6218–6227, Aug. 2010.

[116] Z. Luka, "Evaluation of model and dispersion parameters and their effects on the formation of constant-phase elements in equivalent circuits," *Journal of Electroanalytical Chemistry*, vol. 464, pp. 68–75, 1999.

[117] D. Levie and G. Unruersity, "On the impedance of electrodes with rough interfaces," *J. Electroanal. Chem.*, vol. 261, pp. 1–9, 1989.

[118] Rosa, "The self and mutual-inductance of linear conductors," *Bulletin of the Bureau of Standards*, vol. 4, no. 301-344, 1908.

[119] D. Y. Kondakov, J. R. Sandifer, C. W. Tang, and R. H. Young, "Nonradiative recombination centers and electrical aging of organic light-emitting diodes: Direct connection between accumulation of trapped charge and luminance loss," *Journal of Applied Physics*, vol. 93, no. 2, p. 1108, 2003.

[120] J. Crank, "Mathematical Models in Heat Flow and Diffusion," vol. 1, no. March, pp. 27–37, 1970.

[121] J. Crank, *The mathematics of diffusion.* Oxford: Clarendon Pr., 2. ed., re ed., 1994.

[122] J. Scherbel, P. H. Nguyen, G. Paasch, W. Bruetting, and M. Schwoerer, "Temperature dependent broadband impedance spectroscopy on poly-(p-phenylene-vinylene) light-emitting diodes," *Journal of Applied Physics*, vol. 83, no. 10, p. 5045, 1998.

[123] J. A. Reedijk, H. C. F. Martens, S. M. C. van Bohemen, O. Hilt, H. B. Brom, and M. A. J. Michels, "Charge transport in doped polythiophene," *Synthetic Metals*, vol. 101, no. 1–3, pp. 475–476, 1999.

[124] a. Gusso, "Modeling of organic light-emitting diodes with graded concentration in the emissive multilayer," *Journal of Applied Physics*, vol. 95, no. 4, p. 2056, 2004.

[125] BOTEST SYSTEMS GMBH, "BOTEST LIV." http://www.botest.de/images/gallery/liv_02.jpg [Online; accessed 31-August-2013].

[126] R. Tone, *Impedance Spectroscopy as a Tool for the Detection of Mixed Layers in Organic Devices.* Master thesis, University Heidelberg, 2013.

[127] M. Kroeger, S. Hamwi, J. Meyer, T. Riedl, W. Kowalsky, and A. Kahn, "Role of the deep-lying electronic states of MoO[sub 3] in the enhancement of hole-injection in organic thin films," *Applied Physics Letters*, vol. 95, no. 12, p. 123301, 2009.

[128] F. Lindla, M. Boesing, P. van Gemmern, D. Bertram, D. Keiper, M. Heuken, H. Kalisch, and R. H. Jansen, "Employing exciton transfer molecules to increase the lifetime of phosphorescent red organic light emitting diodes," *Applied Physics Letters*, vol. 98, no. 17, p. 173304, 2011.

[129] J. Meyer, M. Kroeger, S. Hamwi, F. Gnam, T. Riedl, W. Kowalsky, and A. Kahn, "Charge generation layers comprising transition metal-oxide/organic interfaces: Electronic structure and charge generation mechanism," *Applied Physics Letters*, vol. 96, no. 19, p. 193302, 2010.

[130] S.-J. Su, E. Gonmori, H. Sasabe, and J. Kido, "Highly Efficient Organic Blue- and White-Light-Emitting Devices Having a Carrier- and Exciton-Confining Structure for Reduced Efficiency Roll-Off," *Advanced Materials*, pp. NA–NA, Oct. 2008.

[131] D.-H. Lee, Y.-P. Liu, K.-H. Lee, H. Chae, and S. M. Cho, "Effect of hole transporting materials in phosphorescent white polymer light-emitting diodes," *Organic Electronics*, vol. 11, pp. 427–433, Mar. 2010.

[132] S. Noh, C. K. Suman, Y. Hong, and C. Lee, "Carrier conduction mechanism for phosphorescent material doped organic semiconductor," *Journal of Applied Physics*, vol. 105, no. 3, p. 033709, 2009.

[133] Y. Shirota and H. Kageyama, "Charge carrier transporting molecular materials and their applications in devices.," *Chemical reviews*, vol. 107, pp. 953–1010, Apr. 2007.

[134] T. Hofbeck and H. Yersin, "The triplet state of fac-Ir(ppy)3.," *Inorganic chemistry*, vol. 49, pp. 9290–9, Oct. 2010.

[135] S. Reineke, G. Schwartz, K. Walzer, M. Falke, and K. Leo, "Highly phosphorescent organic mixed films: The effect of aggregation on triplet-triplet annihilation," *Applied Physics Letters*, vol. 94, no. 16, p. 163305, 2009.

[136] B. Martini, *Studien zur Realisierung einer nanoskopischen organischen Leuchtdiode auf der Spitze einer Rasterkraftsonde.* Diploma thesis, University Heidelberg, 2012.

[137] B.-S. Kim, D.-E. Kim, Y.-K. Jang, N.-S. Lee, O.-K. Kwon, and Y.-S. Kwon, "UV-Ozone Surface Treatment of Indium-Tin-Oxide in Organic Light Emitting Diodes," *Journal of the Korean Physical Society*, vol. 50, p. 1858, June 2007.

[138] J. Meyer, S. Hamwi, T. Buelow, H.-H. Johannes, T. Riedl, and W. Kowalsky, "Highly efficient simplified organic light emitting diodes," *Applied Physics Letters*, vol. 91, no. 11, p. 113506, 2007.

[139] J. Lee, J.-I. Lee, J. Y. Lee, and H. Y. Chu, "Enhanced efficiency and reduced roll-off in blue and white phosphorescent organic light-emitting diodes with a mixed host structure," *Applied Physics Letters*, vol. 94, no. 19, p. 193305, 2009.

[140] A. F. Rausch, M. E. Thompson, and H. Yersin, "Matrix effects on the triplet state of the OLED emitter Ir(4,6-dFppy)2(pic) (FIrpic): investigations by high-resolution optical spectroscopy.," *Inorganic chemistry*, vol. 48, pp. 1928–37, Mar. 2009.

[141] B. Krummacher, M. K. Mathai, V.-E. Choong, S. a. Choulis, F. So, and A. Winnacker, "Influence of charge balance and microcavity effects on resultant efficiency of organic-light emitting devices," *Organic Electronics*, vol. 7, pp. 313–318, Oct. 2006.

[142] A. Fukase, K. L. T. Dao, and J. Kido, "High-efficiency organic electroluminescent devices using iridium complex emitter and arylamine-containing polymer buffer layer," *Polymers for Advanced Technologies*, vol. 13, pp. 601–604, Aug. 2002.

[143] S. H. Kim, J. Jang, and J. Y. Lee, "Lifetime improvement of green phosphorescent organic light-emitting diodes by charge confining device structure," *Applied Physics Letters*, vol. 90, no. 20, p. 203511, 2007.

[144] E. A.-f. I. Saad, "Dielectric properties of molybdenum oxide thin films," *Journal of Optoelectronics and Advances Materials*, vol. 7, no. 5, pp. 2743–2752, 2005.

[145] V. K. Sabhapathi, O. M. Hussain, S. Uthanna, B. Naidu, P. Reddy, C. Julien, and M. Balkanski, "A.c. conductivity studies on A1/MoO3/A1 sandwich structures," *Materials Science and Engineering*, vol. 32, pp. 93–97, 1995.

Erklärung

Ich versichere, dass ich diese Arbeit selbständig verfasst und keine anderen als die angegeben Quellen und Hilfsmittel benutzt habe.

Heidelberg, den 30.09.2013   ....

                                                     (Paul Faßl)